

**MEASUREMENTS OF THE DEUTERON, PROTON AND HE-3
MAGNETIC FORM FACTORS AT LARGE MOMENTUM TRANSFERS**

Jefferson Lab PAC33 Proposal

December 2007

R. Alarcon, B. D. Anderson, K. A. Aniol, E. J. Beise, L. Bimbot, J. R. Calarco,
A. Camsonne, J.-P. Chen, M. B. Epstein, S. Gilad, J. Gomez, F. Gross,
J.-O. Hansen, D. Higinbotham, J. Huang, C. W. de Jager, X. Jiang, A. T. Katramatou,
E. Khrosinkova, R. De Leo, L. Lagamba, J. LeRose, N. Liyanage, D. M. Manley,
S. Marrone, Z.-E. Meziani, M. Mihovilovič, B. Moffit, P. Monaghan,
N. Muangma, M. N. Olson, G. G. Petratos, M. Potokar, A. Puckett, O. Rondon,
A. Saha, M. H. Shabestari, S. Širca, N. Sparveris, R. Subedi, V. Sulkosky,
J. W. Watson, X. Zhan, W.-M. Zhang, X. Zheng

Arizona State University, Tempe, AZ 85287

California State University, Los Angeles, CA 90032

INFN/Bari and University of Bari, 70126 Bari, Italy

Jefferson Lab, Newport News, VA 23606

Kent State University, Kent, OH 44242

Los Alamos National Laboratory, Los Alamos, NM 87544

Jožef Stefan Institute and Physics Dept., University of Ljubljana, Slovenia

University of Maryland, College Park, MD 20742

Massachusetts Institute of Technology, Cambridge, MA 02139

University of New Hampshire, Durham, NH 03824

Institut de Physique Nucléaire, F-91406 Orsay, France

St. Norbert College, De Pere, WI 54115

Temple University, Philadelphia, PA 19122

University of Virginia, Charlottesville, VA 22904

Spokespersons: A. Camsonne, J. Gomez, A. Katramatou, N. Sparveris and G. Petratos

Contact person: G. Petratos (gpetrato@kent.edu)

Abstract

We propose an experiment on a precision measurement of the deuteron $B(Q^2)$ magnetic form factor around its diffraction minimum and at large momentum transfers, possibly up to $Q^2 = 6 \text{ (GeV}/c)^2$, limited only by cross section sensitivity. The experiment can be performed in the JLab Hall A Facility using i) two backward ($\sim 170^\circ$) custom-made spectrometers to detect back-scattered electrons and ii) two 3.5° spectrometers using a dual-septum dipole magnet and the two High Resolution Spectrometers to detect forward-recoiling deuterons in coincidence. The experiment will also be able to measure a) elastic electron-proton scattering in the Q^2 range from 0.4 to 4.3 $(\text{GeV}/c)^2$ and provide precision data on the proton G_M^p magnetic form factor, free of Rosenbluth separation experimental deficiencies, and b) elastic electron- ^3He scattering to measure precisely the F_M magnetic form factor of the nucleus around its 1st first diffraction minimum and at $Q^2 = 75 \text{ fm}^{-2}$. The $B(Q^2)$ results are expected to play a crucial role in understanding the internal structure and dynamics of the deuteron. The new $B(Q^2)$ data will offer unique grounds for testing non-relativistic and relativistic models of the nucleon-nucleon interaction and meson-exchange currents, as well as ideas based on quark degrees of freedom and perturbative QCD. The precision of the $B(Q^2)$ data will constrain the theoretical uncertainties and hopefully result in a consistent canonical hadronic model describing the electromagnetic structure of the simplest nucleus in nature. The new G_M^p data will be highly complementary to recent precise JLab polarization data on the proton G_E^p electric form factor and will provide valuable input in understanding the extraction of the proton elastic form factors from polarized and unpolarized measurements. The ^3He data are expected to provide severe constraints in analytic Faddeev or Monte Carlo method three-body problem approaches and play a major role in the establishment of a standard meson-nucleon model describing the few-body nuclear systems. The experiment will use a cryogenic deuterium/hydrogen/ ^3He system with 5, 10 and 15 cm long cells. The experiment requires beam energies in the range of 0.5 to 2.7 GeV, beam currents of up to 120 μA , 38 days of deuterium, hydrogen and ^3He data taking at 100% efficiency, and 3 days of check-out time at low beam current.

Contents

1	Precision Measurement of the Deuteron Magnetic Form factor	4
1.1	Theory Overview	4
1.2	Overview of Large Q^2 Measurements	11
1.3	Experiment versus Theory	13
1.4	Motivation for New $B(Q^2)$ Measurements	20
1.5	The Experimental Setup	28
1.5.1	The Dual 3.5° Recoil Spectrometers	33
1.5.2	The Dual Backward Electron Spectrometers	36
1.6	The Deuteron Proposed Measurements	39
2	Precision Measurement of the Proton Magnetic Form Factor	44
2.1	Short Review of the Proton Form Factors	44
2.2	The Proton Proposed Measurements	50
3	Precision Measurement of the ^3He Magnetic Form Factor	52
3.1	Short Review of the ^3He Form Factors	52
3.2	The ^3He Proposed Measurements	57
4	Summary–Request	60
5	Tables	62
6	APPENDIX: The Monte Carlo Simulation	68
6.1	The Coincidence Elastic Cross Section	68
6.2	Overview of the Simulation Method	69
6.3	The Effective Double-Arm Solid Angle	76
7	Bibliography	82

1 Precision Measurement of the Deuteron Magnetic Form factor

1.1 Theory Overview

Electron scattering from the deuteron has long been a crucial tool in understanding the internal structure and dynamics of the nuclear two-body system [1, 2, 3, 4]. In particular, the deuteron electromagnetic form factors, measured in elastic scattering, offer unique opportunities to test models of the short-range nucleon-nucleon interaction and meson-exchange currents as well as the possible influence of explicit quark degrees of freedom [5].

The cross section for elastic electron-deuteron scattering is described, in the one-photon exchange approximation, by the Rosenbluth formula:

$$\frac{d\sigma}{d\Omega} = \frac{\alpha^2 E'}{4E^3 \sin^4\left(\frac{\Theta}{2}\right)} \left[A(Q^2) \cos^2\left(\frac{\Theta}{2}\right) + B(Q^2) \sin^2\left(\frac{\Theta}{2}\right) \right], \quad (1)$$

where E and E' are the incident and scattered electron energies, Θ is the electron scattering angle, $Q^2 = 4EE' \sin^2(\Theta/2)$ is the four-momentum transfer squared and α is the fine-structure constant. The elastic structure functions $A(Q^2)$ and $B(Q^2)$ are given in terms of the charge, quadrupole and magnetic form factors of the deuteron $G_C(Q^2)$, $G_Q(Q^2)$ and $G_M(Q^2)$:

$$A(Q^2) = G_C^2(Q^2) + \frac{8}{9}\tau^2 G_Q^2(Q^2) + \frac{2}{3}\tau G_M^2(Q^2), \quad (2)$$

$$B(Q^2) = \frac{4}{3}\tau(1 + \tau)G_M^2(Q^2), \quad (3)$$

where $\tau = Q^2/4M_d^2$, with M_d being the deuteron mass. Since $A(Q^2)$ is dominated by the two electric form factors and since $B(Q^2)$ is directly proportional to the magnetic one, it is customary to call $A(Q^2)$ and $B(Q^2)$ the electric and magnetic deuteron form factors, respectively. This convention will be followed throughout the text.

Separation of the two $A(Q^2)$ and $B(Q^2)$ elastic structure functions is accomplished by cross section measurements at different scattering angles. Forward angle scattering [6] yields $A(Q^2)$, while backward angle scattering [7] allows for the determination of $B(Q^2)$. Separation of all three $G_C(Q^2)$, $G_Q(Q^2)$ and $G_M(Q^2)$ form factors is achieved by measuring a polarization observable in a single- or double-scattering experiment [8, 9]. Single-scattering experiments

have used unpolarized electron beams and tensor-polarized deuteron targets [10]. Double-scattering experiments have used unpolarized electron beams and recoil deuteron tensor polarimeters [11].

Cross section asymmetry measurements with an electron beam and a tensor-polarized target or a deuteron tensor polarimeter, result in the extraction of the deuteron tensor polarization observable $t_{20}(Q^2)$, which is given in terms of the deuteron form factors as:

$$t_{20}(Q^2) = -\frac{1}{\sqrt{2}S(Q^2)} \left[\frac{8}{3}\tau G_C(Q^2)G_Q(Q^2) + \frac{8}{9}\tau^2 G_Q^2(Q^2) + \frac{1}{3}\tau f(\Theta)G_M^2(Q^2) \right], \quad (4)$$

where $S(Q^2) = A(Q^2) + B(Q^2)\tan^2(\Theta/2)$ and $f(\Theta) = 1 + 2(1 + \tau)\tan^2(\Theta/2)$. It is customary to neglect the small contribution of $G_M(Q^2)$ in $t_{20}(Q^2)$ and use the alternate quantity $\tilde{t}_{20}(Q^2)$, defined as:

$$\tilde{t}_{20}(Q^2) = \sqrt{2}\frac{y(2+y)}{1+2y^2}, \quad y = \frac{2\tau G_Q(Q^2)}{3G_C(Q^2)}. \quad (5)$$

The advantage of this quantity is that, in both the non-relativistic and relativistic impulse approximation, it is independent of the nucleon electromagnetic form factors, as they cancel in the ratio $G_Q(Q^2)/G_C(Q^2)$.

In the non-relativistic impulse approximation (IA), the electron interacts, through the exchange of a virtual photon, with one of the two moving nucleons in the deuteron (see Figure 1a), and the two-body bound state is solved using the Schrödinger equation with a realistic nucleon-nucleon (N-N) potential. The deuteron form factors are then described in terms of the deuteron wave function and the electromagnetic form factors of the nucleons [12]:

$$G_C = (G_E^p + G_E^n)C_E, \quad (6)$$

$$G_Q = (G_E^p + G_E^n)C_Q, \quad (7)$$

$$G_M = \frac{M_d}{M} \left[(G_M^p + G_M^n)C_S + \frac{1}{2}(G_E^p + G_E^n)C_L \right], \quad (8)$$

where G_E^p and G_M^p are the electric and magnetic form factors of the proton, G_E^n and G_M^n are the electric and magnetic form factors of the neutron, and M is the nucleon mass. The factors C_E , C_Q , C_S and C_L give the distribution of the proton and neutron point currents inside the deuteron as determined by the deuteron wave function. They are integrals of quadratic combinations of the S - and D -state wave functions $u(r)$ and $w(r)$ of the deuteron, with r being the internucleon separation, expressed as:

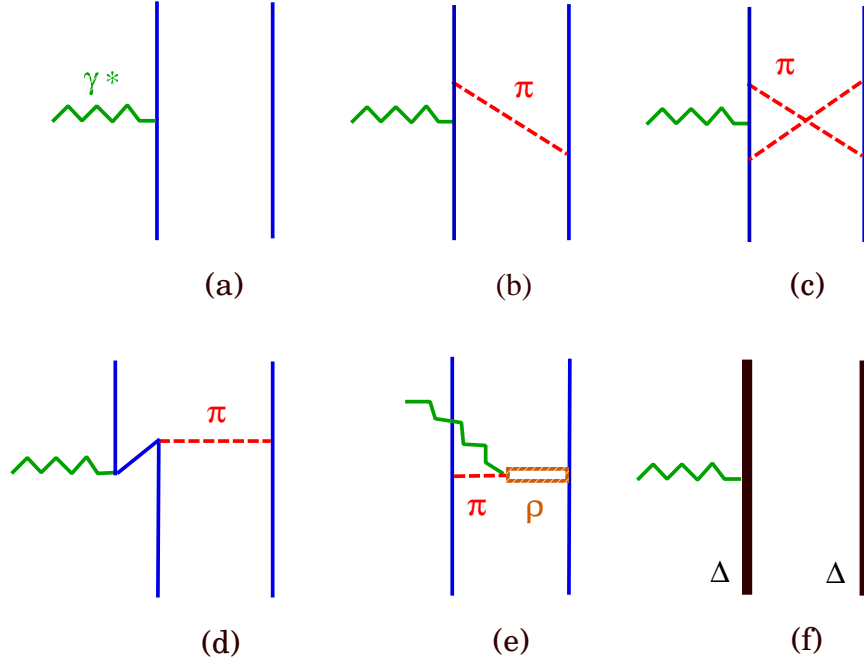


Figure 1: Non-relativistic diagrammatic representation of elastic electron-deuteron scattering. (a): impulse approximation; (b-e): selected meson-exchange current diagrams (retardation correction, two-pion exchange current, pair current and $\rho\pi\gamma$ interaction current) ; (f): isobar configuration.

$$C_E = \int_0^\infty [u^2(r) + w^2(r)] j_0(k) dr, \quad (9)$$

$$C_Q = \frac{3}{\sqrt{2}\tau} \int_0^\infty w(r) \left[u(r) - \frac{w(r)}{2\sqrt{2}} \right] j_2(k) dr, \quad (10)$$

$$C_S = \int_0^\infty \left[u^2(r) - \frac{w^2(r)}{2} \right] j_0(k) + \frac{w(r)}{2} [\sqrt{2}u(r) + w(r)] j_2(k) dr, \quad (11)$$

$$C_L = \frac{3}{2} \int_0^\infty w^2(r) [j_0(k) + j_2(k)] dr, \quad (12)$$

where $j_0(k)$ and $j_2(k)$ are spherical Bessel functions, with $k = Qr/2$.

Theoretical calculations based on the IA approach using various nucleon-nucleon potentials and parametrizations of the nucleon form factors underestimate the $A(Q^2)$ data and fail to reproduce the position of the first diffraction minimum and the height of the secondary maximum of the charge and magnetic form factor data (for extended theory and experiment reviews, and compilations of experimental data see References [1], [2], [3], [4] and [13]). It has long been known that the deuteron form factors are very sensitive to the presence of

meson-exchange currents (MEC) and/or relativistic effects in the deuteron. The inclusion of “model independent” (Figure 1b, 1c, 1d) and “model dependent” (Figure 1e) MEC to the IA brings the theory into better agreement with the data but still fails to describe at the same time all available deuteron form factor data for moderate and large momentum transfer measurements [2, 3]. It should be noted that some calculations of the deuteron form factors show also sensitivity to possible presence of isobar configurations (Figure 1f) in the deuteron wave function [14, 15], but the magnitude of these configurations is essentially unknown. In general, inclusion of reasonable isobar configurations in the IA does not bring the non-relativistic calculations in agreement with all available deuteron form factor data.

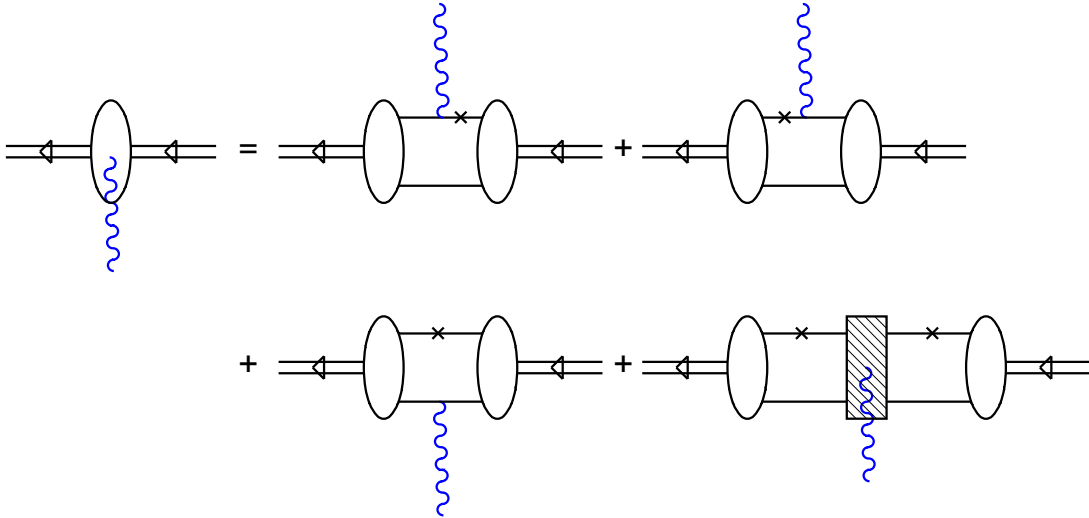


Figure 2: Feynman diagrams representing elastic electron-deuteron scattering in the Complete Impulse Approximation relativistic approach of Gross and collaborators [20]. The crosses on the nucleon lines denote on-shell particles. The shaded box depicts the $\rho\pi\gamma$ interaction current.

The failure of the non-relativistic calculations with increasing momentum transfers dictates the need for relativistic calculations. There are two relativistic approaches: Hamiltonian Dynamics [16, 17] and Propagator Dynamics [18]. In the first approach, the basic dynamics contains a finite number of particles and has a corresponding Hilbert space when quantized. The quantization is performed along constant time surfaces (instant-form dynamics), along spacelike surfaces with constant interval (point-form dynamics), or along the light

cone (light-front dynamics). The advantage of the hamiltonian dynamics framework is that it can lead to equations of motion of the same form as the two-body Schrödinger equation, where it is possible to use non-relativistic nucleon-nucleon potentials without modification. The disadvantage of this formalism is, in general, the loss of locality and manifest covariance. Also, no consensus has been reached concerning consistent techniques for the construction of electromagnetic currents in this framework [2, 3].

The second approach is based on a field theory description of two interacting nucleons using three-dimensional reductions of the Bethe-Salpeter (BS) equation [19], which is a four-dimensional integral equation with a complicated analytical structure. The three-dimensional reduction to so called quasipotential equations is accomplished by replacing the free propagator in the BS equation with a new one, chosen to include a constraint in the form of a delta function involving either the relative energy [20, 21] or time [22] of the interacting nucleons. The advantage of the propagator dynamics is the retainment of locality and manifest covariance. The disadvantage of this approach is the inclusion of negative energy states in the particle propagators, which tends to make the calculations technically more difficult and their physical interpretation harder. A diagrammatic representation of one of the propagator dynamics approaches by Gross and collaborators [20] is shown in Figure 2. The Figure includes also the $\rho\pi\gamma$ interaction current (shaded box). Recent dramatic advances in the refinement of the propagation dynamics approach have brought the theory in reasonable agreement with the experimental data (see below).

It is widely recognized that at distances much less than the nucleon size, the underlying quark-gluon dynamics of the deuteron cannot be ignored. This has led to the formulation of so called hybrid quark models [23, 24, 25], which try to simultaneously incorporate the quark- and gluon-exchange mechanism at short distances and the meson-exchange mechanism at long and intermediate distances. A commonly used approach divides the deuteron in two regions: an exterior one described by baryon configurations and an interior one described by a quark cluster. When the internucleon separation becomes smaller than ~ 1 fm, the deuteron is treated as a six-quark configuration with a certain probability. Hybrid models are still in a phenomenological stage but the hope is that they could provide a consistent basis of bridging the meson-nucleon and quark-gluon descriptions of the few-body systems.

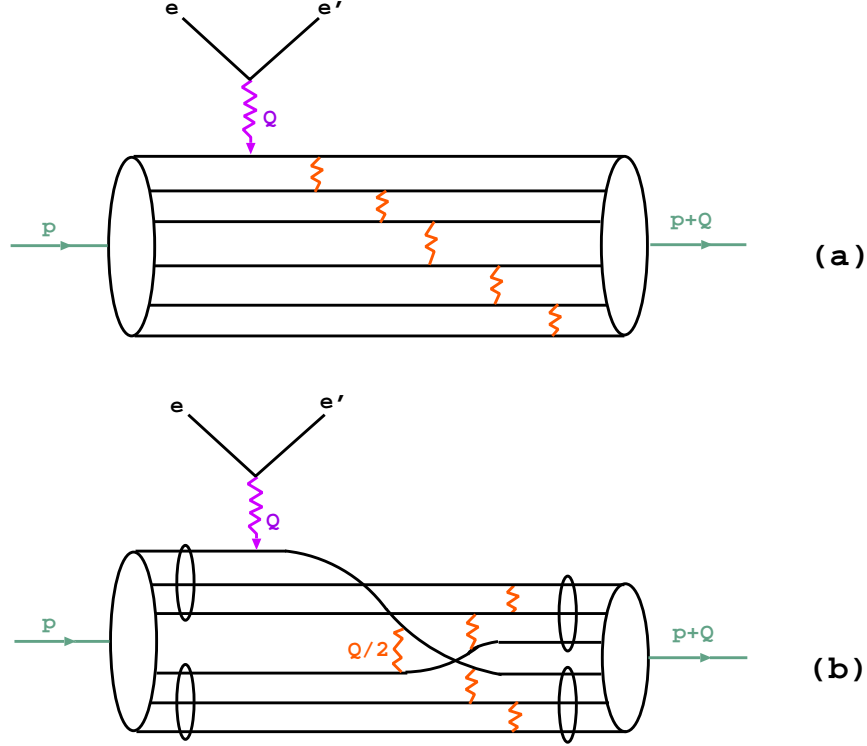


Figure 3: Elastic electron-deuteron scattering in the quark-dimensional scaling model [26, 27] showing the rescattering of the six deuteron constituent quarks (solid lines) via the exchange of hard gluons (wavy lines); (a): democratic six-quark chain model, (b) quark-interchange model.

At sufficiently large momentum transfers the deuteron form factors are expected to be calculable in terms of only quarks and gluons within the framework of Quantum Chromodynamics (QCD). The first attempt at a quark-gluon description of the deuteron form factors was based on quark-dimensional scaling (QDS) [26, 27]: the underlying dynamical mechanism during elastic electron-deuteron scattering is the rescattering of the constituent quarks via the exchange of hard gluons, as shown in Figure 3, which implies that $\sqrt{A(Q^2)} \sim (Q^2)^{-5}$. This prediction was later substantiated in the framework of perturbative QCD (pQCD), where it was shown [28] that to leading-order:

$$\sqrt{A(Q^2)} = \left[\frac{\alpha_s(Q^2)}{Q^2} \right]^5 \sum_{m,n} d_{mn} \left[\ln \frac{Q^2}{\Lambda_{QCD}^2} \right]^{-\gamma_n - \gamma_m}, \quad (13)$$

where $\alpha_s(Q^2)$ and Λ_{QCD} are the QCD strong coupling constant and scale parameter, and $\gamma_{m,n}$ and d_{mn} are QCD anomalous dimensions and constants.

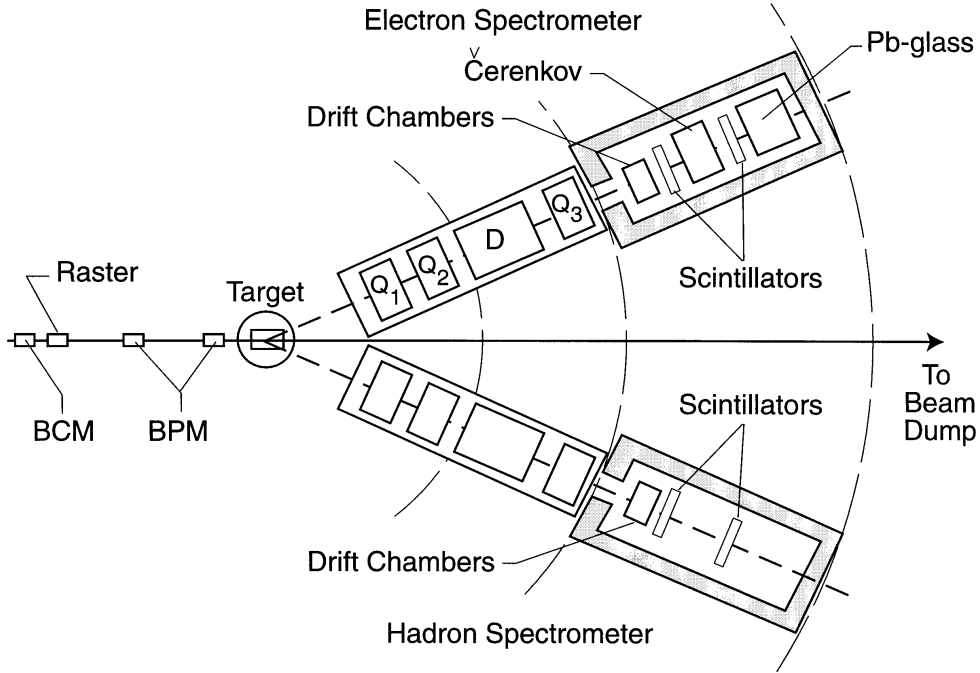


Figure 4: Plan view of the JLab Hall A Facility as used for the recent measurement of the deuteron $A(Q^2)$ at large momentum transfers [6]. Shown are the target scattering chamber, and the two identical high resolution spectrometers with their detectors, each consisting of three quadrupole Q_1 , Q_2 , Q_3 magnets and a dipole D magnet.

A trend consistent with the QDS and pQCD predictions for the deuteron electric form factor has been observed in recent Jefferson Lab (JLab) measurements (see below) [6]. Extension of the above pQCD calculations for the magnetic form factor has resulted in the prediction [29]:

$$\frac{B(Q^2)}{A(Q^2)} \simeq \frac{4\tau(\tau + 1)}{\tau^2 + \tau + 3/4}, \quad (14)$$

for $Q^2 \gg 2M_d\Lambda_{QCD} \sim 0.8 (\text{GeV}/c)^2$, which fails to account for the presence of a diffraction minimum in the magnetic form factor. A refinement [30] of the above prediction, which includes helicity-flip matrix elements assumed to be negligible in the original calculation, preserves the asymptotic behavior of the ratio but at the same time allows for the existence of a diffraction minimum in the magnetic form factor.

1.2 Overview of Large Q^2 Measurements

The unique features of the Continuous Electron Beam Accelerator and Hall A Facilities of JLab offered recently the opportunity to extend the kinematical range of $A(Q^2)$ and to resolve inconsistencies in previous data sets from different laboratories by measuring [6] forward scattering angle elastic electron-deuteron scattering for $0.7 \leq Q^2 \leq 6.0$ (GeV/c)². Backward angle measurements [31] in conjunction with the forward angle measurements enabled also determination of $B(Q^2)$ in the kinematical range $0.7 \leq Q^2 \leq 1.4$ (GeV/c)². Electron beams were scattered off a liquid deuterium target. Scattered electrons were detected in the electron High Resolution Spectrometer (HRS). To suppress backgrounds and separate elastic from inelastic scattering events, recoil deuterons were detected in coincidence with the scattered electrons in the hadron HRS. A schematic of the Hall A Facility as used in this experiment (E91-26) is shown in Figure 4.

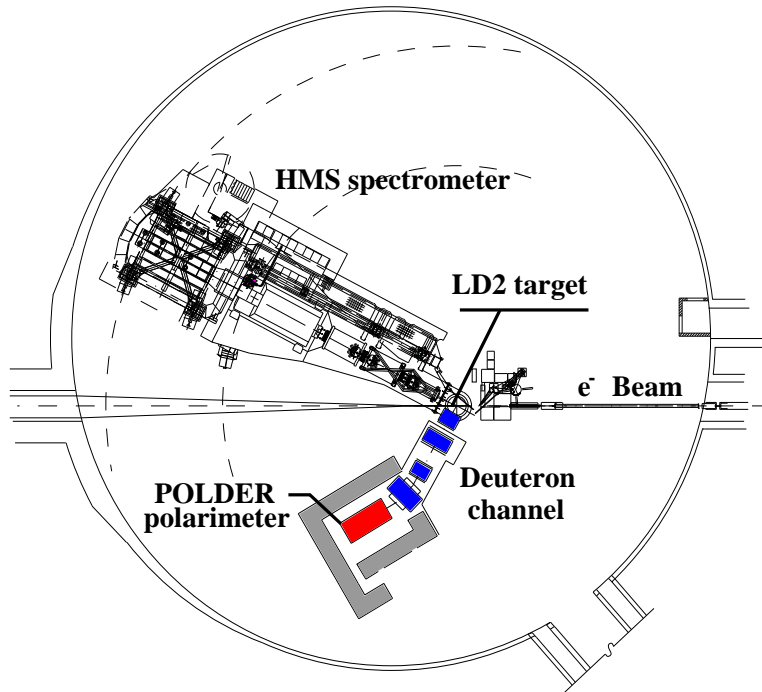


Figure 5: Plan view of the JLab Hall C Facility as used for the recent measurement [11] of the deuteron $t_{20}(Q^2)$. Shown are the electron High Momentum Spectrometer, the deuteron cryotarget, and the recoil deuteron spectrometer with the POLDER polarimeter.

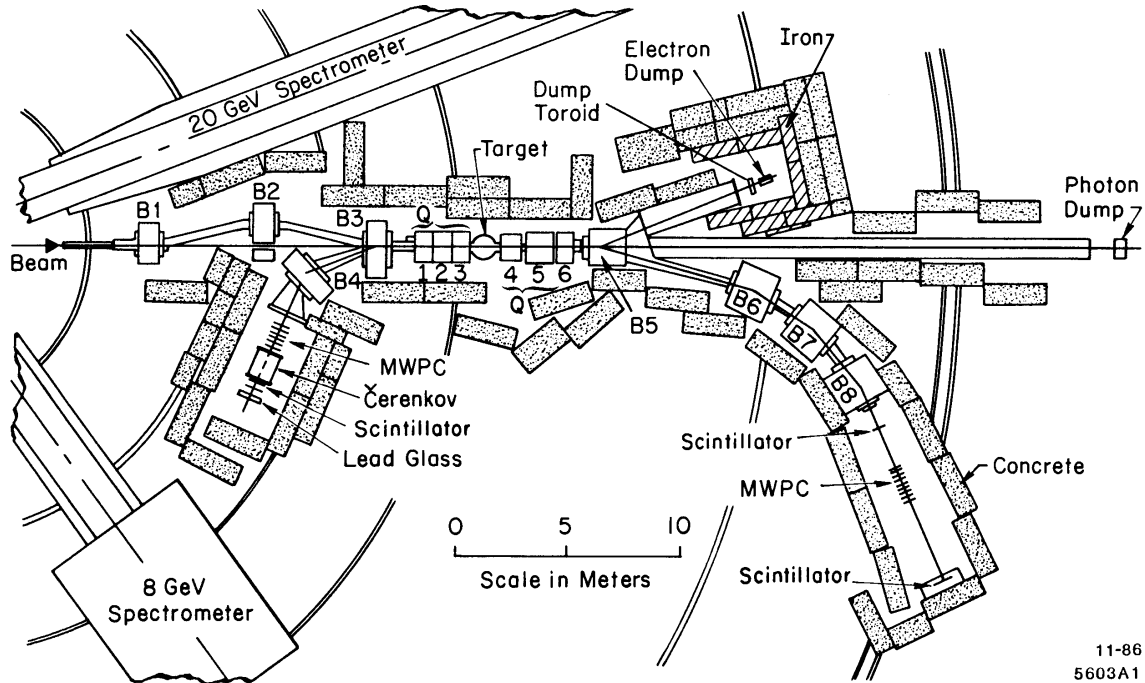


Figure 6: Plan view of the 180° electron and 0° deuteron magnetic spectrometer systems [35, 34] used for the SLAC End Station A measurement [7] of the deuteron $B(Q^2)$ (see text).

Recent advances in deuteron polarimetry and the high luminosity of the JLab Hall C Facility enabled also large Q^2 measurements of $t_{20}(Q^2)$ [11] for $0.7 \leq Q^2 \leq 1.7$ $(\text{GeV}/c)^2$. The experiment (E94-18) also measured precisely $A(Q^2)$ in the same Q^2 region [32]. The experimental setup used the Hall C High Momentum Spectrometer (HMS) to detect scattered electrons and a special deuteron channel to detect and spin-analyze recoil deuterons in coincidence with the electrons (see Figure 5). The deuteron channel consisted of a large solid angle magnetic spectrometer comprised of three quadrupole and one dipole magnets, and the POLDER deuteron tensor polarimeter, calibrated previously at the Saturn Laboratory. The polarimeter was based on the charge exchange reaction $H(\vec{d}, pp)n$ induced by the recoil deuterons in a liquid hydrogen cell. Deuterons incident on the polarimeter were identified with two scintillator trigger planes and two sets of wire chambers. The pairs of protons from the charge exchange reactions were identified with two pairs of scintillator hodoscopes and a wire chamber set.

The highest Q^2 measurements of $B(Q^2)$ were performed [7] in the mid-1980's with a novel double-arm spectrometer system [33, 34, 35] in the SLAC End Station A (Experiment NE4), as shown in Figure 6. Electron beams from the Nuclear Physics Injector were directed on a deuteron target through a chicane of dipole magnets (B1, B2 and B3). Electrons scattered at 180° were transported through a large solid angle spectrometer system consisting of three quadrupole (Q1, Q2, and Q3) and two dipole (B3 and B4) magnets to a set of detectors. The spectrometer system comprised of these magnets had medium resolution. Deuterons recoiling at 0° were transported through a spectrometer system consisting of three quadrupole (Q4, Q5, and Q6) and four dipole (B5, B6, B7 and B8) magnets to another set of detectors. The spectrometer system comprised of these magnets had poor resolution. The primary (unscattered) beams were directed onto a beam dump located inside the End Station. Elastic electron-deuteron coincidence events were identified by the time-of-flight (TOF) method between the electron and recoil spectrometer trigger signals. The kinematical parameters of the coincidence events were defined through the reconstructed momentum and angle of the scattered electrons. The recoil spectrometer was used to tag the coincidence, as the electron spectrometer alone could not identify elastic electrons, due to a combination of its moderate resolution and long target lengths.

1.3 Experiment versus Theory

The experimental data for $A(Q^2)$, $B(Q^2)$ and $t_{20}(Q^2)$ are shown (with the exception of recent $t_{20}(Q^2)$ data from Novosibirsk [10]) in Figures 7–10 together with non-relativistic and relativistic theoretical calculations. The data for $A(Q^2)$ indicate a smooth fall off with no apparent diffractive structure. The data for $B(Q^2)$ indicate the presence of a diffraction minimum in the vicinity of $Q^2 = 1.8 \text{ (GeV}/c)^2$. The large error bars of the SLAC NE4 data are due to limited statistics and to systematics associated with a large photoproduction background mimicking elastic electron-deuteron coincidences. The $t_{20}(Q^2)$ data together with the $A(Q^2)$ and $B(Q^2)$ data show that the charge form factor exhibits a diffractive structure with a minimum at $Q^2 = 0.7 \text{ (GeV}/c)^2$ and that the quadrupole form factor falls off exponentially in the measured Q^2 region [11].

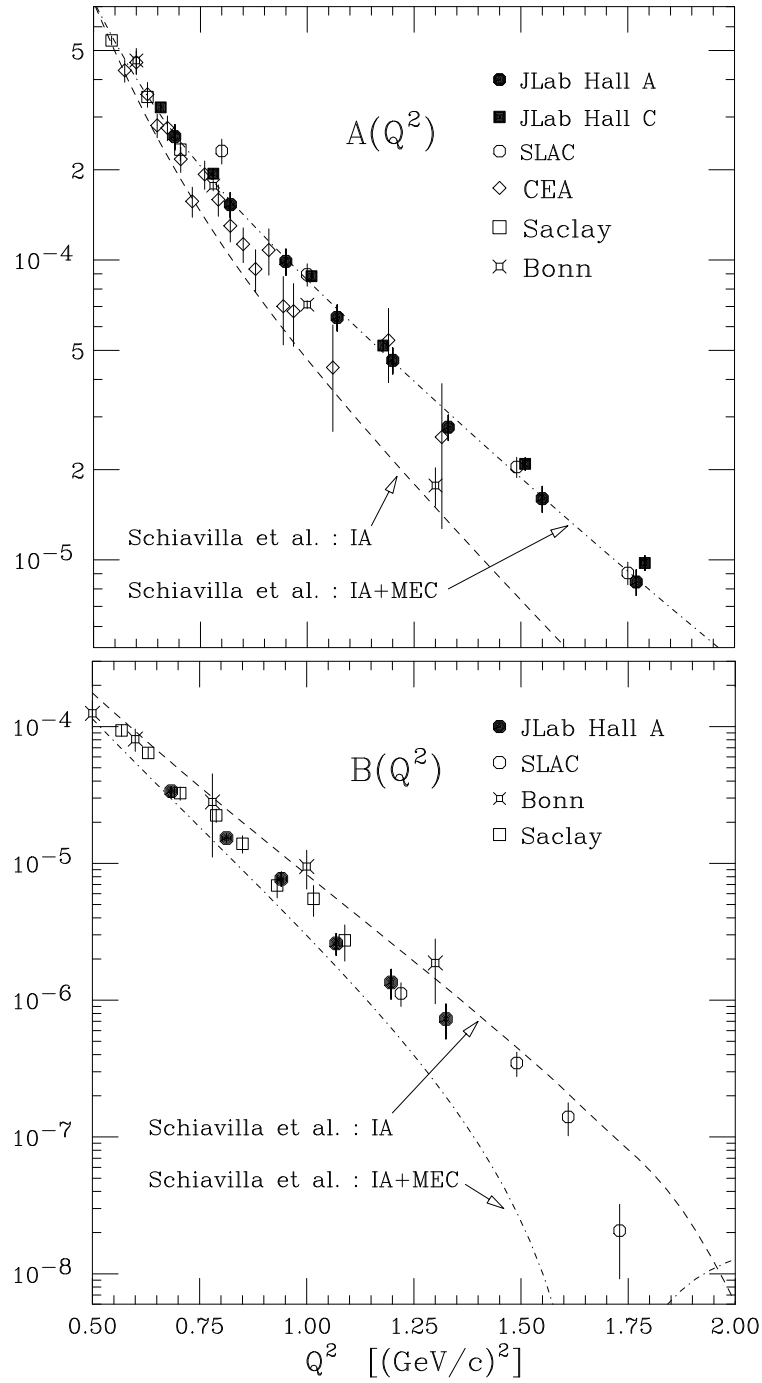


Figure 7: Low Q^2 data [6, 7, 31] on the deuteron $A(Q^2)$ and $B(Q^2)$ electric and magnetic form factors compared with non-relativistic impulse approximation calculations by Schiavilla and collaborators [36] with and without inclusion of meson-exchange currents.

Figure 7 shows $A(Q^2)$ and $B(Q^2)$ data for $Q^2 < 2$ (GeV/c)² compared with a state-of-the-art non-relativistic calculation by Schiavilla and collaborators [36] using the Argonne v_{18} nucleon-nucleon potential. The calculation is based on the impulse approximation approach and includes relativistic corrections and meson-exchange currents. The solid dots in the $B(Q^2)$ plot are the recent data from the JLab E91-26 Hall A experiment [31]. The dashed curve is the impulse approximation calculation. The dot-dashed curve is the full calculation. It is evident from the Figure that this non-relativistic calculation cannot describe both form factors at the same time. This is a pattern present in all non-relativistic calculations.

Figure 8 shows all the available $A(Q^2)$, $B(Q^2)$ and $\tilde{t}_{20}(Q^2)$ experimental data and theoretical calculations based on the propagator dynamics approach [sometimes referred to as the relativistic impulse approximation (RIA)] by three different groups. The solid, dotted and dashed curves represent the RIA calculations of Van Orden, Devine and Gross (VDG) [20], Hummel and Tjon (HT) [21], and Phillips, Wallace and Devine (PWD) [22], respectively. The VDG curve is based on the Gross quasipotential equation [37] with a one-boson-exchange interaction and assumes that the electron interacts with an off-mass-shell nucleon or a nucleon that is on-mass-shell right before or after the interaction (see Figure 2). The HT curve is based on a one-boson-exchange quasipotential approximation of the Bethe-Salpeter equation [38], where the two nucleons are treated symmetrically by putting them equally off their mass-shell with zero relative energy. The PWD curve is also based on a one-boson-exchange interaction but with a single-time equation that constraints the relative time to be zero.

In all three cases the relativistic impulse approximation fails to describe the data. All three theory groups have augmented their models by including the $\rho\pi\gamma$ MEC contribution as shown in Figure 9. The magnitude of this contribution depends on the $\rho\pi\gamma$ coupling constant and vertex form factor choices [39]. The VDG model (solid curve) uses a soft $\rho\pi\gamma$ form factor. The HT model (thin dotted curve) uses a Vector Meson Dominance model hard form factor. The PWD model (dashed curve) uses an intermediate form factor. The inclusion of the $\rho\pi\gamma$ MEC contribution has a small effect on $B(Q^2)$ and $\tilde{t}_{20}(Q^2)$ but increases dramatically $A(Q^2)$. The $A(Q^2)$ data favor use of the softest possible form factor. The thick dotted curve is an alternate calculation by the VDG group with a different nucleon form factor choice in the off-shell modification of the single nucleon current as required to insure current

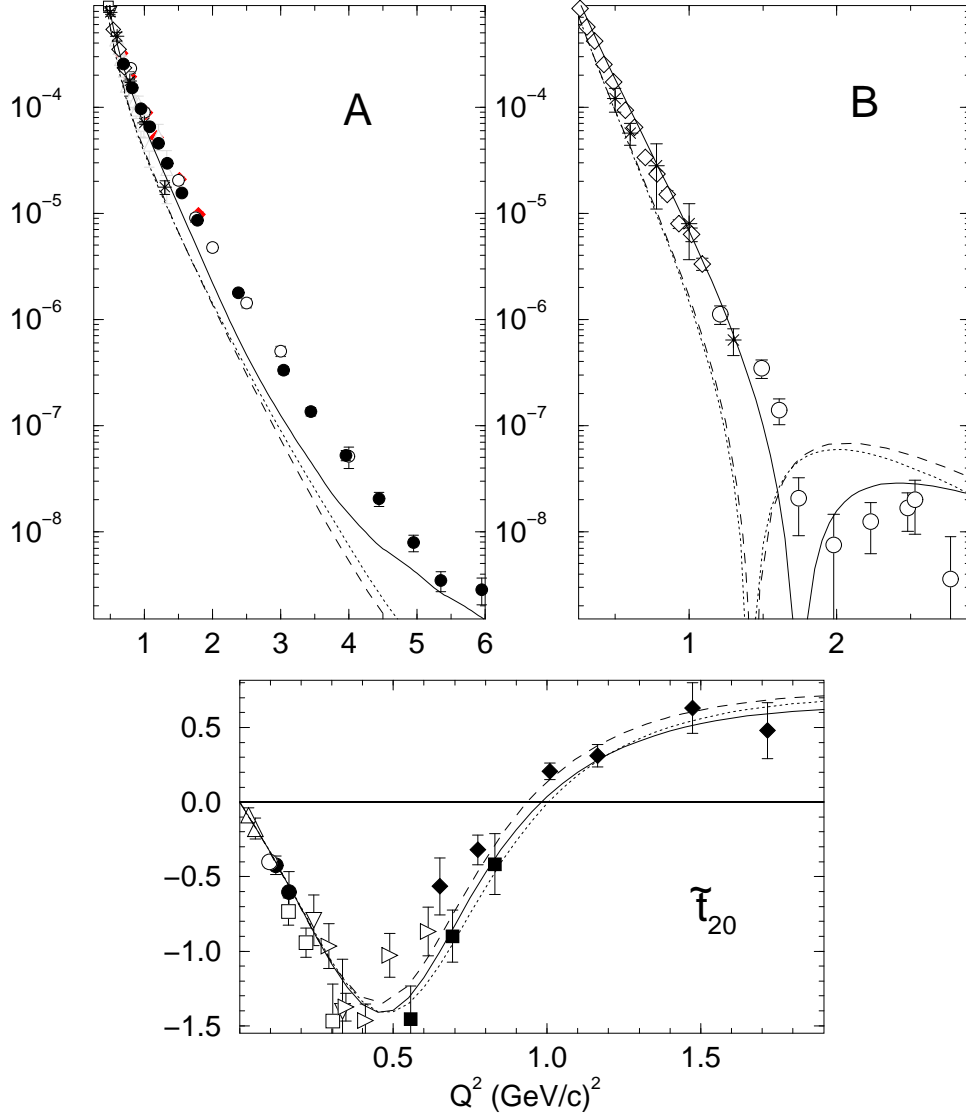


Figure 8: Experimental data [6, 7, 10, 11] on the deuteron $A(Q^2)$, $B(Q^2)$ and $\tilde{t}_{20}(Q^2)$ compared with theoretical calculations based on propagator dynamics (RIA) [20, 21, 22] (see text).

conservation (see next section). This modification affects significantly $B(Q^2)$ and to a lesser degree $\tilde{t}_{20}(Q^2)$. Although the difference in the models is indicative of the size of theoretical uncertainties and ambiguities, it appears that the relativistic impulse approximation can, as in the case of the alternate VDG model, reproduce the deuteron form factor data fairly well.

Figure 10 shows a comparison of selected recent hamiltonian dynamics calculations with the available experimental $A(Q^2)$, $B(Q^2)$ and $\tilde{t}_{20}(Q^2)$ data. The solid curve is a point form

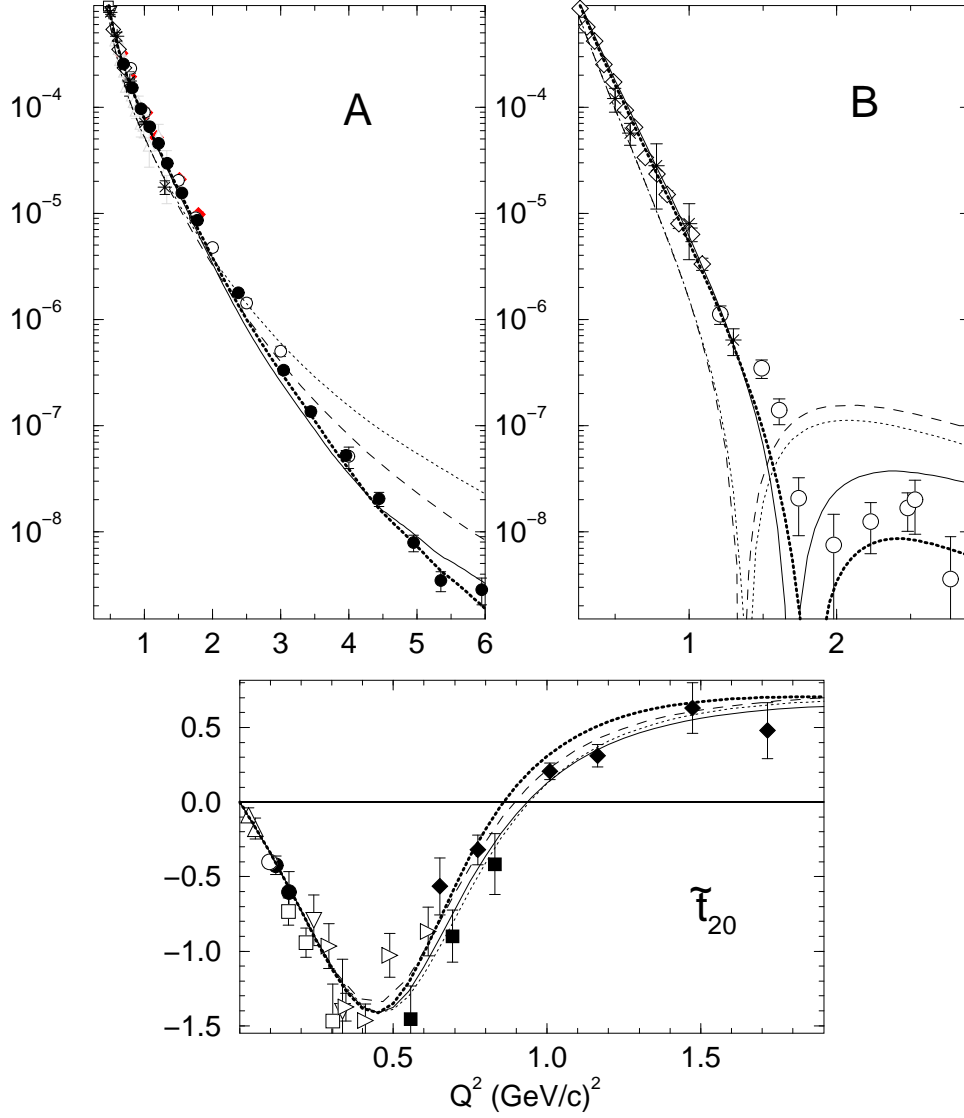


Figure 9: Experimental data [6, 7, 10, 11] on the deuteron $A(Q^2)$, $B(Q^2)$ and $\tilde{t}_{20}(Q^2)$ compared with theoretical calculations based on propagator dynamics (RIA) with inclusion of the $\rho\pi\gamma$ interaction current [20, 21, 22] (see text).

calculation by Allen, Klink and Polyzou [40] using the Argonne v_{18} potential. The dashed curve is a front form calculation by Lev, Pace and Salmè [41] using the Nijmegen potential. The dot-dashed curve is an instant form calculation by Schiavilla and Pandharipande [42] using the Argonne v_{18} potential. These three calculations employ different approaches for the construction of the electromagnetic current. It is evident that none of these admittedly

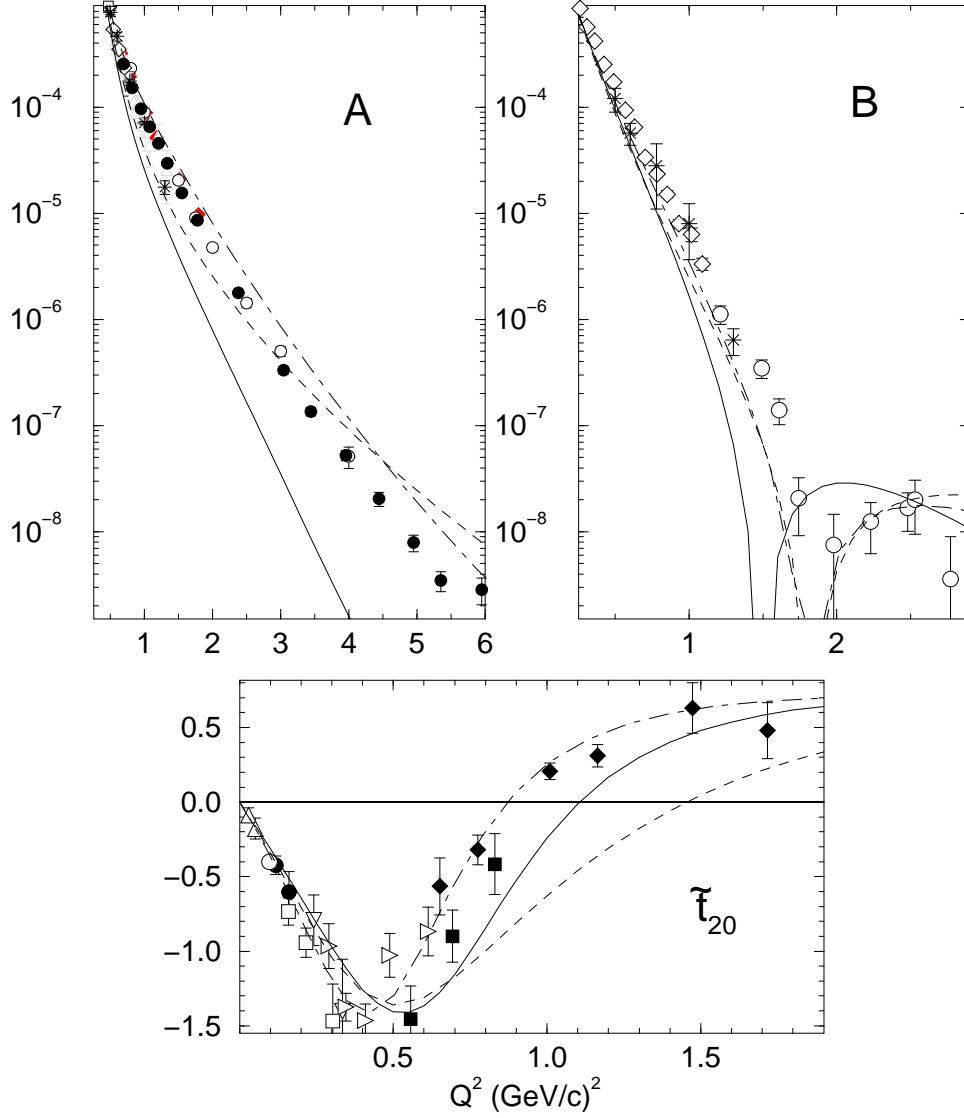


Figure 10: Experimental data [6, 7, 10, 11] on the deuteron $A(Q^2)$, $B(Q^2)$ and $\tilde{t}_{20}(Q^2)$ compared with selected theoretical calculations based on hamiltonian dynamics [40, 41, 42] (see text).

promising approaches is able, at this stage, to describe simultaneously all three $A(Q^2)$, $B(Q^2)$ and $\tilde{t}_{20}(Q^2)$ deuteron observables.

Figure 11 (top) shows values for the “deuteron form factor” $F_d(Q^2) \equiv \sqrt{A(Q^2)}$ from JLab experiment E91-26 [6] and SLAC experiment E101 [43] multiplied by $(Q^2)^5$. It is evident that the data exhibit a behavior consistent with the power law of QDS and pQCD. Figure 11 (bottom) shows values for the “reduced” deuteron form factor $f_d(Q^2) \equiv F_d(Q^2)/F_N^2(Q^2/4)$,

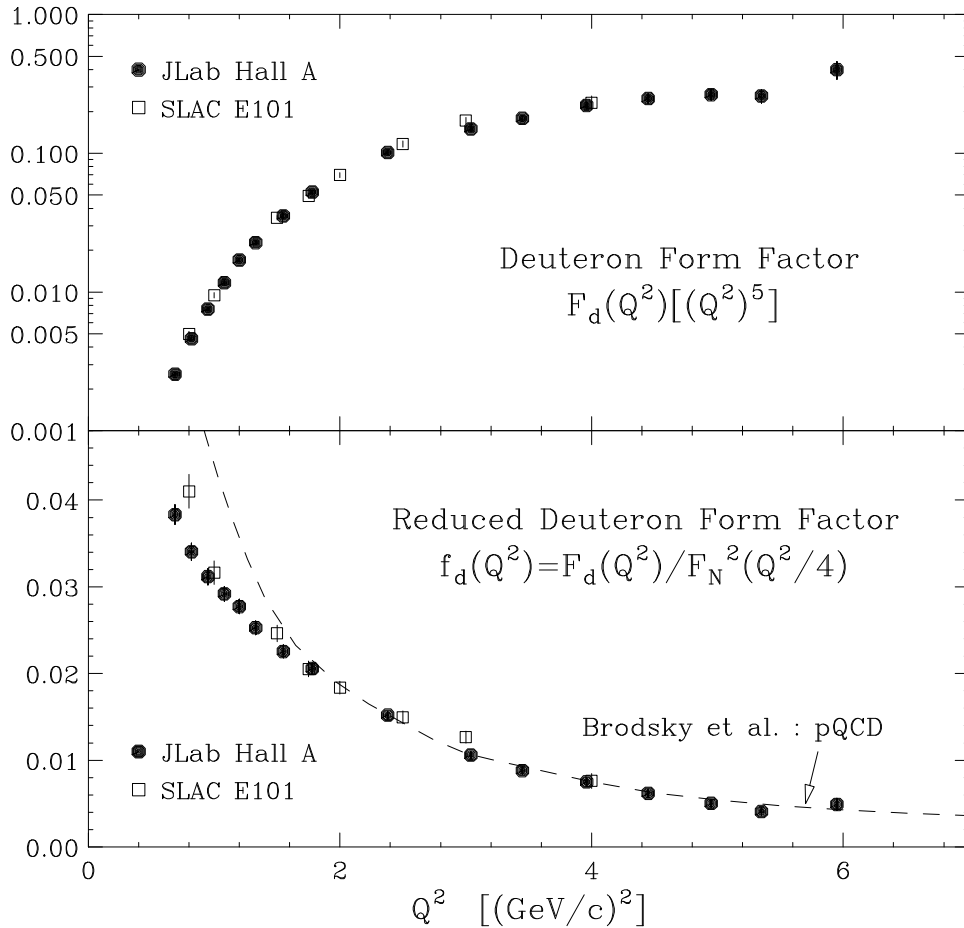


Figure 11: The deuteron form factor $F_d(Q^2)$ times $(Q^2)^5$ (top) and the reduced deuteron form factor $f_d(Q^2)$ (bottom) from JLab [6] and SLAC [43] data. The curve is the asymptotic pQCD prediction [28] for $\Lambda_{QCD} = 100$ MeV, arbitrarily normalized to the data at $Q^2 = 4$ (GeV/c) 2 .

where the two powers of the nucleon form factor $F_N(Q^2) = (1 + Q^2/0.71)^{-2}$ remove in a minimal and approximate way the effects of nucleon compositeness [44]. The $f_d(Q^2)$ data appear to follow, for $Q^2 > 2$ (GeV/c) 2 , the asymptotic Q^2 prediction of pQCD [28]:

$$f_d(Q^2) \sim \frac{\alpha_s(Q^2)}{Q^2} \left[\ln \frac{Q^2}{\Lambda_{QCD}^2} \right]^{-\Gamma}. \quad (15)$$

Here $\Gamma = -(2C_F/5\beta)$, where $C_F = (n_c^2 - 1)/2n_c$, $\beta = 11 - (2/3)n_f$, with $n_c = 3$ and $n_f = 2$ being the numbers of QCD colors and effective flavors. Although several authors have questioned the validity of QDS and pQCD at the momentum transfers of the JLab experiment [45, 46], similar scaling behavior has been reported in deuteron photodisintegration

at moderate photon energies [47]. New large momentum transfer data on many observables, including the deuteron magnetic form factor as well as the three- and four-body form factors will be necessary, before drawing any definitive conclusion for the applicability of pQCD in exclusive processes in the kinematical domain accessible by today’s machines.

1.4 Motivation for New $B(Q^2)$ Measurements

Jefferson Lab is the ideal place to study experimentally the deuteron form factors, “observables of choice” [48] for testing meson-nucleon models describing the electromagnetic structure of the deuteron. The unique capability of its high luminosity and the availability of its superior resolution large acceptance magnetic spectrometers, were instrumental in extending, with an unprecedented precision, the measurements of the deuteron electric form factor $A(Q^2)$ and tensor polarization $t_{20}(Q^2)$ to momentum transfers not accessible by other electron machines. The same features of JLab can be utilized to study the diffraction minimum and the secondary maximum of the deuteron magnetic form factor $B(Q^2)$, and probably more than double the Q^2 range of the existing $B(Q^2)$ data.

The $B(Q^2)$ SLAC data acquired in the “heroic effort” [3] of SLAC experiment NE4 uncovered the diffractive feature of $B(Q^2)$ predicted by the theory (although not beyond *any doubt*, as has been stressed in Ref. [3]) but were unable to determine reliably the location of its diffraction minimum and the strength of its secondary maximum. The NE4 results were limited primarily by large statistical uncertainties, and to a lesser extent by systematic uncertainties from an unexpected large background from two-step photoproduction processes in the target [7]. The possible sources of this background, located predominantly on the radiative tail, were considered to be electron-deuteron coincidences from $\gamma d \rightarrow \gamma d$ (Compton scattering) and/or $\gamma d \rightarrow \pi_0 d$ reactions initiated by bremsstrahlung photons in the target. The second reaction also results in photon production as the π_0 decays in the target into two photons. In both cases the outcome can be a coincidence between a deuteron in the recoil spectrometer and an electron in the electron spectrometer, originating from pair production of a final state photon in the target. The effect of this unforeseen background, which mimicked elastic coincidence events, was inadvertently magnified by the long targets

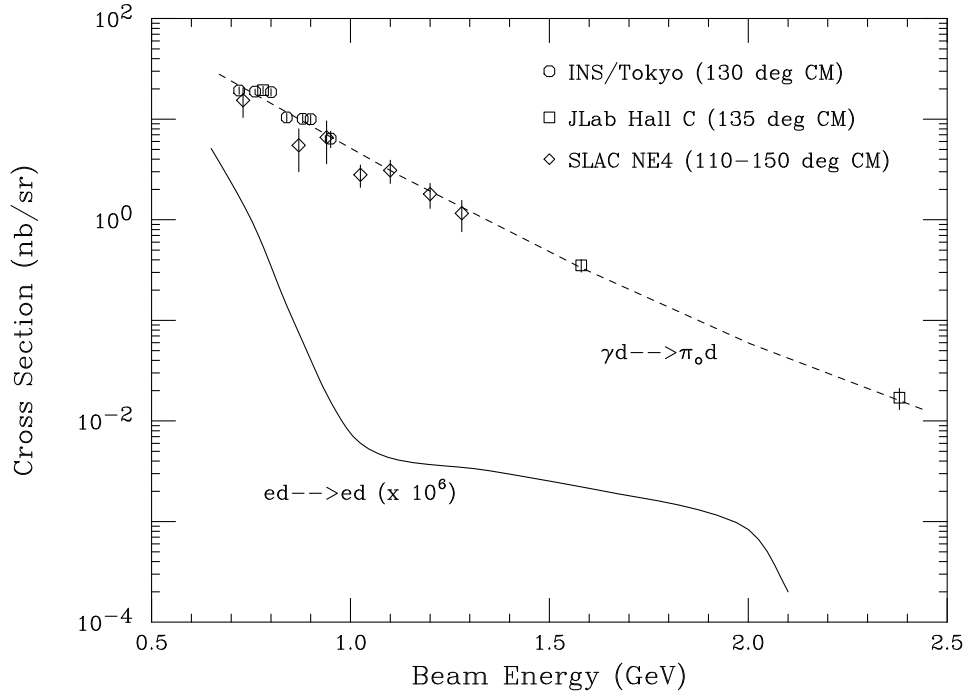


Figure 12: Cross section for the reaction $\gamma d \rightarrow \pi_0 d$, as extracted by experiment SLAC NE4 [7], compared with Tokyo [49] and JLab [50] measurements. The dashed curve is an eye fit to the data. The solid curve is a model for the elastic electron-deuteron cross at the backward NE4 kinematics.

used in NE4, as it grows at least with the square of the target length (all but one kinematical points used 20 and 40 cm long targets), and by the modest (poor) resolution of the electron (recoil) spectrometer. A detailed analysis of these events showed that they were coming overwhelmingly from the $\gamma d \rightarrow \pi_0 d$ reaction. The measured value of the ratio of double-arm electron-deuteron coincidences to single-arm deuterons in the recoil spectrometer was compared to a Monte Carlo ratio calculation of the two types of background. The χ^2/df for the π_0 reaction was 1.9 and for the Compton one 105. Also, the cross section for the π_0 reaction, calculated from single-arm deuterons in the recoil spectrometer under the assumption that Compton scattering is negligible, is in excellent agreement with old data from Tokyo [49] and recent data from JLab Hall C [50], as shown in Figure 12. The effect of this background is shown for all Q^2 points of NE4 in Figure 13, where spectra of coincidence events are plotted versus the double-arm missing momentum δ_{mm} defined as the sum of the relative electron and deuteron momenta (with respect to the central electron and deuteron

spectrometer momenta). It is evident from the Figure that the number of background events on the radiative tail grows about quadratically with target length. JLab can overcome the limitations of the SLAC experiment by using in a high luminosity experiment a short target and a recoil spectrometer with very good resolution as the hadron HRS (see below).

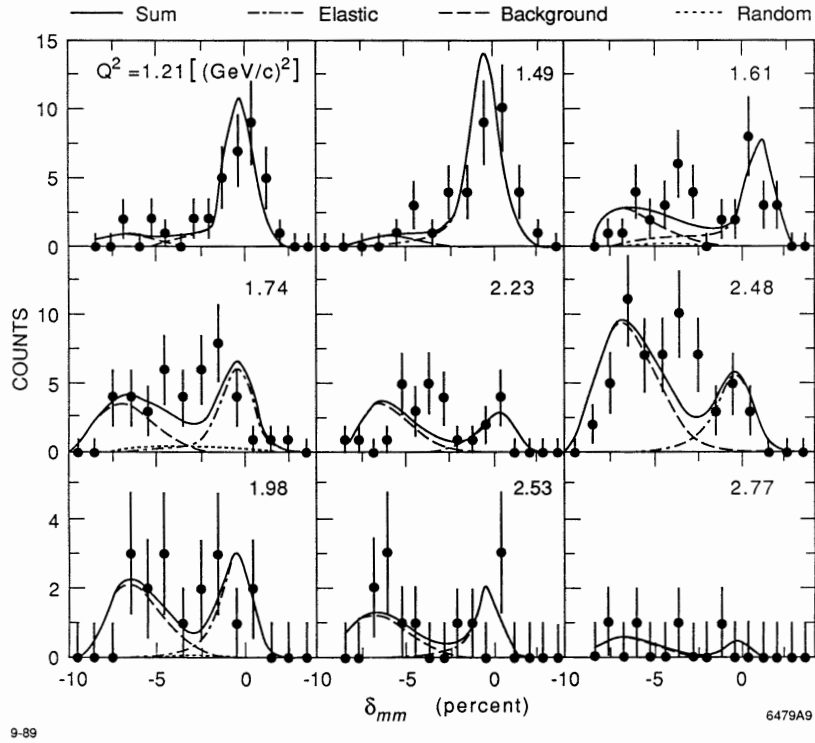


Figure 13: Spectra of elastic electron-deuteron coincidence events versus missing momentum for nine Q^2 kinematics from SLAC experiment NE4 [7] (see text). The Q^2 point 1.21 $(\text{GeV}/c)^2$ used 10 cm target, the Q^2 points 1.49, 1.61, 2.23, 2.53 and 2.77 used 20 cm target, and the Q^2 points 1.74, 1.98 and 2.48 used 40 cm target. The data were fitted to a sum of three curves: elastic scattering, $\gamma d \rightarrow \pi_0 d$ background, and random background. The shapes of the elastic and background curves were determined by Monte Carlo simulation.

It is well known that the deuteron magnetic form factor is extremely sensitive to the details of the theoretical calculations [1, 2, 3]. All non-relativistic calculations show a large sensitivity in the nucleon-nucleon potential used, the modeling in the inclusion of MEC and the possible admixtures of nucleon isobars and six-quark states in the deuteron wave

function. Small variations of unconstrained parameters of the models result in big differences in the location of the diffraction minimum of $B(Q^2)$ and the strength and Q^2 evolution of the secondary maximum. Typical examples on this sensitivity can be found in References [2], [14], [25] and [36]. A similar degree of sensitivity is observed in the relativistic calculations using hamiltonian dynamics or propagator dynamics as it is evident by inspection of Figures 8, 9 and 10 (see also Ref. [51]).

In the most complete study of the deuteron form factors using propagator dynamics with the Gross equation, the VDG group observed that $B(Q^2)$ is extremely sensitive to the presence of small P -state components of the deuteron wave function of relativistic origin. In particular, the position of the minimum of $B(Q^2)$ is very sensitive to the sign of the singlet P state v_s . This observation is very surprising, because the probability of the v_s state is only 0.01%. The reason such a small component can have such a large effect is due to a double interference between the small P states and the larger S - and D -state components. This is easily seen when one considers the decomposition of the magnetic form factor in electric and magnetic parts (similarly to the non-relativistic impulse approximation case):

$$G_M = (G_E^p + G_E^n)D_M^E + (G_M^p + G_M^n)D_M^M, \quad (16)$$

and obtains, to first order in $(Q/M)^2$, the low- Q^2 limit for the relativistic impulse approximation:

$$D_M^E = \int_0^\infty dr \left\{ \frac{3}{2}w^2(r) + \frac{2Mr}{\sqrt{3}} \left[v_t(r) \left(\frac{1}{\sqrt{2}}u(r) - w(r) \right) - v_s(r) \left(u(r) + \frac{1}{\sqrt{2}}w(r) \right) \right] \right\} [j_0(k) + j_2(k)], \quad (17)$$

$$D_M^M = \int_0^\infty dr \left[(2u^2(r) - w^2(r)) j_0(k) + (\sqrt{2}u(r)w(r) + w^2(r)) j_2(k) \right], \quad (18)$$

where v_t is the triplet P state of the relativistic four-component deuteron wave function. All terms quadratic in the P states are very small in this region but the small- P components of the terms in D_M^E interfere with the large components, enhancing the overall effect of the small components. Also if the sign of the v_s component is opposite to that of v_t , the two separate interference terms will add coherently enhancing their effect.

Another source of uncertainty in the VDG model is the off-shell modification of the single-nucleon current. This is necessary to insure current conservation, by satisfying the Ward-

Takahashi identity. The VDG solution of this constraint results in a nucleon electromagnetic current requiring an unconstrained form factor, $F_3(Q^2)$, in addition to the Dirac and Pauli form factors $F_1(Q^2)$ and $F_2(Q^2)$, and three associated, partly constrained, functions of the off-shell virtuality of the nucleon. Recent studies by Van Orden and Gross [20] have shown that the secondary maximum of $B(Q^2)$ is very sensitive to the hardness of the $F_3(Q^2)$ off-shell form factor and that reasonable variations in the $F_3(Q^2)$ choices have a small effect in $\tilde{t}_{20}(Q^2)$ and minimal effect on $A(Q^2)$. This can be seen by comparing the curves of Figures 8 and 9. The solid curve of Figure 9 uses a dipole-type form for the $F_3(Q^2)$ form factor meanwhile the thick-dotted curve uses a tripole-type form.

A third source of uncertainty in the VDG model is the hardness of the $\rho\pi\gamma$ form factor. The particular choice for this form factor has a large effect on $A(Q^2)$ but a small effect on $B(Q^2)$ and almost no effect in $\tilde{t}_{20}(Q^2)$, as can be seen by examination of Figures 8 and 9, given that the VDG, HT and PWD groups use significantly different $\rho\pi\gamma$ form factor choices. Since the above three uncertainties affect primarily three different aspects of the data, namely the location of the $B(Q^2)$ diffraction minimum, the height of the secondary maximum of $B(Q^2)$ and its evolution to larger Q^2 , and the overall magnitude of $A(Q^2)$, a precise measurement of the location of the diffraction minimum and of the height and shape of the secondary maximum of $B(Q^2)$ and beyond, will constrain the theoretical model and provide a consistent description of both elastic form factors $A(Q^2)$ and $B(Q^2)$.

The importance of precise $B(Q^2)$ measurements in discriminating among the differing theoretical calculations is demonstrated in Figure 14, which contains a representative sample of recent propagator and hamiltonian dynamics calculations and an older quark-cluster hybrid model calculation compared to $A(Q^2)$, $B(Q^2)$ and $t_{20}(Q^2)$ data. The theory curves in the Figure are, in order of the Q^2 of their minima in $B(Q^2)$, by: Carbonnel and Karmanov [52] (hamiltonian dynamics/ front-form, long dot-dashed line); Phillips, Wallace and Devine [22] (propagator dynamics, dashed double-dotted line); Allen, Klink and Polyzou [40] (hamiltonian dynamics/point-form, short dot-dashed line); Van Orden and Gross [20] (propagator dynamics/full calculation, solid line); Van Orden, Devine and Gross [20] (propagator dynamics/RIA only, long dashed line); Lev, Pace and Salmè [41] (hamiltonian dynamics/ front-form, dotted line); Dijk and Bakker [25] (quark-cluster hybrid, widely spaced dot-

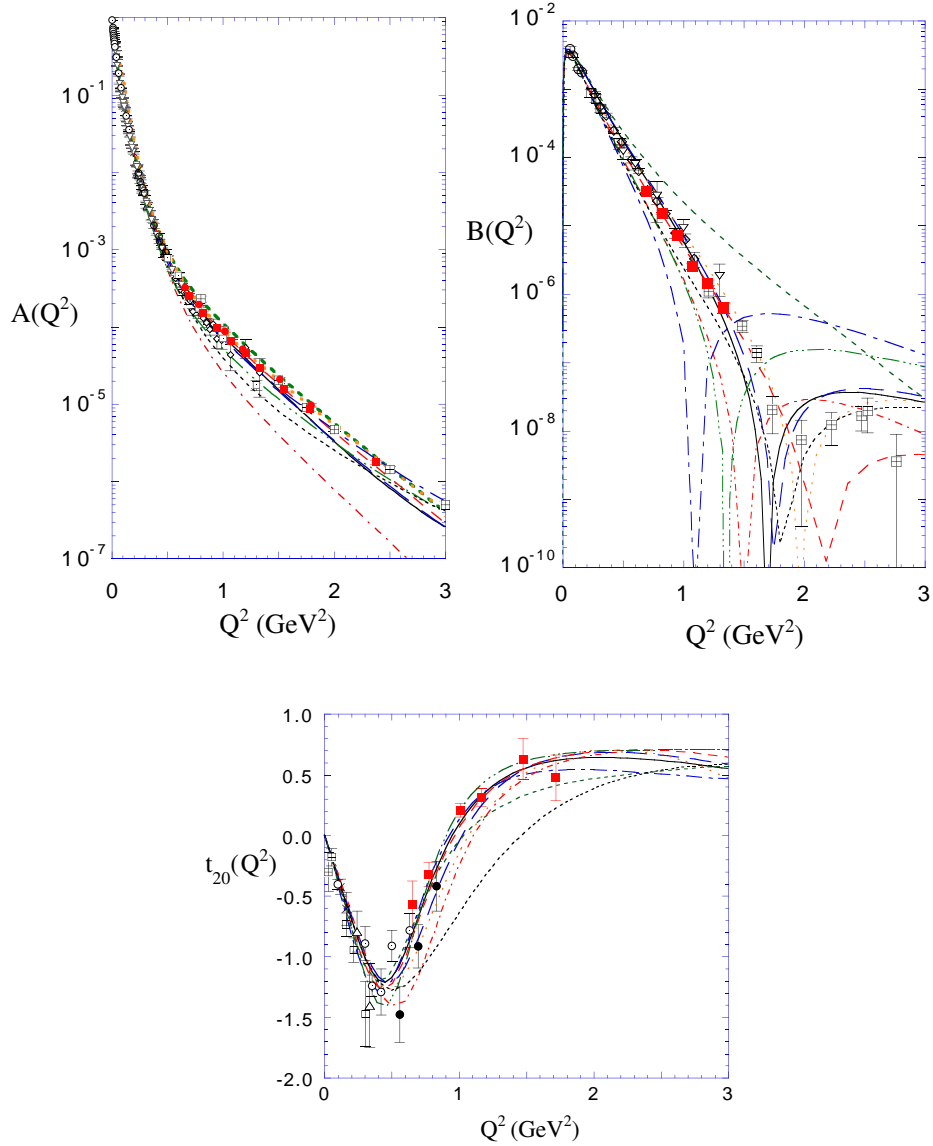


Figure 14: Comparison of available deuteron $A(Q^2)$, $B(Q^2)$ and $t_{20}(Q^2)$ data [6, 7, 10, 11, 31] with selected theoretical calculations [20, 22, 25, 40, 41, 42, 52, 53] (see text). Of note is the large model dependence of the predictions for $B(Q^2)$.

ted line); Schiavilla and Pandharipande [42] (hamiltonian dynamics/instant form, medium dashed line); and Arenhövel, Ritz and Wilbois [53] (hamiltonian dynamics, short dashed line). The “*most striking feature of this plot is the large model dependence of the predictions for $B(Q^2)$* ”, as has been stressed in the review work of Ref. [3]. A new precise measure-

ment of $B(Q^2)$ can obviously provide severe constraints in the parameters of the calculations with an unprecedented discriminative power. The second obvious striking feature of the plot are the very large error bars of the higher Q^2 SLAC data of $B(Q^2)$ that offer a limited discriminative power, necessitating the need for new precise measurements.

The pQCD calculations predict fairly large values for $B(Q^2)$ for $Q^2 > 2.5$ (GeV/c)², easily measurable in a JLab experiment. The expected values are, in general, significantly larger than the ones predicted by conventional non-relativistic or relativistic meson-nucleon calculations. The original pQCD prediction for the ratio $B(Q^2)/A(Q^2)$ by Brodsky and Hiller [29] and its improvement by Kobushkin and Syamtomov [30] are shown in Figure 15. Shown also in the Figure are data from SLAC [7], Bonn [54] and Saclay [55]. A new JLab experiment will offer large Q^2 $B(Q^2)$ data that can provide some finality to the, unresolved for more than a quarter of a century, issue of the applicability of pQCD to the deuteron form factor description and either validate the apparent success of QDS and pQCD in describing $A(Q^2)$, or put it to rest.

It should be noted that there has been a tremendous amount of theoretical work on the deuteron form factors in the last decade and in particular after the publication of the JLab $A(Q^2)$ and $t_{20}(Q^2)$ data. A successful completion of this work will require new improved data on the deuteron $B(Q^2)$ over the Q^2 region of its apparent diffraction minimum and beyond to larger Q^2 to constrain remaining theoretical uncertainties. A JLab measurement of the deuteron $B(Q^2)$ with a precision comparable to the previous $A(Q^2)$ JLab measurements will significantly advance our understanding of the internal structure and dynamics of the deuteron, and quite possibly *establish a canonical consistent hadronic model describing the electromagnetic structure of the deuteron*.

The importance of the previous SLAC and JLab experiments on the deuteron form factors for our understanding of the simplest nucleus in nature is universally accepted. Both the 1990 DOE/NSF Long Range Plan by NSAC [56], which proceeded the SLAC NE4 experiment, and the 2002 Long Range Plan [57], which proceeded the JLab experiments, acknowledged the deuteron form factor measurements as major nuclear physics achievements and called their extensions to the highest momentum transfers possible as essential for the advancement of nuclear physics. While the extension of $A(Q^2)$ [58] will have to wait for the 12 GeV upgrade

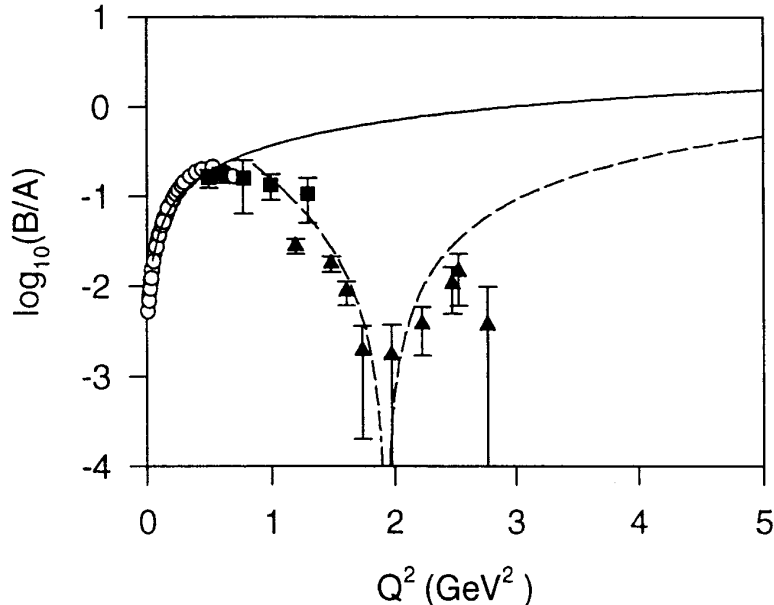


Figure 15: Perturbative QCD predictions for the deuteron $A(Q^2)/B(Q^2)$ ratio. The solid curve is the original calculation by Brodsky and Hiller [29]; the dashed curve includes a correction of order Λ_{QCD}/M_d by Kobushkin and Syamtomov [30]. The data are from SLAC [7] (solid triangles), Bonn [54] (solid squares) and Saclay [55] (open circles).

of JLab and the extension of $t_{20}(Q^2)$ for a major new idea in deuteron polarimetry, the extension of $B(Q^2)$ is presently feasible at JLab.

We are proposing to perform the much needed extension of $B(Q^2)$ by reaching the limits of magnetic elastic scattering from the deuteron accessible by the unique features of JLab. Our objective is to improve significantly the quality of the existing data on the deuteron $B(Q^2)$ around its diffraction minimum and extend the existing measurements to the highest momentum transfers, possibly up to $Q^2 = 6$ $(\text{GeV}/c)^2$, limited only by cross section sensitivity of one elastic event per day [as in the JLab E91-26 experiment on $A(Q^2)$]. The new data will be of significant importance for the development of a canonical theory based on hadronic degrees of freedom describing the electromagnetic structure of the deuteron.

1.5 The Experimental Setup

The existing deuteron form factor data show that, for $Q^2 > 1.5 \text{ (GeV}/c)^2$, the electric form factor is 2 to 3 orders of magnitude greater than the magnetic one, dictating that *any future $B(Q^2)$ measurements for $Q^2 > 1.5 \text{ (GeV}/c)^2$ must be performed at or close to 180°* so that the contribution from $A(Q^2)$ would not dominate the elastic cross section.

The cross section to be measured is known to be small and of the order of 10^{-41} to 10^{-42} cm^2/sr in the vicinity of the diffraction minimum and beyond, requiring i) clean identification of elastic events with detection of both scattered electrons and recoiling deuterons in coincidence, ii) sufficient angular and momentum resolution in the kinematical reconstruction of the events, iii) a double-arm magnetic spectrometer with the largest possible solid angle, and iv) the longest possible target consistent with cryogenic limitations and suppression of the expected photoproduction background.

Deuterons will be detected at a fixed recoil angle of 3.5° in the two High Resolution Spectrometers, placed at their minimum angle of 12.5° . The recoil nuclei will be deflected by 9.0° to the entrance of the two HRSs by a dual-septum dipole magnet placed on the Hall A pivot platform, which normally houses the cryogenic target chamber, as shown in Figure 16. The latter chamber will be pulled upstream by 1.4 m. The electron beam will travel towards the beam dump through a central opening in the dual-septum dipole (see below), shown in Figure 17. Scattered electrons will be measured with two simple backward spectrometers based on two small dipole magnets, shown in Figure 18, placed on both sides of the beam, as shown in Figure 16.

The identification of the electron-recoil nucleus coincidences will rely on double-arm TOF measurements, as in the E91-26/E04-18 [59] elastic experiments on the deuteron/helium isotopes. It is our expectation that the double-arm TOF spectra for this experiment will be free of background, similarly with the electron-deuteron/helium spectra of E91-26/E04-18 experiments. Figure 19 shows a representative sample of E91-26 TOF spectra (after standard timing corrections) in the Q^2 range of 0.7 to 6 $(\text{GeV}/c)^2$ [60].

The presence of double-arm electron-deuteron coincidences from the two-step photoproduction background processes observed in SLAC experiment NE4 will be significantly sup-

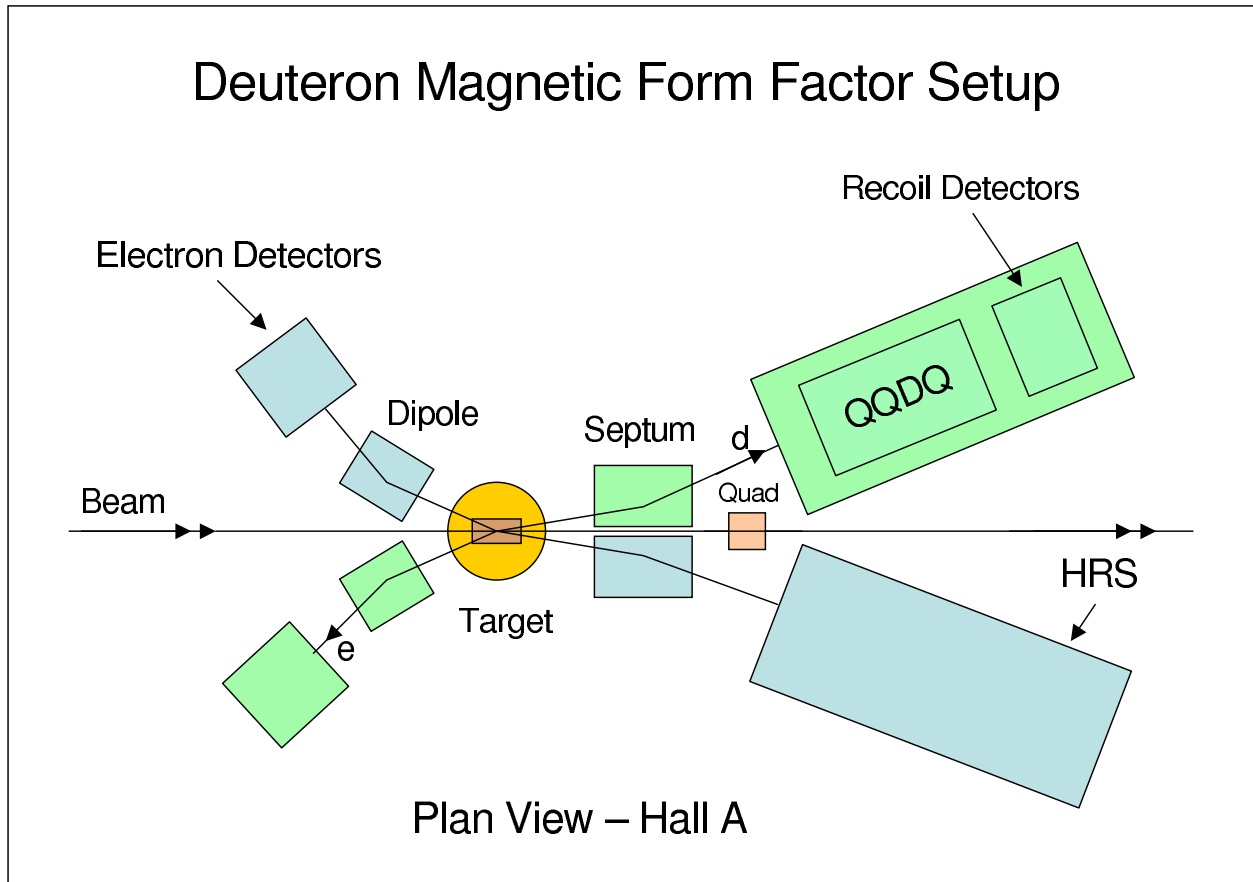


Figure 16: The dual double-arm spectrometer system for the measurement of the deuteron, proton and ^3He magnetic form factors (not to scale). Scattered electrons are detected at backward angles (153° - 172°) in two spectrometers based on two small dipole magnets. Recoil nuclei are detected at a fixed angle of 3.5° in the two High Resolution spectrometers of Hall A, placed at 12.5° with respect to the beam line, after a 9° deflection by a dual-septum dipole magnet (see text).

pressed in this experiment. This background, being at least proportional to the square of the target length, will be reduced by one order of magnitude as compared to SLAC NE4, using a target length of 10 cm, much shorter than the 20 and 40 cm target lengths used at SLAC. The outstanding angular and momentum resolutions of the recoil spectrometers will provide clean separation of elastic and photoproduction deuterons, further suppressing any remaining background close to the elastic peak. Application of cuts in the angular elastic

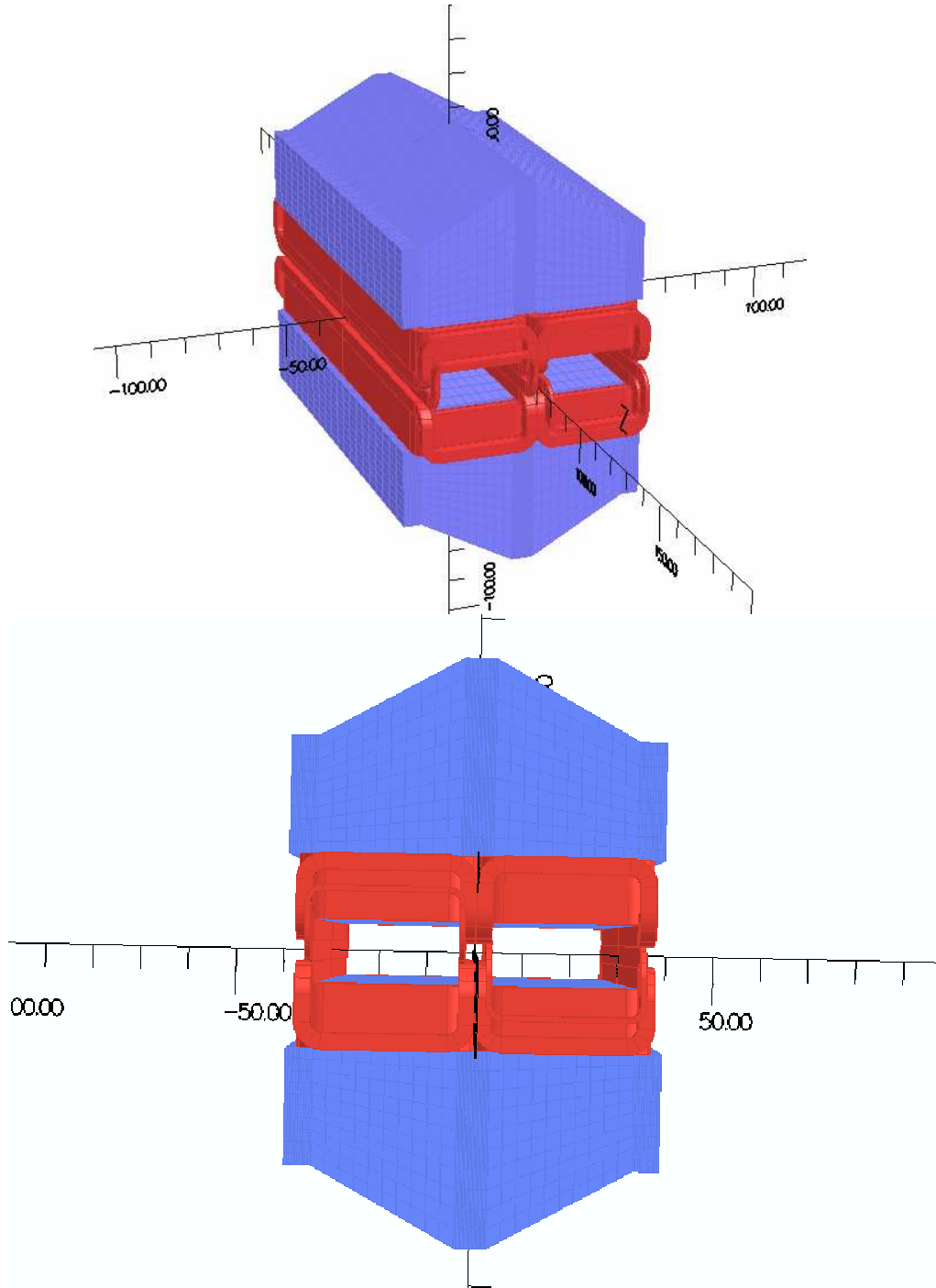


Figure 17: Side and front (target) view of the iron yoke (top and bottom) and coils (middle) of the dual-septum dipole magnet that deflects nuclei recoiling around 3.5° to the two HRS systems through its left and right openings. The beam travels to the Hall A dump through the central opening of the magnet.

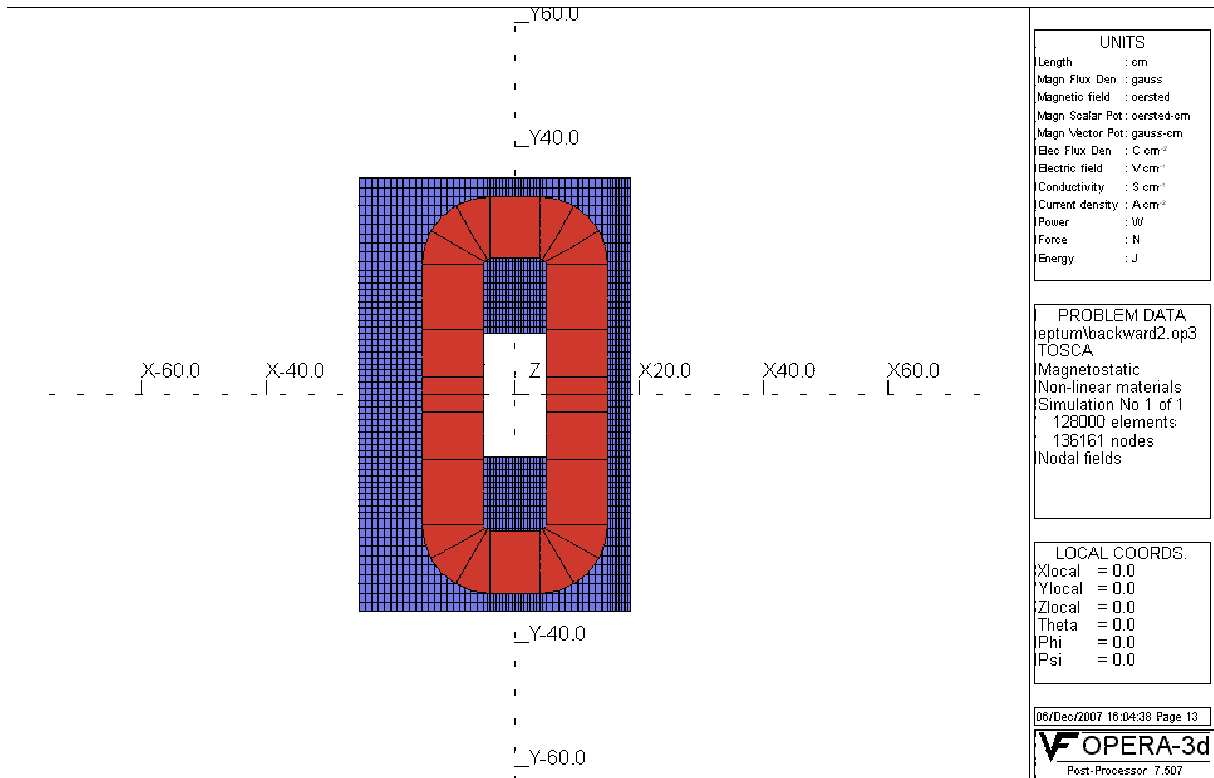


Figure 18: Front (target) view of one of the two small dipole magnets of the backward electron spectrometers. Seen are the iron yoke and the coils.

correlation of the scattered and recoil particles (not applied in the SLAC experiment because of the poor resolution of its recoil spectrometer), in particular in the vertical direction, will ensure the total elimination of any remaining background events.

The kinematical coordinates of the coincidence elastic events will be determined from the 3.5° spectrometers' recoil nucleus coordinates. The electron detection in coincidence will tag and ensure the nature of the elastic events. The calibration of the entire double-arm system will be checked with elastic electron-proton scattering in coincidence. Elastic scattering from hydrogen will be measured at every kinematical point of the elastic deuteron scattering. The double-arm solid angle will be calculated by means of Monte Carlo simulation as was done for the SLAC NE4 experiment on $B(Q^2)$ and for the JLab E91-26 Hall A experiment on

$A(Q^2)$ [33, 35]. Details on the essential elements of the simulation method are given in the Appendix.

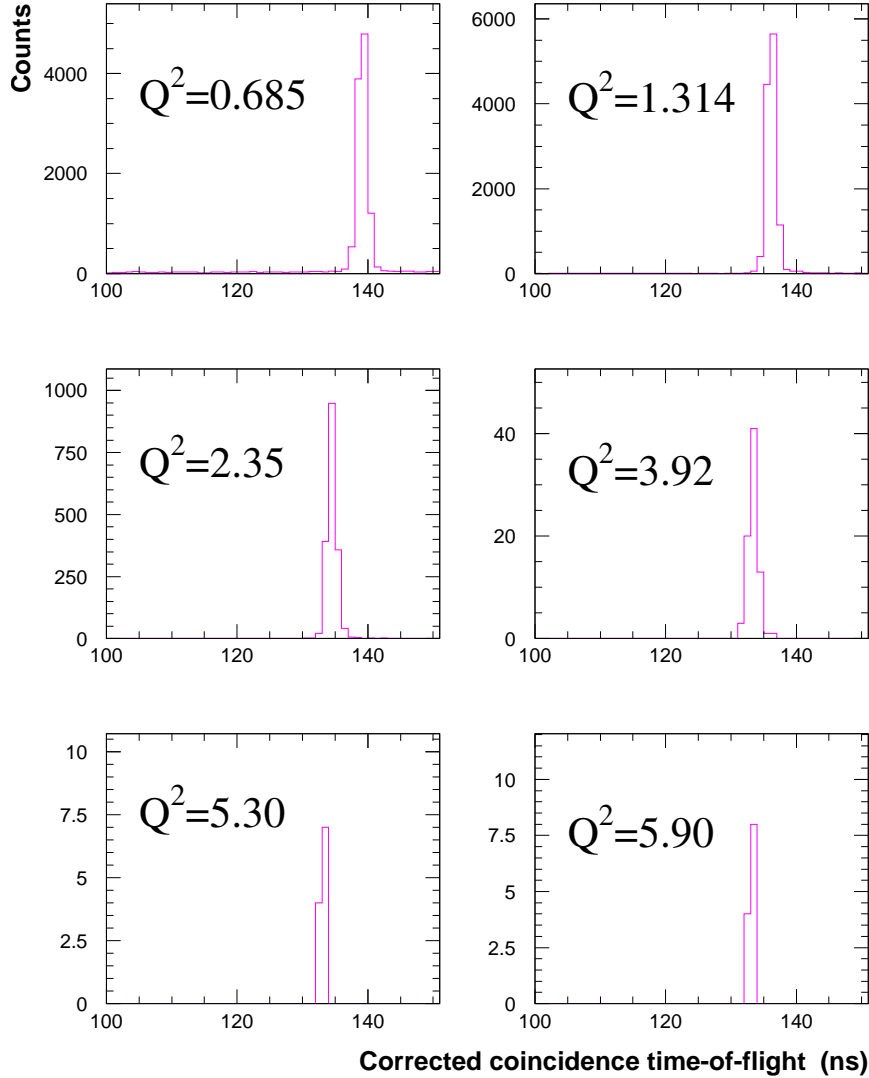


Figure 19: Electron-deuteron coincidence TOF spectra for six Q^2 kinematics (including the lowest and highest ones) from JLab Hall A elastic electron-deuteron scattering experiment E91-26, after applying standard timing corrections [60].

The experiment will require three target cells, a 5 cm long one for hydrogen and ^3He measurements, a 10 cm long for deuterium measurements, and a 15 cm one for ^3He measurements. The large angular range of the scattered electrons dictate use of the convenient

tuna-can target cell geometry, used successfully in other experiments in the past. The tested cooling capability of Hall A can allow use of beam currents as high as $150\mu\text{A}$ for a 10 cm long deuterium target. For the purpose of this proposal we assume a beam current of $120\mu\text{A}$ for the deuteron and helium measurements (as for the case of Hall Experiment E91-26, which used a 15 cm long deuterium target), and up to $60\mu\text{A}$ for the hydrogen measurements. Beam-intensity induced changes in the density of liquid hydrogen and deuterium (gas helium) targets have been measured to be, under similar conditions in Hall A, on the order of a few (several) percent, resulting in a fractional cross section error of $< \pm 0.5$ (1.0)%.

1.5.1 The Dual 3.5° Recoil Spectrometers

The recoiling nuclei will be detected in the two High Resolution Spectrometers after being deflected by 9° in the two left and right gaps/openings of the dual-septum dipole, shown in Figure 17. This septum has been designed by Mr. Paul Brinza, JLab Engineer [61]. It will be a symmetric, iron-dominated magnet, with identical, very uniform magnetic fields in its two gaps. The length of the iron yoke is 1.1 m and the maximum integrated magnetic field is 1.6 T·m, with an effective length of 1.2 m. The dimensions of each gap are 30 cm horizontally by 12 cm vertically. The magnet will be powered by the existing BigBite power supply. Detailed magnetic measurements will be performed prior to the installation of this magnet and a complete field map will be produced as a function of current.

In order to be able to use the HRSs with their permanent pointing to the Hall A target pivot center, the target assembly will be moved by 1.4 m upstream from its nominal position on the Hall A pivot, with the two HRSs pointing towards the dual-septum, placed in the vicinity of the target pivot. The distance between the exit of the septum and the entrance of the first HRS quadrupole is 0.49 m. The collimator multi-function box in front of each HRS will be removed and a single aperture/solid angle-defining collimator will be placed inside the vacuum pipe of each first HRS quadrupole. To block the large flux of forward bremsstrahlung photons, originating in the target, from propagating through the vacuum pipe of the two recoil spectrometers, two fixed-aperture photon collimators will be placed in front of the two openings of the septum magnet.

Each half of the dual-septum becomes an additional magnetic dipole element of the optics of the HRS system, with the distance of its first quadrupole from the target center increased from 1.6 to 3.1 m. A new optics configuration has been developed to i) achieve a desired recoil solid angle of 1.5 msr, with vertical (horizontal) angular acceptance of 24 (15) mr and ii) preserve the excellent momentum and angular resolutions of the standard HRS optics configuration. The optics is point to point in the dispersive (vertical) plane (the transported particle's position along a momentum focal plane is proportional to its momentum) and parallel to point in the transverse (horizontal) plane (the transported particle's position along an angular focal plane is proportional to its production angle). The momentum and horizontal angle focal planes are at the same position, in the drift chambers, with the position of the momentum focal plane of the standard HRS tune (this latter tune has no angle focal plane). The operating gradients of the three HRS quadrupoles, Q_1 , Q_2 and Q_3 , will be $0.429g_1$, $0.896g_2$ and $1.12g_3$, where g_1 , g_2 and g_3 are the gradients of the standard HRS tune. The first order transformation equations for the exit TRANSPORT [62] coordinates (x , θ : horizontal; y , ϕ : vertical) of the particles at the drift chambers, in terms of the target coordinates (x_o , θ_o : horizontal; y_o , ϕ_o : vertical; δ_o : relative momentum) are:

$$\begin{pmatrix} x \\ \theta \\ y \\ \phi \end{pmatrix} = \begin{pmatrix} 0.00 & -0.12 & 0.00 & 0.00 & 0.18 \\ 8.54 & 0.18 & 0.00 & 0.00 & 2.34 \\ 0.00 & 0.00 & -1.24 & 0.00 & 12.8 \\ 0.00 & 0.00 & -1.88 & -0.80 & 21.7 \end{pmatrix} \begin{pmatrix} x_o \\ \theta_o \\ y_o \\ \phi_o \\ \delta_o \end{pmatrix} \quad (19)$$

For comparison, the corresponding matrix transformation of the nominal HRS tune is:

$$\begin{pmatrix} x \\ \theta \\ y \\ \phi \end{pmatrix} = \begin{pmatrix} -0.62 & -0.08 & 0.00 & 0.00 & 0.00 \\ 3.83 & -1.09 & 0.00 & 0.00 & 0.00 \\ 0.00 & 0.00 & -1.95 & -0.06 & 11.9 \\ 0.00 & 0.00 & -0.63 & -0.53 & 19.6 \end{pmatrix} \begin{pmatrix} x_o \\ \theta_o \\ y_o \\ \phi_o \\ \delta_o \end{pmatrix} \quad (20)$$

It can be seen that the intrinsic momentum resolution of the modified HRS will be better by about a factor of 2, as the D/M (dispersion over magnification) almost doubles

(12.8/1.24=10.2 versus 11.9/1.95=6.1), as compared to the standard HRS tune. For a beam raster size of ± 0.15 cm incident on a 10 cm target viewed by the HRS at 3.5° , the momentum resolution of the modified (standard) HRS is $\pm 0.017\%$ ($\pm 0.038\%$), for 4 (GeV/ c) particles. The angular resolutions depend on the central spectrometer momentum due to multiple scattering effects in the HRS exit vacuum window and the drift chambers. They are also better by more than a factor of 2 for the modified HRS, as compared to the nominal HRS tune. For comparison, the intrinsic angular resolutions of the modified (standard) HRS tune are, for the 1.9 (GeV/ c) recoil momentum of the middle $Q^2 = 3$ (GeV/ c)² proposed deuteron kinematics (see Table 1), ± 0.3 (0.9) mr in the horizontal and ± 1.9 (3.8) mr in the vertical direction. The total effective angular resolutions will grow due to multiple scattering effects in the target (*e.g.* ± 0.8 mr in both vertical and horizontal directions for the deuteron momentum of 1.9 (GeV/ c), but they will be more than sufficient for the needs of this experiment.

The incident electron beam will travel straight to the beam dump of the Hall through the central opening of the dual septum (which is, in the current design, $\sim 4 \times 4$ cm²). There is no dipole field along the beam-line axis, but there is a quadrupole field estimated to be ~ 40 (130) G/mm at the lowest (highest) Q^2 deuteron kinematics, corresponding to a beam energy of $E = 0.59$ (2.1) GeV, or, on the average, a gradient of ~ 65 G/mm/GeV, normalized to beam energy. To compensate for the beam phase-space growth caused by this quadrupole field, a small separate quadrupole, running in opposite polarity, will be placed in the 0.5 m space available between the septum magnet and the two first quadrupoles of the two HRS systems, as shown in Figure 16.

The recoil nucleus detection will require a subset of the full detector package of each HRS. The two planes of scintillators, S1 and S2, and the vertical drift chambers (VDC) will suffice for TOF measurements and for the reconstruction of the recoil nucleus momentum and recoil angle. The candidate recoil signal used for triggering and for double-arm TOF measurements will be formed by the coincidence of the signals of the two scintillator planes. To improve the single-arm TOF separation between deuterons and protons, the distance between the two scintillator planes will be increased from 2 to 4 m by moving the S2 plane downstream. Additional discrimination between protons and deuterons will be provided by

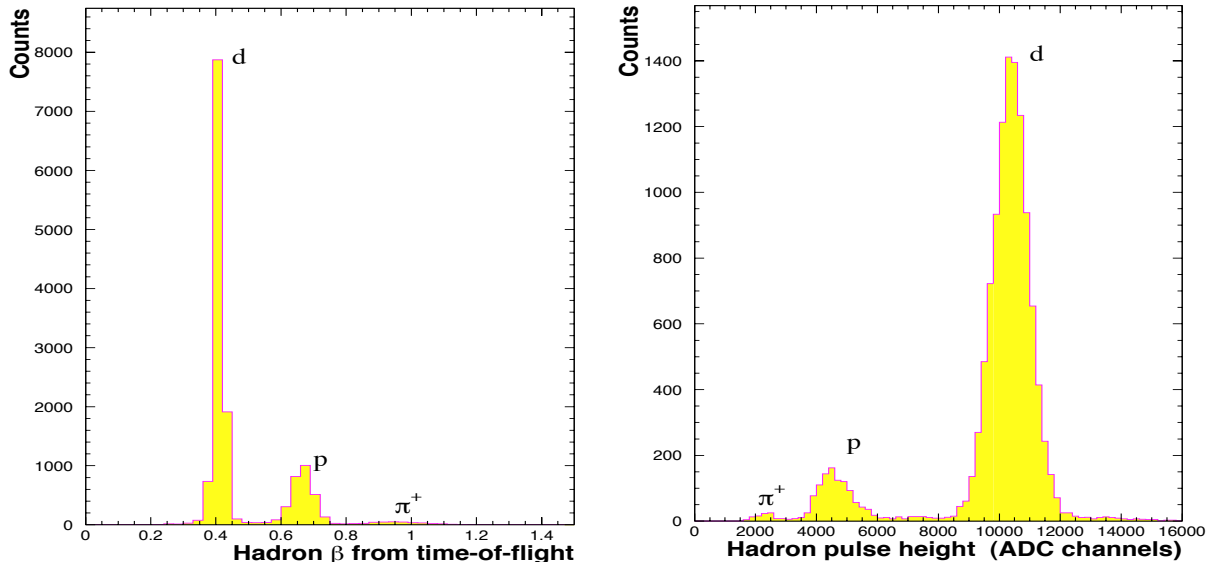


Figure 20: Hadron identification by the two planes of scintillators in the E91-26 experiment that measured the deuteron $A(Q^2)$ in JLab Hall A: a) Measured speed of hadrons detected in the recoil HRS system, b) ADC spectrum of the 1st plane of the recoil HRS scintillators. The central spectrometer momentum was 0.84 (GeV/c) [60].

the ADC pulse heights of their scintillator signals. The system of the two scintillator planes has performed admirably so far in past Hall A experiments, as shown, for one of the E91-26 $A(Q^2)$ measurements [60], in Figure 20. The timing resolution in the single arm TOF measurements was about 0.5 ns (rms).

1.5.2 The Dual Backward Electron Spectrometers

Each electron spectrometer will be comprised of a small single, also iron-dominated, dipole magnet, shown in Figure 18, also designed by Mr. Paul Brindza, and a set of detectors about 2 m away from the dipole. The dipole magnets will put the detectors out of the direct view of the target, and sweep away all scattered electrons and background pions outside their $\sim 25\%$ momentum acceptance. The length of each magnet will be 0.35 m, providing an integrated field of 0.5 T·m. The opening of the magnet will have a horizontal width of 13 cm and a vertical gap of 20 cm. It is assumed, that since the two magnets for the backward

spectrometers are identical, they can run by a single power supply, in series or parallel, available at JLab. Detailed magnetic measurements will be performed for this magnet too, prior to its installation, and a complete field map will be produced as a function of current. Also, an aperture/solid angle-defining collimator in the horizontal direction, of remotely controlled variable width, will be placed in front of each dipole.

Since the recoil spectrometers will be at a fixed angle (3.5°), the angle of the electron spectrometers will have to change with each elastic kinematic setting (see Tables 1, 3 and 5). This will be accomplished by putting the magnet and detector package of each spectrometer on a remotely controlled platform, rotating about the target center. The required angular range is 165° - 170° for electron-deuteron scattering, 153° - 170° for electron-proton scattering, and 170° - 172° for electron- ^3He scattering.

As the electron backward-scattering angle decreases with increasing Q^2 , to maximize the solid angle of each backward spectrometer setting, the two dipole magnets should move towards the target. The maximum (minimum) solid angle of each spectrometer, which corresponds to the largest (smallest) Q^2 for the deuteron target, is 25 (10) msr. This movement range is up to 30 cm. The closest position of the entrance of each dipole from the target is, for the largest deuteron Q^2 setting, 70 cm. The changing position of the dipoles' exit optical axis (parallel translation) will necessitate moving at the same time the detector packages with the axis (in a direction always perpendicular to the dipoles' axis). This range of this movement is up to 10 cm. It is assumed that both of these movements will be remotely controlled.

Each electron detection package will consist of i) a segmented electromagnetic calorimeter in a fly's eye configuration, assembled from 24 existing Hall A lead-glass blocks, for electron identification and background pion rejection, and ii) a finely segmented scintillator hodoscope, with fingers running along both the horizontal and vertical directions, for triggering and double-arm TOF measurements, and for the reconstruction of the electron scattering angle. A request has been made to the Stanford Linear Accelerator to borrow and use a small subset (~ 100) of the hundreds of elements of the compact hodoscopes used in the End Station A nucleon spin physics program. The required cross sectional area of the detector package is 35 cm (horizontal) by 70 cm (vertical).

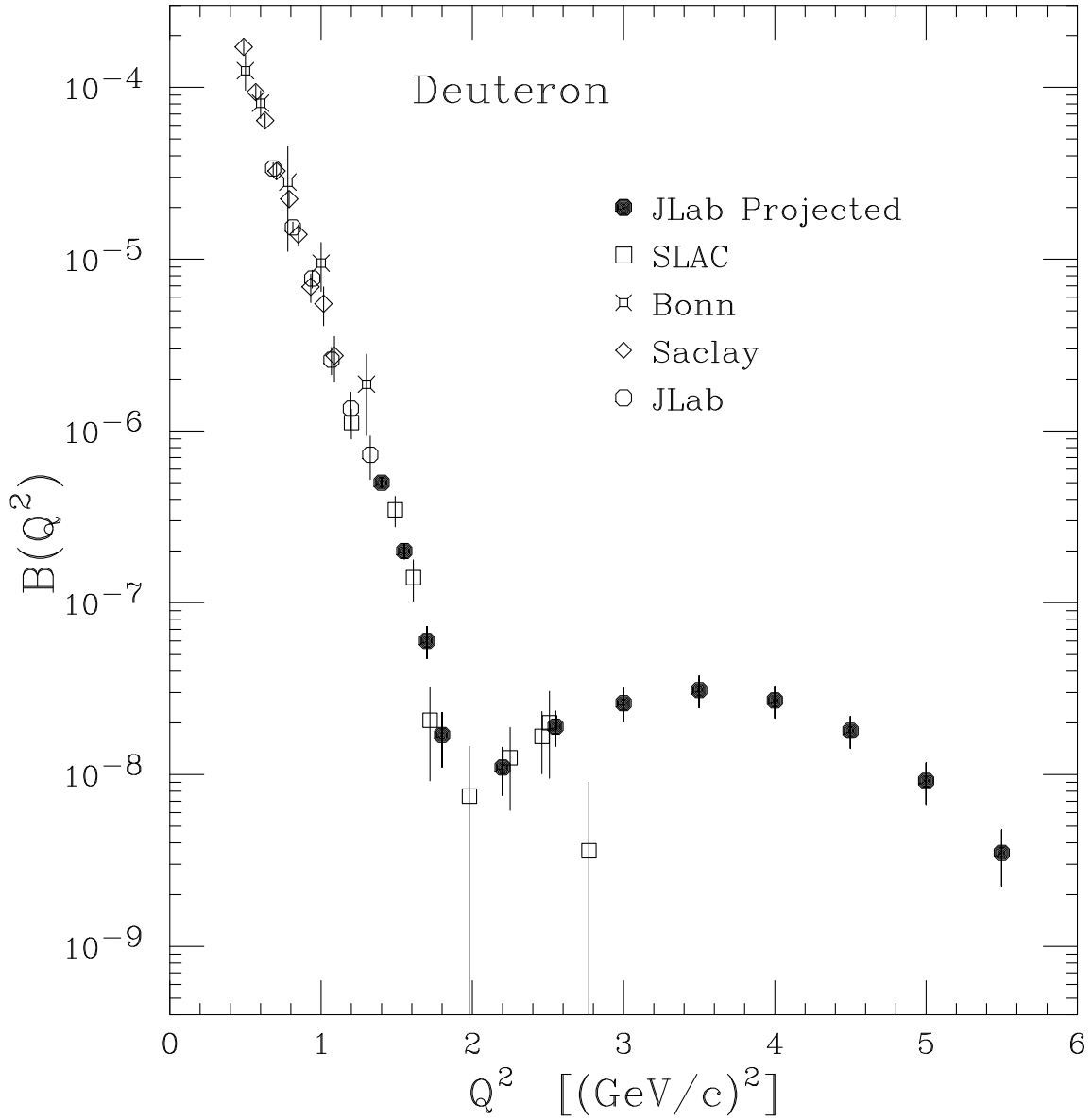


Figure 21: Projected deuteron magnetic form factor $B(Q^2)$ data from the proposed experiment. Also shown are recent JLab data [31] and older data from Bonn, Saclay and SLAC [7].

The calorimeter blocks are of the SF5 type with radiation length of 2.5 cm, and have dimensions $15 \times 15 \times 35$ cm³. The physical length of the blocks amounts to 14 radiation lengths, which will more than meet the standard design feature of having at least 98% containment of the longitudinal development of the shower in the calorimeter. The ~ 2 cm width of the above SLAC scintillator elements is ideal for the reconstruction of the electron

angular coordinates, and for allowing for very strict cuts to be put in the angular correlation of electron-deuteron coincidence events. In the vertical plane, in particular, the electron angular resolution will be dominated by multiple scattering in the target, rather than the width of the scintillator fingers. The candidate electron signal used for triggering and for double-arm TOF measurements will be a 3-fold coincidence of the signals of four scintillator planes. Each detector package will be surrounded by a layer of lead bricks to protect them from room background. The data acquisition system of the backward spectrometers will use the existing electronics and racks of the BigBite Spectrometer.

1.6 The Deuteron Proposed Measurements

The kinematical parameters of elastic electron-deuteron scattering in coincidence are given, for a Θ_r recoil angle of 3.5° , and for the Q^2 range from 1.4 to 6.0 $(\text{GeV}/c)^2$, in Table 1. The required beam energy range is 0.81 to 2.27 GeV. The scattered electron energy E' will be in the range of 0.44 to 0.67 GeV, and the recoil deuteron momentum P_r will be in the range of 1.24 to 2.93 GeV/c . The electron scattering angle Θ will be in the range 170° to 165° . The last column in the Table is the ratio of the electron to deuteron differential solid angle elements (Jacobian transformation of the solid angle for recoil detection).

To estimate the counting rates and required beam times we have assumed a beam current of $120 \mu\text{A}$, a liquid deuterium target with length of 10 cm and density of $0.162 \text{ g}/\text{cm}^3$, a total variable geometric solid angle for the two electron spectrometers ranging from 50 (20) msr at the highest (lowest) Q^2 kinematics, and a radiative correction factor of 0.8. The cross section values used for $Q^2 \geq 2.5 (\text{GeV}/c)^2$ assume a magnetic form factor behavior that follows the general trend of most recent relativistic calculations. They are given, along with counting rates, running times and projected uncertainties in the extraction of $B(Q^2)$, in Table 2. The magnetic form factor error, $\Delta B(Q^2)$, includes both statistical and systematic uncertainties. The overall elastic electron-deuteron cross section systematic uncertainty is estimated to be, based on the E91-26 $A(Q^2)$ measurement experience, $\sim \pm 3\%$ and is dominated by nuclear interactions of the recoil deuterons in the target and the detectors, and by the uncertainty in the double-arm solid angle. The uncertainty of the previously measured $A(Q^2)$ has been

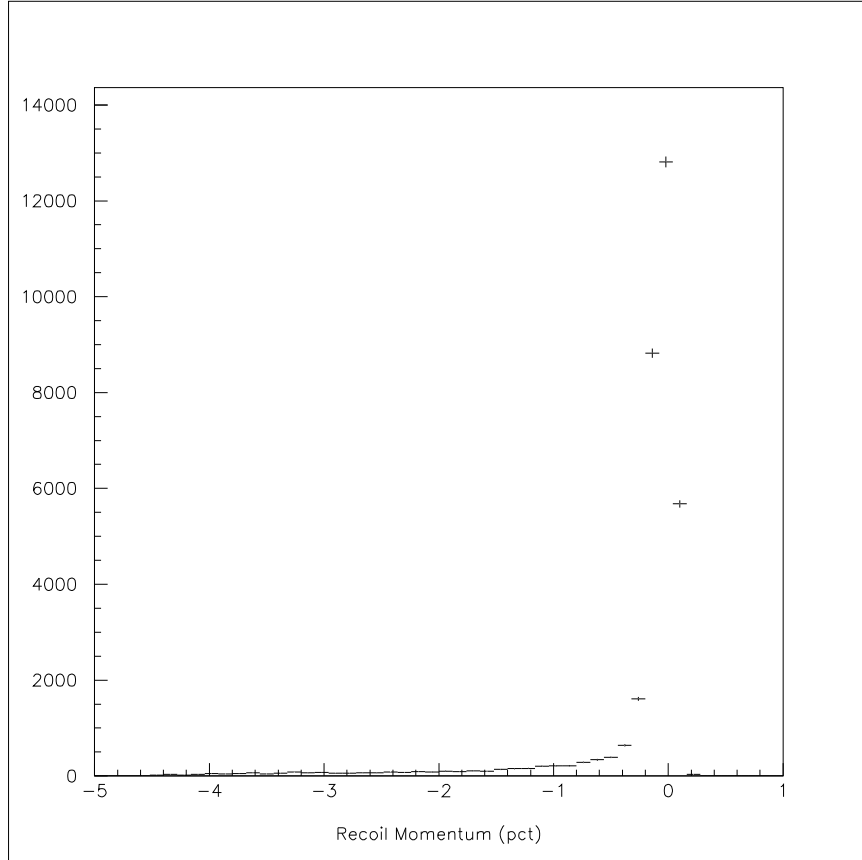


Figure 22: Deuteron elastic peak Monte Carlo simulation: the reconstructed relative momentum (with respect to the central spectrometer momentum) of the recoil deuterons for the middle $Q^2 = 3 \text{ (GeV}/c)^2$ point of the proposed data set.

also included in the calculation. This uncertainty ranges from $\pm 3.5\%$ at $Q^2 = 1 \text{ (GeV}/c)^2$ to $\pm 15\%$ at $Q^2 = 5.5 \text{ (GeV}/c)^2$. The estimated time required to measure $B(Q^2)$ to the maximum Q^2 possible and to map satisfactorily its diffraction minimum is 32 days. The quality of the projected data possible from this proposed experiment is shown, for the above assumptions, in Figure 21. It is evident from the Figure that the proposed $B(Q^2)$ data will be of unprecedented precision, comparable to the precision of the previous $A(Q^2)$ and $t_{20}(Q^2)$ JLab data.

The effective double-arm solid angle for the determination of the elastic cross section will be determined by means of a Monte Carlo simulation of elastic electron-nucleus scattering with the two HRS spectrometers. A brief essential description of the simulation method is

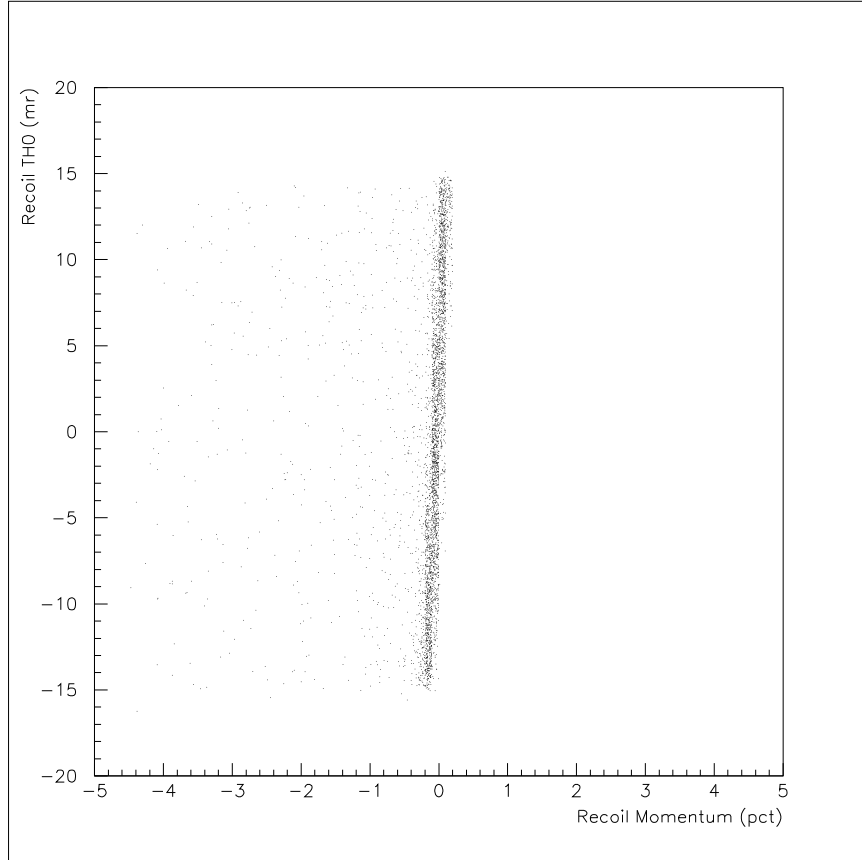


Figure 23: Deuteron elastic peak Monte Carlo simulation: the horizontal recoil angle component of the deuterons versus their relative momentum (with respect to the central spectrometer momentum), as seen by the recoil spectrometer, for the middle $Q^2 = 3 \text{ (GeV}/c)^2$ point of the proposed data set.

given in the Appendix. The elastic cross section for the central values E_o and Θ_o will be determined as:

$$\frac{d\sigma}{d\Omega}(E_o, \Theta_o) = \frac{N_{er}}{N_b N_t C F(Q^2, T) P_{MC}}, \quad (21)$$

where N_{er} is the number of electron-recoil nucleus coincidence events, N_b is the number of incident beam electrons, N_t is the number of target nuclei per cm^2 , C is a factor correcting for computer dead-time effects, detector inefficiencies, and absorption of recoil nuclei in the target and the detectors. The function $F(Q^2, T)$ is the portion of radiative corrections that is independent of the momentum acceptances of the electron and recoil spectrometers, with T being the total average radiator path length of the incident and scattered electrons in the

target. The factor P_{MC} is the effective double-arm solid angle simulated integral:

$$P_{MC} = \left\langle \int \int G(E, E', \Theta, t) d\Omega dE' \right\rangle_{E,l}, \quad (22)$$

where the function $G(E, E', \Theta, t)$ includes the momentum acceptance-dependent internal and external radiative effects for the incident and scattered electrons, ionization energy losses by the electrons and the recoil nuclei, and multiple scattering effects for all particles (see Appendix). The parameter t is the position of the scattering vertex of the elastic event along the target length l . The bracket enclosure indicates that the integral is averaged over the energy distribution of the incident beam and over the length of the target.

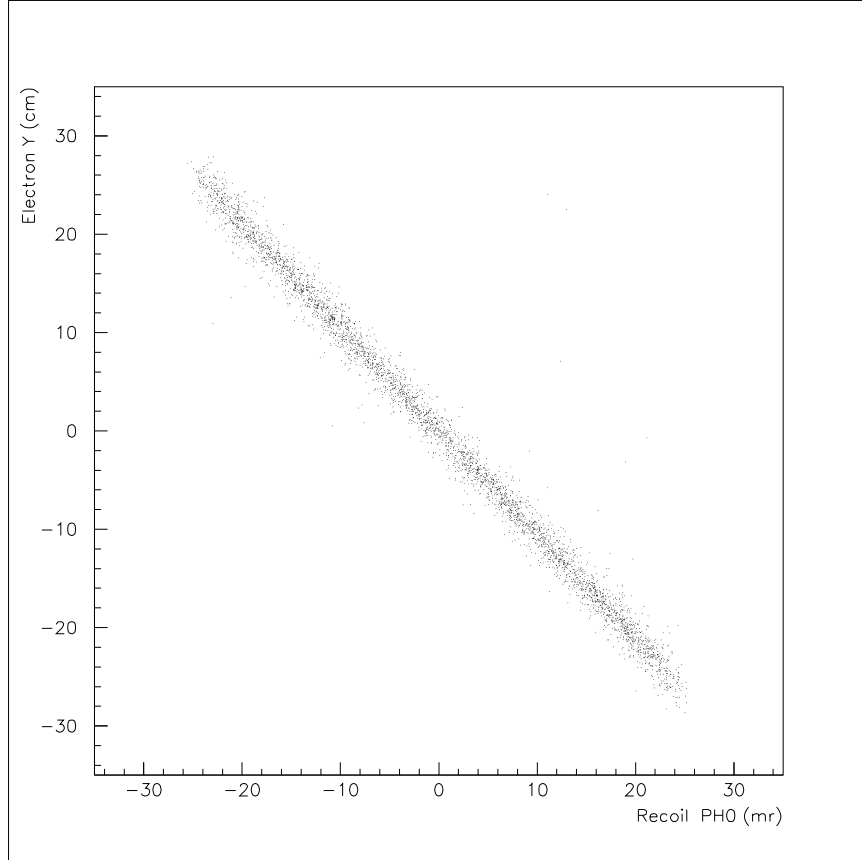


Figure 24: Deuteron elastic peak Monte Carlo simulation: the HRS-reconstructed vertical recoil deuteron angle component versus the raw scattered electron vertical position at the hodoscope of the backward spectrometer, for the middle $Q^2 = 3 \text{ (GeV}/c)^2$ point of the proposed data set.

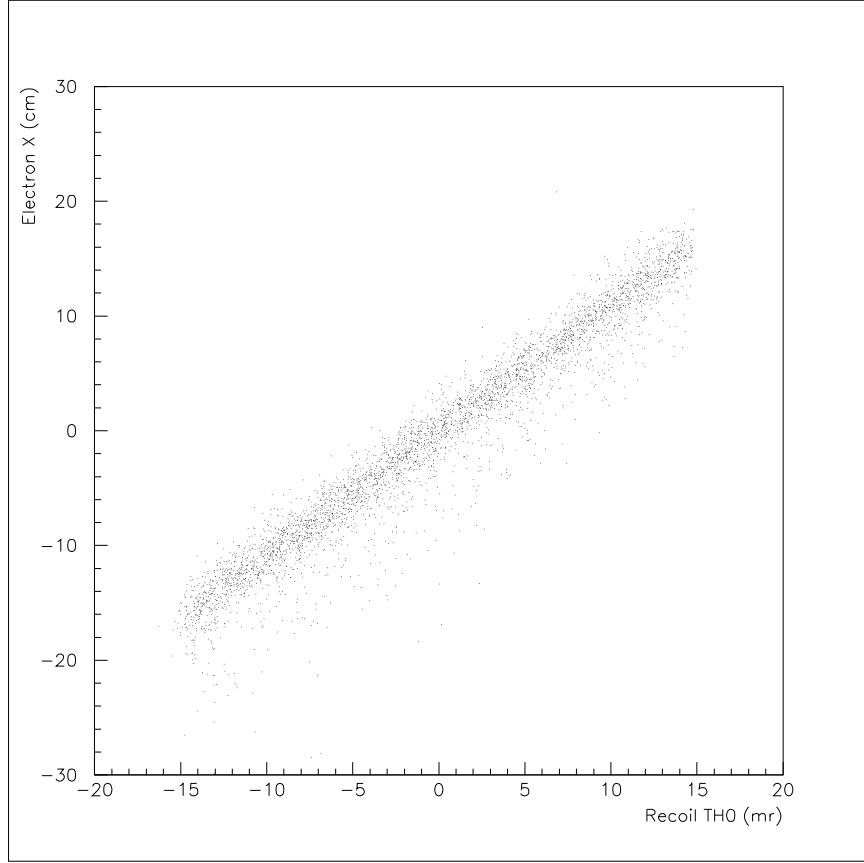


Figure 25: Deuteron elastic peak Monte Carlo simulation: the HRS-reconstructed horizontal recoil deuteron angle component versus the raw scattered electron horizontal position at the hodoscope of the backward spectrometer, for the middle $Q^2 = 3 \text{ (GeV}/c)^2$ point of the proposed data set.

Figure 22 shows the Monte Carlo simulation of the recoil deuteron momentum (relative to the central spectrometer momentum) for elastic scattering for the middle $Q^2 = 3 \text{ (GeV}/c)^2$ point of the proposed data set. Figure 23 shows the simulation of the recoil deuteron relative momentum versus the recoil angle component in the horizontal plane for the same kinematics. It can be seen that the width of the elastic momentum stripe has a $\sigma = 0.04\%$. The threshold for deuterons from the $\gamma d \rightarrow \pi_0 d$ reaction is more than 10σ away from the centroid of the stripe. The Monte Carlo simulation of the angular correlation of scattered electrons and recoil deuterons is shown in Figures 24 and 25. The very clear correlation

of the angular coordinates of recoil deuterons and scattered electrons (translated as position in the electron spectrometer hodoscope) will impose severe cuts for the rejection of background coincidence events. The simulation took into account the effects of a) Landau ionization energy loss for the incident/scattered electrons and recoil nuclei, b) internal and external bremsstrahlung radiation for both incident and scattered electrons, and c) multiple scattering for the incident/scattered electrons and recoil nuclei (see Appendix).

2 Precision Measurement of the Proton Magnetic Form Factor

2.1 Short Review of the Proton Form Factors

The proposed experimental setup will be also ideal to perform precise elastic electron-proton scattering at very backward angles. At these angles, the cross section is dominated by the proton magnetic form factor G_M^p . The electric form factor G_E^p contribution is very small, allowing essentially a direct measurement of G_M^p , without the need of a Rosenbluth separation, which introduces inherent systematic uncertainties. The cross section for elastic electron-proton scattering is given, in the one-photon exchange approximation, by:

$$\frac{d\sigma}{d\Omega}(E, \Theta) = \frac{\alpha^2 E'}{4E^3 \sin^4\left(\frac{\Theta}{2}\right)} \left[A(Q^2) \cos^2\left(\frac{\Theta}{2}\right) + B(Q^2) \sin^2\left(\frac{\Theta}{2}\right) \right], \quad (23)$$

where, in this case, the elastic structure functions $A(Q^2)$ and $B(Q^2)$ are given in terms of $G_E^p(Q^2)$ and $G_M^p(Q^2)$ as:

$$A(Q^2) = \frac{(G_E^p)^2 + \tau(G_M^p)^2}{1 + \tau}, \quad (24)$$

$$B(Q^2) = 2\tau(G_M^p)^2. \quad (25)$$

In the non relativistic limit, G_E^p and G_M^p are the Fourier transforms of the charge and magnetization distributions of the proton in the Breit frame (center-of-mass frame for elastic electron-nucleus scattering). They are related to the Dirac and Pauli form factors $F_1(Q^2)$ and $F_2(Q^2)$ by: $G_E^p = F_1 - \tau\kappa F_2$ and $G_M^p = F_1 + \kappa F_2$, where κ is the proton anomalous magnetic moment. The Dirac form factor is related to the distribution of charge and the normal part of the magnetic moment μ of the proton. The Pauli form factor is related to the distribution of the anomalous part of the magnetic moment.

The starting point in the theoretical description of the nucleon form factors is the Vector Meson Dominance (VMD) model. In this framework, applicable to low and moderate momentum transfers, the virtual photon couples to the nucleon through vector mesons, and the nucleon form factors are expressed in terms of photon-meson coupling strengths, $C_{\gamma V}$, and meson-nucleon vertex form factors, F_{VN} :

$$F(Q^2) = \sum_i \frac{m_i^2 C_{\gamma V_i}}{m_i^2 + Q^2} F_{V_i N}(Q^2) , \quad (26)$$

where the sum is over all possible vector mesons of mass m_i . The early VMD models by Iachello *et al.* [63] and Höhler *et al.* [64], though with flexibility in the choice of parameters, offered fair descriptions of the then available nucleon form factor data. Later on, Gari and Krümpelmann (GK) [65] developed a hybrid phenomenological model to extend VMD to large momentum transfers by synthesizing in a direct way the meson picture of VMD and the asymptotic features of pQCD (see below) using parametrizations of the form factors which properly combine these two approaches, with a transition from meson dynamics to quark dynamics at ~ 5 (GeV/ c)². In recent years, the VMD approach has been revisited by Bijker and Iachello (BI) [66], Hammer and Meissner (HM) [67], and Lomon [68]. The BI calculation includes, in addition to ρ , ω and ϕ meson terms, an intrinsic three-quark structure phenomenological contribution, and has built-in the asymptotic behavior expected from pQCD. The HM calculation includes isovector $\pi\pi$ continuum contribution as in Ref. [64] (and more recently [69] $\rho\pi$ and $K\bar{K}$ contributions), as well as asymptotic constraints from pQCD. All of these recent models describe, in general, satisfactorily the available data.

With the advent of the quark-parton model and QCD, it is believed that, at large Q^2 , the nucleons must behave as systems of point-like quarks bound by gluon-exchanges and governed by the properties of the strong force. The first attempt at a quark-gluon description of the nucleon form factors was, as for the deuteron case, within the quark dimensional scaling framework [26, 27], which predicted that, at large Q^2 , F_1 and F_2 should scale as $(Q^2)^{-2}$ and $(Q^2)^{-3}$, and as a result, the ratio F_2/F_1 should scale as $1/Q^2$. This asymptotic behavior was confirmed within a pQCD consideration, where Brodsky and Lepage argued [70] that, at large Q^2 , QCD effects produce only a logarithmic departure from the QDS power laws, in agreement with the large Q^2 SLAC elastic electron-proton cross section E-136 data [71].

Further work [72] showed that use of naive symmetric quark distribution amplitudes in the pQCD approach, where the three valence quarks share equally the nucleon’s momentum, failed dramatically to account for the sign and normalization of the proton magnetic form factor, favoring amplitudes in which the momentum balance of the valence quarks in the proton is quite asymmetric. These asymmetric distribution amplitudes are achieved at the expense of strong contributions from “soft” regions where one of the quark constituents carry a small fraction of the nucleon’s momentum. An attempt to calculate the contribution to the nucleon form factors from soft non-perturbative processes was provided by Nesterenko and Radyushkin [73]. They fixed the soft nucleon wave functions by employing QCD sum rules based on quark-hadron duality and decomposed the scattering process in a series of diagrams with gluon exchanges between the quarks. Their calculation showed that the form factors are dominated by “soft” processes over the Q^2 range of the existing data and they estimated that the scale of the transition to the hard two-gluon exchange between the three quarks is beyond the reach of present experiments.

Recent work by Miller [74] has showed that introduction of an orbital angular momentum component in the nucleon wave function, which violates hadron helicity conservation, alters the original pQCD prediction for the ratio F_2/F_1 . His model predicts that the ratio should scale as $1/Q$, in agreement with the recent JLab experiments that measured the ratio of G_E^p/G_M^p [75, 76] at moderate momentum transfers. It should be noted that Iachello and Wan [77] have argued that this $1/Q$ behavior is accidental and valid only at moderate momentum transfers. A re-examination of the above ratio within pQCD by Belitsky *et al.* [78] modifies the original pQCD prediction as $F_2/F_1 \sim [\ln(Q^2/\Lambda^2)]^2/Q^2$, where Λ is a soft scale related to the size of the nucleon. Although this derivation is also in agreement with the recent JLab data, the authors have pointed out that this could be precocious, as pQCD is expected to work at much higher momentum transfers, as Isgur and Llewellyn-Smith [45] have also argued in the past.

Over the years, there is a considerable number of calculations of the nucleon form factors applying various forms of relativistic constituent quark models (CQM), where the nucleon appears as the ground state of a quantum-mechanical three-quark system in a confining potential (a comprehensive review is given by Thomas and Weise [79]). These relativistic

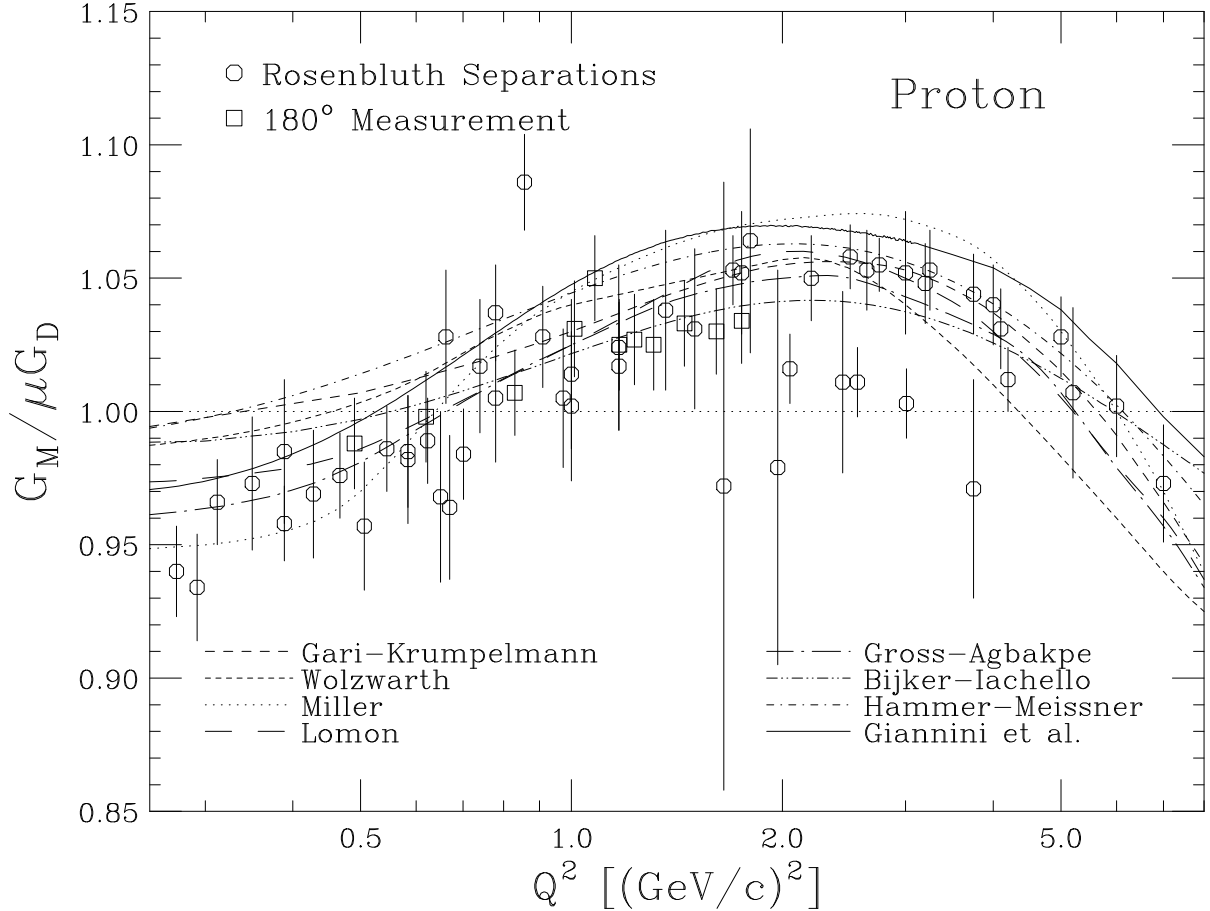


Figure 26: The proton magnetic form factor divided by the proton magnetic moment μ and the dipole formula $G_D = (1 + Q^2/0.71)^{-2}$. The data are from single JLab [91, 92], and SLAC, Bonn, DESY and Stanford Rosenbuth separation experiments as compiled, with radiative correction improvements, in Ref. [93], and SLAC $\Theta = 180^\circ$ data [7, 35]. The curves are theoretical calculations, described in the text.

nucleon descriptions use the Hamiltonian dynamics formalism of instant form, point form or light-front form to approximate the current operator assuming that the electron interacts with a single quark in the nucleon. Two early examples of light-front dynamics models are by Chung and Coester [80] and Schlumpf [81] who used symmetric nucleon wave functions with two parameters, an effective quark mass m and a confinement scale a . Among recent models that describe fairly well the existing form factor data are the ones by Miller [82], Giannini *et al.* [83], Holzwarth [84], Ma *et al.* [85], and Gross and Agbakpe [86].

Miller [82] used an extension of the cloudy bag model, where the three quarks are surrounded by a pion cloud, with the spatial wave function of Schlumpf, and with parameters chosen to reproduce the neutron radius and magnetic moments of the nucleons. Giannini *et al.* [83] introduced a three-quark interaction in the form of a gluon-gluon interaction in a hypercentral model, which describes well various static hadron properties. Holzwarth [84] used a chiral soliton model, where the quarks are bound in the nucleon by their interaction with chiral fields, including in addition to pion, the ρ and ω vector mesons. The Q^2 region of validity of the soliton form factors was extended by a proper boost from the nucleon rest frame to the Breit frame. Ma *et al.* [85] calculated the nucleon form factors within a simple quark spectator-diquark model, formulated in the light-cone formalism, with its parameters fixed by the static nucleon properties. Gross and Agbakpe [86] showed that the nucleon form factors can be explained using a covariant spectator model, where the nucleon is modeled as a spherical state of three constituent quarks with their own electromagnetic form factors and a possible pion cloud. An exhaustive listing of theoretical calculations of the nucleon form factors is given in the reviews by Gao [87], Hyde-Wright and de Jager [88], Arrington *et al.* [89] and Perdrisat *et al.* [90].

A comparison of the available proton magnetic form factor data for $Q^2 > 0.2$ (GeV/c)² with some of the above mentioned theoretical calculations is given in Figure 26. The G_M^p data are from JLab [91, 92], and SLAC, DESY, Bonn and Stanford Rosenbluth separations (from the same experiment), as compiled, with radiative correction improvements, in Ref. [93], and SLAC $\Theta = 180^\circ$ data [7, 35]. It is evident from the Figure that the differences, in general, among the theoretical calculations are small, implying that to discriminate successfully among the different models, precise experimental data over the widest momentum transfer range are necessary.

In the past several years there has been a considerably renewed interest in precision measurements of elastic scattering from the proton after the two JLab experiments [75, 76] that measured the G_E^p/G_M^p ratio found it to be in strong disagreement with previous measurements [94]. The previous measurements were based on the traditional Rosenbluth separation of elastic cross sections measured at different angles, meanwhile the JLab measurements were based on the polarization transfer technique, which used a polarized electron beam, and a

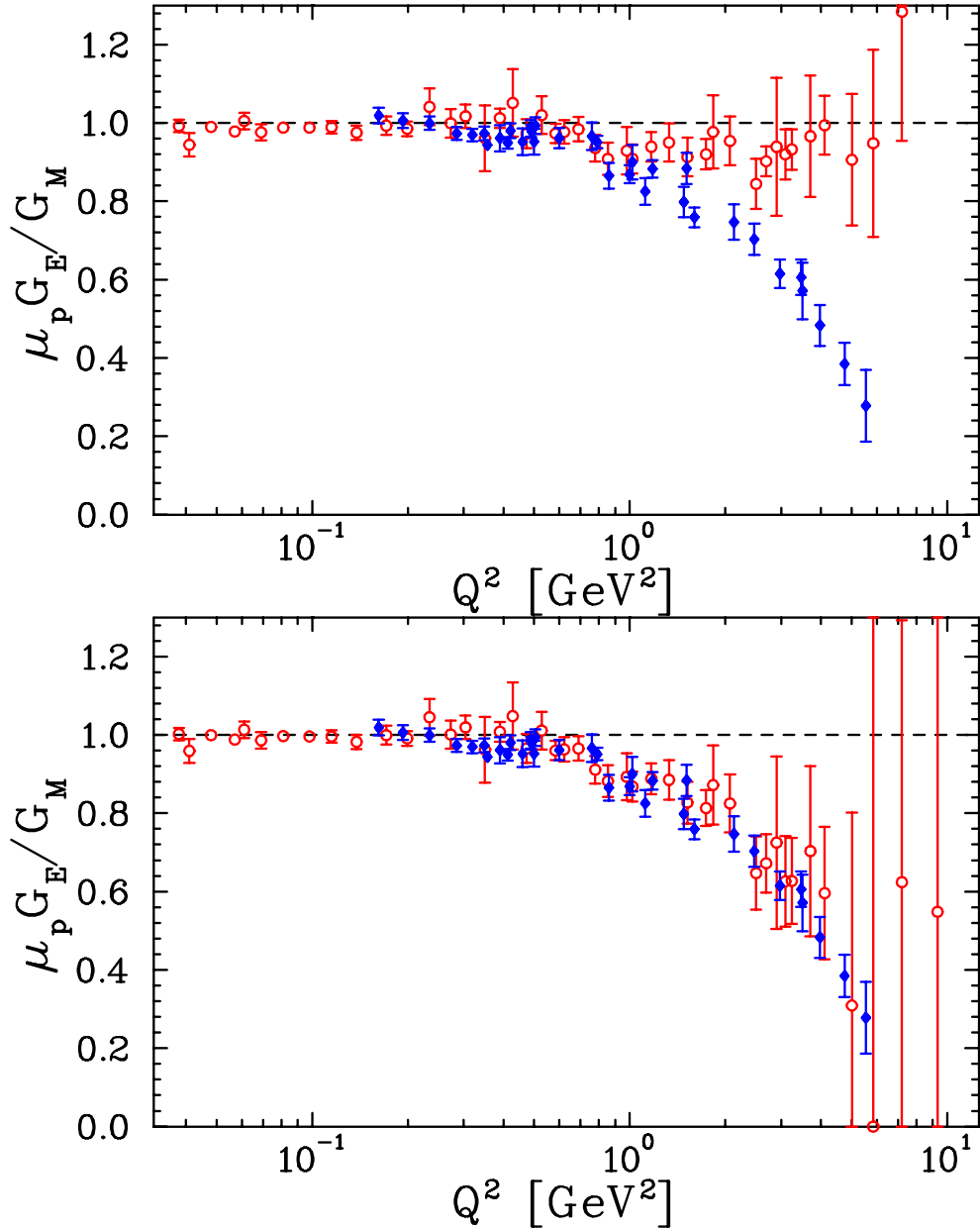


Figure 27: Experimental measurements of the proton form factor G_E^p/G_M^p ratio multiplied by the proton magnetic moment μ , as plotted in Ref. [97]. The solid diamonds are from recoil proton polarization transfer measurements. The open circles are from Rosenbluth separations without (top plot) and with (bottom plot) corrections for two-photon radiation effects applied to the measured cross sections.

vector polarimeter to measure the polarization of the recoil protons. An explanation of the disagreement could be attributed to the inherent, well known experimental deficiencies of the Rosenbluth separation method, arising from possible systematic errors in the wide range of incident beam energies, and scattered electron energies and angles used. In particular, the variation of the kinematical parameters of the scattered electrons necessitate measurements with magnetic spectrometers operating at their minimum and maximum fields (where their optical properties may be quite different) and in complete correlation with their target viewing angle. The polarization transfer technique is sensitive only to small uncertainties associated with the recoil polarimetry. Another possible explanation for the disagreement could be two-photon exchange processes not accounted for in the standard corrections for radiative effects and which could affect far more the elastic cross section than the recoil proton polarization [95, 96]. This explanation has gained credibility after new precise JLab data [91, 92] using the Rosenbluth technique were found to agree with the previous SLAC data [94], and with recent theoretical work that seems to reconcile the Rosenbluth separation and polarization technique data [97] (see Figure 27). The end result of the above disagreement is that, presently, there is some uncertainty in the determination of both proton form factors.

2.2 The Proton Proposed Measurements

The proposed experimental setup can provide unique proton G_M^p data over a wide range of momentum transfers, from $Q^2 = 0.4$ to 4.3 $(\text{GeV}/c)^2$, in a very timely fashion. The cross sections that can be measured at very backward angles (153° - 170°) will be proportional to $(G_M^p)^2$ (the contribution from $(G_E^p)^2$ will be at most 0.5%), and therefore free of the experimental deficiencies that plague Rosenbluth separations. The statistical error on the cross section of these measurements will be negligible ($\leq 0.1\%$). The G_M^p measurements will span over a wide kinematical range covered in the past by several measurements with different systematic errors (8 experiments). The systematic error on the cross section in this experiment will be comparable to other similar JLab and SLAC precision experiments, about $\pm 2.5\%$, resulting in a $\pm 1.25\%$ error for G_M^p .

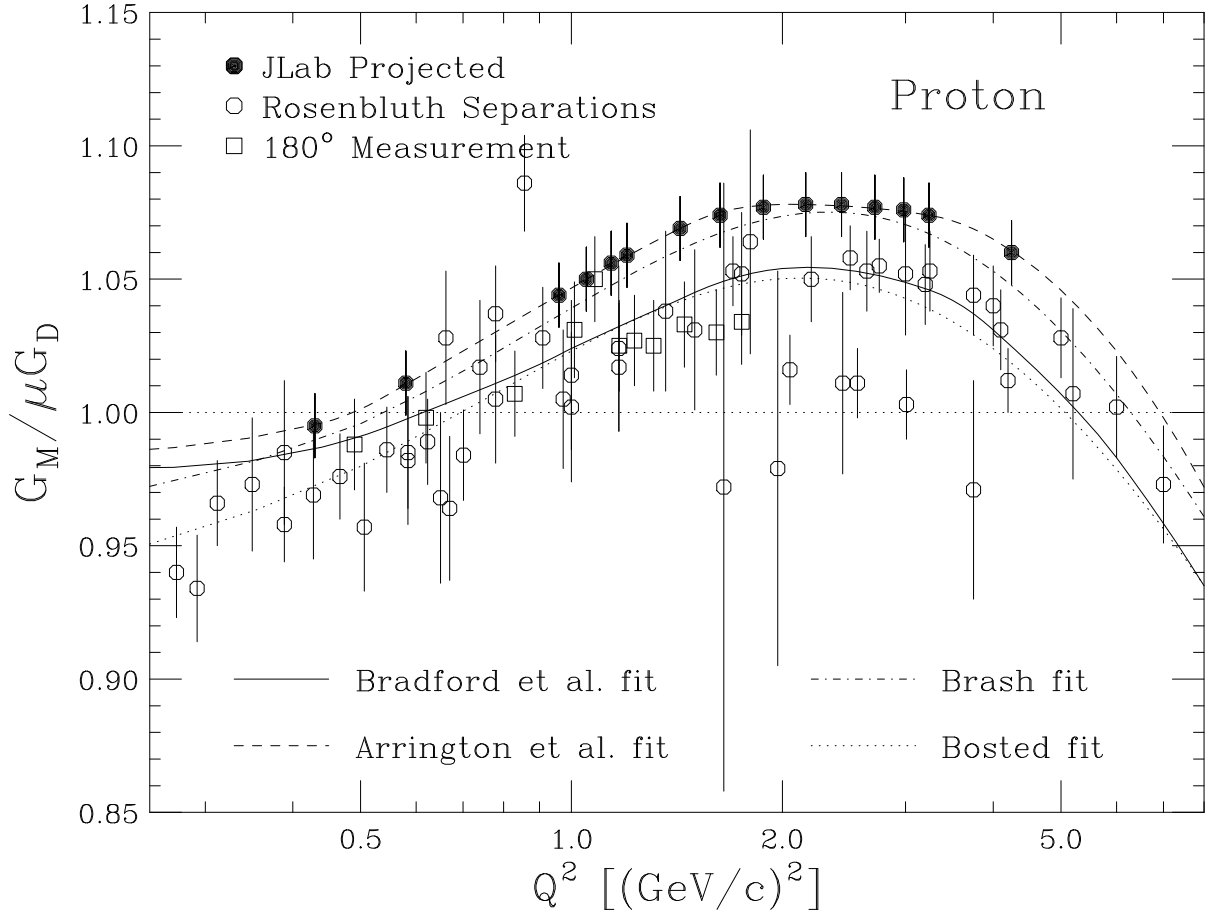


Figure 28: The proton magnetic form factor divided by the proton magnetic moment μ and the dipole formula $G_D = (1 + Q^2/0.71)^{-2}$. The open circles are Rosenbluth separation data from individual extractions using only measurements from single JLab [91, 92], and SLAC, Bonn, DESY and Stanford experiments, as compiled in Ref. [93]. The squares are the direct $\Theta = 180^\circ$ SLAC NE4 data [7, 35]. The curves are fits by Brash *et al.* [93], Bosted [98], Bradford *et al.* [100] and Arrington *et al.* [97] (see text). The solid circles are the projected data from the proposed experiment, arbitrarily set, for clarity, to follow the fit of Arrington *et al.*

We propose to measure elastic electron-proton scattering for every beam energy of the deuteron (and for two of the ^3He , see below) elastic settings. The measurements will span the Q^2 range from 0.4 to 4.3 $(\text{GeV}/c)^2$. The kinematics and all relevant parameters of the run plan for these proton measurements are given in Tables 3 and 4. The beam energy range is 0.46 to 2.7 GeV, the scattered electron energy E' is in the range of 0.23 to 0.42 GeV, and

the recoil deuteron momentum P_r will be in the range of 0.69 to 3.1 GeV/ c . The electron scattering angle Θ will be in the range 170° to 153° .

The projected G_M^p data from these measurements are shown in Figure 28 along with the existing JLab, SLAC, DESY, Bonn and Stanford Rosenbluth separation data and the direct $\Theta = 180^\circ$ elastic proton data from SLAC experiment NE4. Shown also in the Figure is i) a fit by Bosted [98] of the G_M^p values from the “global” analysis of all elastic cross section data by Walker *et al.* [99], ii) a fit by Brash *et al.* [93] on G_M^p values extracted from selected elastic cross section data and the new JLab Hall A data on the G_E^p/G_M^p ratio, iii) a fit by Bradford *et al.* [100] which emphasized measurements based on the polarization transfer technique and excluded Rosenbluth measurements of G_E^p above 1 (GeV/ c)², and iv) a fit by Arrington *et al.* [97], where all the data used have been corrected for two-photon radiation effects. The difference between the curves is indicative of the present G_M^p uncertainty arising from the disagreement of the Rosenbluth and polarization transfer techniques and the very possible two-photon contributions. The required beam time for these proton measurements is 1 day, assuming a 5 cm long hydrogen target of density 0.071 g/cm³, and beam currents of up to 60 μ A.

It is evident from Figure 28 that the proposed measurements will provide precise data over a very wide momentum transfer range. They are expected to provide valuable input in understanding the extraction of the proton form factors from polarized and unpolarized measurements and in establishing firm values for the magnetic form factor. The data will be used to test a whole variety of theoretical calculations of the nucleon structure based on recently refined Vector Meson Dominance models, various forms of relativistic constituent quark models including cloudy bag and chiral soliton models, recently revisited perturbative and non-perturbative QCD models, and expected accurate lattice QCD calculations.

3 Precision Measurement of the ³He Magnetic Form Factor

3.1 Short Review of the ³He Form Factors

The proposed experimental setup will be also ideal to measure precisely the magnetic form factor, F_M , of ³He around its 1st diffraction minimum. The location of the minimum is very

poorly defined, as previous backward Saclay [101, 102] and MIT/Bates [103] cross section measurements, even at fairly large angles, were dominated by contributions from the charge form factor, F_C . The Saclay measurements were at 155° and the MIT/Bates ones at 160° . The setup of this proposal will allow elastic measurements at $\sim 172^\circ$, which will enhance the F_M contribution to the cross section by one order of magnitude as compared to the MIT/Bates and Saclay measurements.

The cross section for elastic electron scattering from the spin one-half ${}^3\text{He}$ nucleus is given, in the one-photon exchange approximation, by:

$$\frac{d\sigma}{d\Omega}(E, \Theta) = \frac{(Z\alpha)^2 E'}{4E^3 \sin^4\left(\frac{\Theta}{2}\right)} \left[A(Q^2) \cos^2\left(\frac{\Theta}{2}\right) + B(Q^2) \sin^2\left(\frac{\Theta}{2}\right) \right], \quad (27)$$

where Z is the nuclear charge, and $A(Q^2)$ and $B(Q^2)$ are the ${}^3\text{He}$ elastic structure functions, given in terms of the charge and magnetic form factors as:

$$A(Q^2) = \frac{F_C^2(Q^2) + (1 + \kappa)^2 \tau F_M^2(Q^2)}{1 + \tau}, \quad (28)$$

$$B(Q^2) = 2\tau(1 + \kappa)^2 F_M^2(Q^2), \quad (29)$$

where κ is the anomalous magnetic moment of the nucleus. The two form factors of ${}^3\text{He}$ are also determined by measuring the elastic cross section at several angles using variable beam energies for the same fixed Q^2 (Rosenbluth separation).

The electromagnetic form factors of the few-body nuclear systems (${}^3\text{He}$, ${}^3\text{H}$ and ${}^4\text{He}$) [104] provide fundamental information on their internal structure and dynamics. They are very sensitive to the choice of the nucleon-nucleon interaction potential, the treatment of meson-exchange currents and relativistic corrections, and to a possible admixture of multi-quark states. They have been the subject of extensive experimental investigations over the past 40 years [4]. At large four-momentum transfers they may offer a unique opportunity to uncover a possible transition in the description of elastic electron scattering off the few-nucleon systems, from meson-nucleon to quark-gluon degrees of freedom as predicted by quark dimensional scaling [44].

Theoretically, in the non-relativistic impulse approximation approach, the few-body form factors are calculated using numerical solutions of the Faddeev equations, the correlated hyperspherical harmonics (CHH) variational method, or Monte Carlo methods to solve for the

nuclear ground states [1]. All three methods provide a solution of the Schrödinger equation for non-relativistic nucleons bound by the nucleon-nucleon interaction. The Faddeev decomposition for the three- or four-body problem rewrites the Schrödinger equation as a sum of three or four equations, in which only one pair of nucleons interacts at a time. The resulting equations are solved in either momentum or coordinate space. The CHH variational method [48] is based on a decomposition quite similar to the Faddeev one. The primary differences are the introduction of hyperspherical coordinates and inclusion of the strong state-dependent correlations, induced by the nucleon-nucleon interaction, directly in the definition of the nuclear wave function. The principal Monte Carlo schemes developed are variational and Green’s function Monte Carlo. Variational Monte Carlo (VMC) [105, 106, 107, 108] uses Monte Carlo techniques to perform standard numerical quadratures. Green’s function Monte Carlo (GFMC) [107, 109] employs Monte Carlo methods to evaluate the imaginary-time path integrals relevant for a light nucleus. All modern calculations augment their impulse approximation by meson-exchange currents [110]. Satisfactory description of the available ${}^3\text{He}$, ${}^3\text{H}$, and ${}^4\text{He}$ form factor data is not possible without inclusion of MEC. Better agreement with the data is obtained by inclusion of contributions from multi-quark clusters within the framework of hybrid quark models, but, as for the deuteron case, these models are still in phenomenological stage [111, 112, 113, 114]. The question whether introduction of possible isobar configurations and of “three-body force” effects by three-body interactions is necessary for a complete theoretical description of the few-body form factors is still unanswered. Studies [48, 115] have shown that isobar configurations do not produce large contributions.

Figures 29 and 30 show all the experimental data for the ${}^3\text{He}$ charge and magnetic form factors in the Q^2 range from 0 to 40 fm^{-2} from Stanford [116, 117], Orsay [118], Saclay [101, 102], Bates [103, 119, 120], Mainz [121] and SLAC [122] experiments. The data demonstrate the presence of an expected diffraction minimum for both form factors. They are compared to four “full” older calculations by Hadjimichael and collaborators [123], Struerve and collaborators [124], Schiavilla and collaborators [105, 106] and Wiringa [107], and a newer calculation by Marcucci and collaborators [48]. All calculations include, in addition to the impulse approximation, meson-exchange currents and genuine three-body force effects. [The theoretical impulse approximation alone, not shown in the Figures, totally

fails to describe the data. It grossly overestimates (underestimates) the location of the diffraction minimum and underestimates (overestimates) the secondary maximum of F_C (F_M), necessitating the need for inclusion of meson-exchange currents.] The above full calculations describe fairly well the charge form factor data, but fail to reproduce the position of the magnetic form factor minimum. Some authors [125] have attributed this disagreement to the need for fully relativistic calculations [126, 127] for the three-body form factors. Gross and collaborators have initiated a serious effort to calculate the three-body form factors in a consistent relativistic framework. Their initial work [127] has been followed by a recent paper [128] where they derived a complete Feynman diagram expansion for the elastic form factor of the three-body bound state using the covariant spectator theory [18]. Similar work is in progress by Adam and Van Orden [129].

Hadjimichael and collaborators [123] calculated the ^3He form factors solving the coupled-channel Faddeev equations in coordinate space, with several N-N potential models, and in particular with the Paris and Reid Soft Core potentials. The calculation included π , ρ , ω , $\rho\pi\gamma$ and $\omega\pi\gamma$ MEC plus isobar admixtures in the initial ground state wave function. Also included are the one-body Darwin-Foldy (DF) and spin-orbit (SO) relativistic corrections to the charge operator. Three-body force effects have been accounted by including in the calculation the two-pion exchange three-body interaction, via Δ -isobar excitation.

Struerve and collaborators [124] calculated the ^3He form factors solving the Faddeev equations in momentum space, and using the Paris N-N potential modified to include Δ -isobar excitations via π and ρ meson-exchanges. The presence of the Δ thus accounted for the most important part of three-body force effects. The calculation included π , ρ , and $\rho\pi\gamma$ meson-exchange contributions, as well as the DF and SO relativistic corrections to the charge operator.

Schiavilla and collaborators [105, 106] calculated the ^3He form factors using VMC wave functions computed with the Argonne v_{14} two-nucleon and the Urbana-VII three-nucleon interactions. The leading isovector MEC, the “ π -like” and “ ρ -like”, have been derived consistently with the nucleon-nucleon interaction used. The calculation included, in addition to the DF and SO relativistic corrections, contributions from ω and $\omega\pi\gamma$ meson-exchange charge operators.

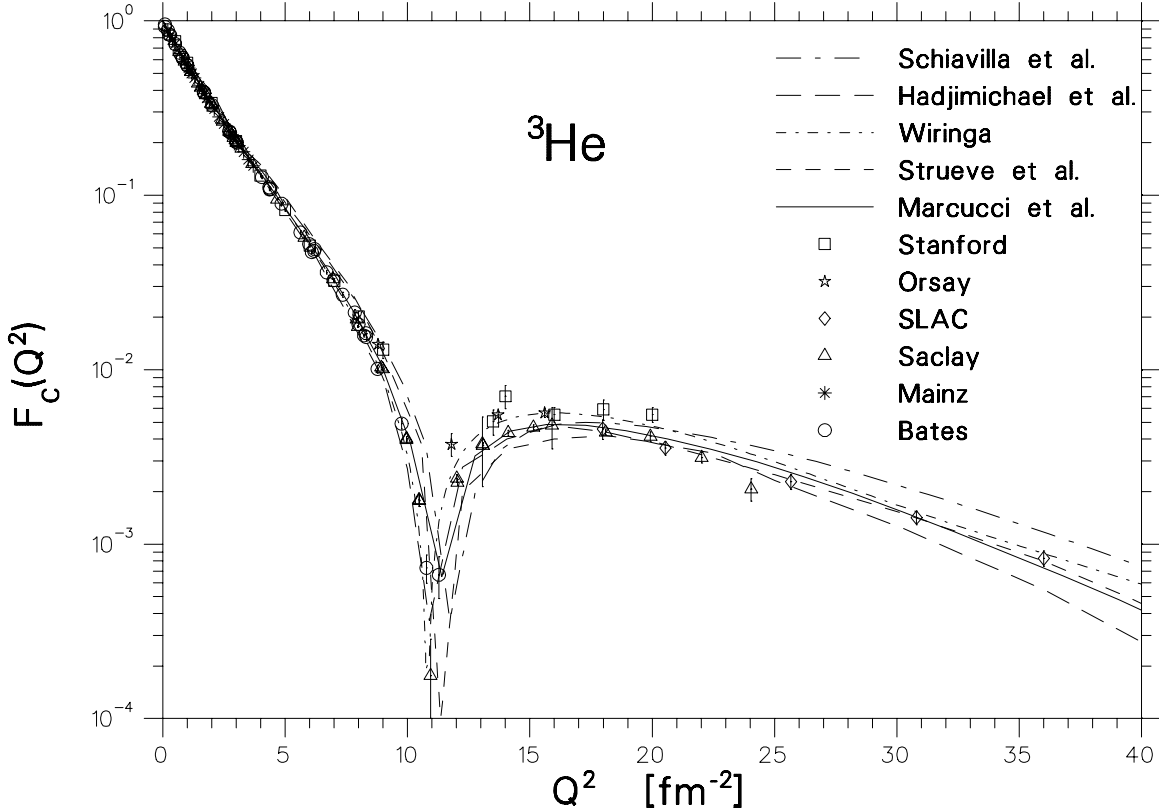


Figure 29: ${}^3\text{He}$ charge form factor data from Stanford [116, 117], Orsay [118], SLAC [122], Saclay [102], Mainz [121] and Bates [120] experiments, and theoretical IA+MEC calculations by Schiavilla *et al.* [106], Hadjimichael *et al.* [123], Strueve *et al.* [124], Wiringa [107] and Marcucci *et al.* [48] (see text).

Wiringa’s calculations [107] for the ${}^3\text{He}$ form factors were based on the same MEC model used by Schiavilla *et al.*, and on the Argonne v_{14} potential. The ${}^3\text{He}$ wave functions were determined with the Faddeev equations and three-body force effects were accounted with the Urbana-VIII three-nucleon force model.

The most recent calculation by Marcucci and collaborators [48] used the CHH variational method to construct high-precision wave functions obtained with the Argonne v_{18} two-nucleon [130] and Urbana-IX three-nucleon interactions model [131]. In this calculation, the two-body MEC operators have been constructed by the same method of the earlier calculation by Schiavilla *et al.* [105, 106] and significant new advances have been made in the

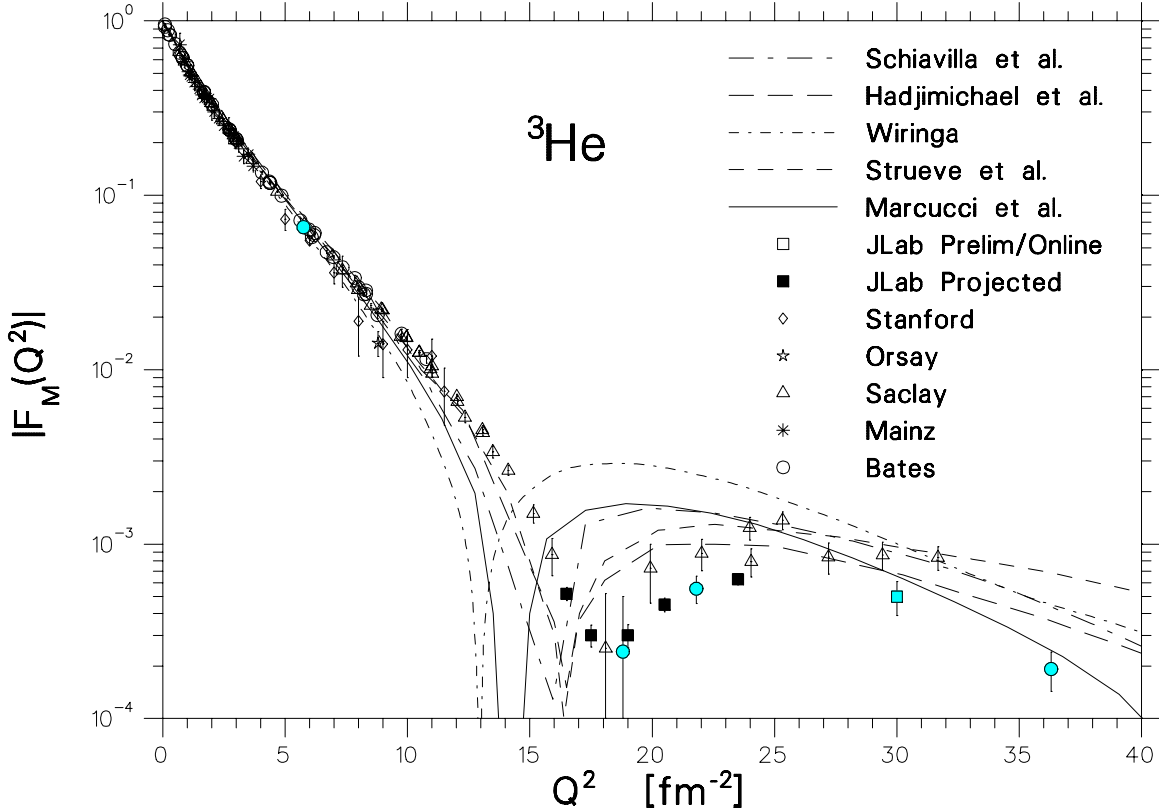


Figure 30: ${}^3\text{He}$ magnetic form factor data from Stanford [116, 117], Saclay [101],[102], Mainz [121], Orsay [118] and Bates [119, 103] experiments, and theoretical IA+MEC calculations by Schiavilla *et al.* [105], Hadjimichael *et al.* [123], Strueve *et al.* [124], Wiringa [107] and Marcucci *et al.* [48] (see text). The datum at $Q^2 = 30 \text{ fm}^{-2}$ is the online analysis result from the recently completed E04-18 Hall A experiment [59], under analysis. The solid squares are the projected data from this experiment.

construction of the irreducible three-nucleon exchange current operator and in the systematic treatment of Δ -isobar configurations in the nuclear bound states.

3.2 The ${}^3\text{He}$ Proposed Measurements

It should be noted that the Hall A Collaboration completed recently JLab experiment E04-18 [59] which measured the ${}^3\text{He}$ and ${}^4\text{He}$ form factors at large momentum transfers. The experiment was carried out in the fall of 2006 and spring and summer of 2007 in JLab's

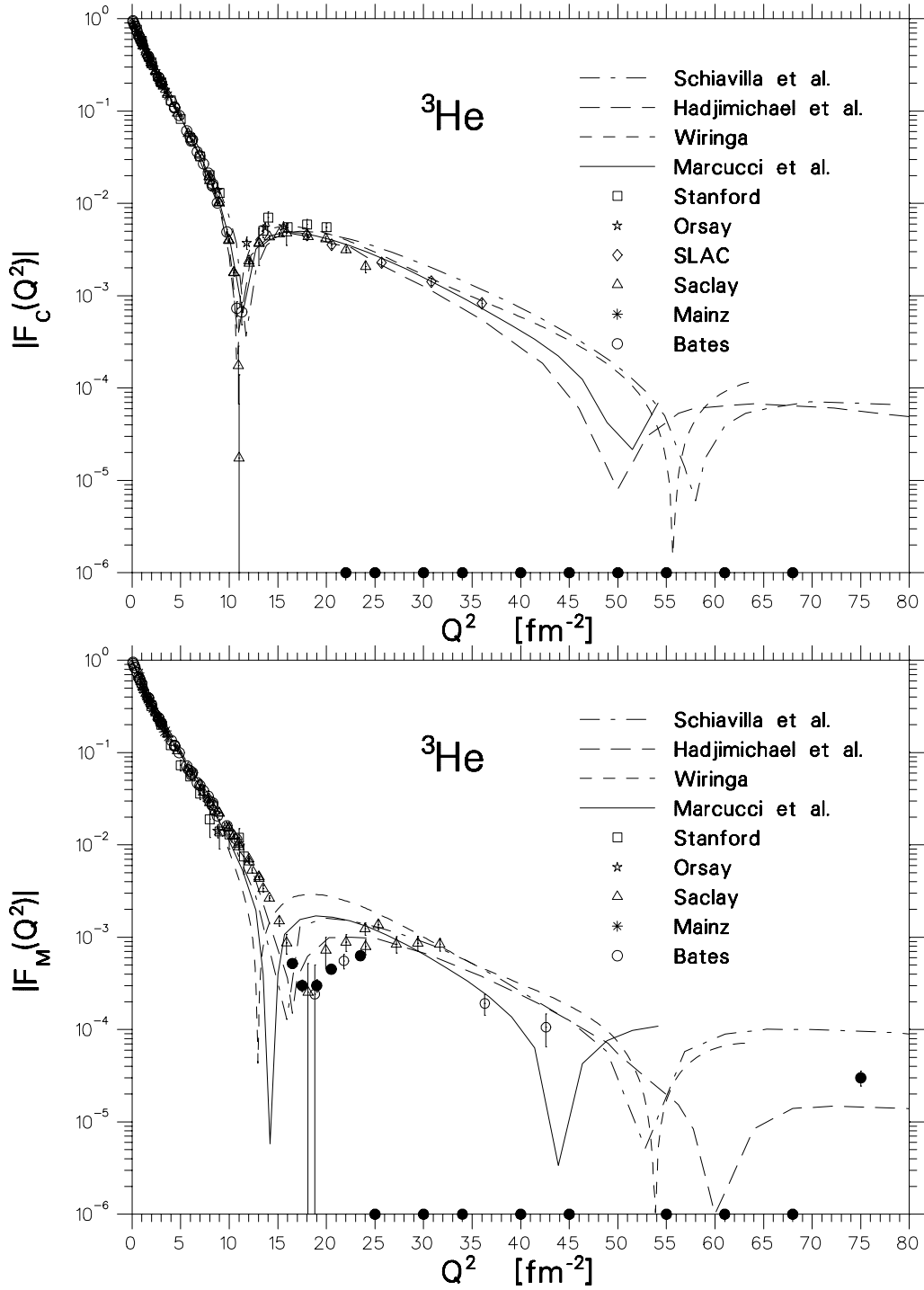


Figure 31: The world ${}^3\text{He}$ F_C and F_M data compared to four different calculations based on the IA with inclusion of MEC (see caption of Figures 29 and 30). The solid circles in the F_M bottom plot are the projected data from this experiment. The solid circles on the Q^2 axes indicate the Q^2 values of the recently completed E04-18 JLab experiment [59], under analysis.

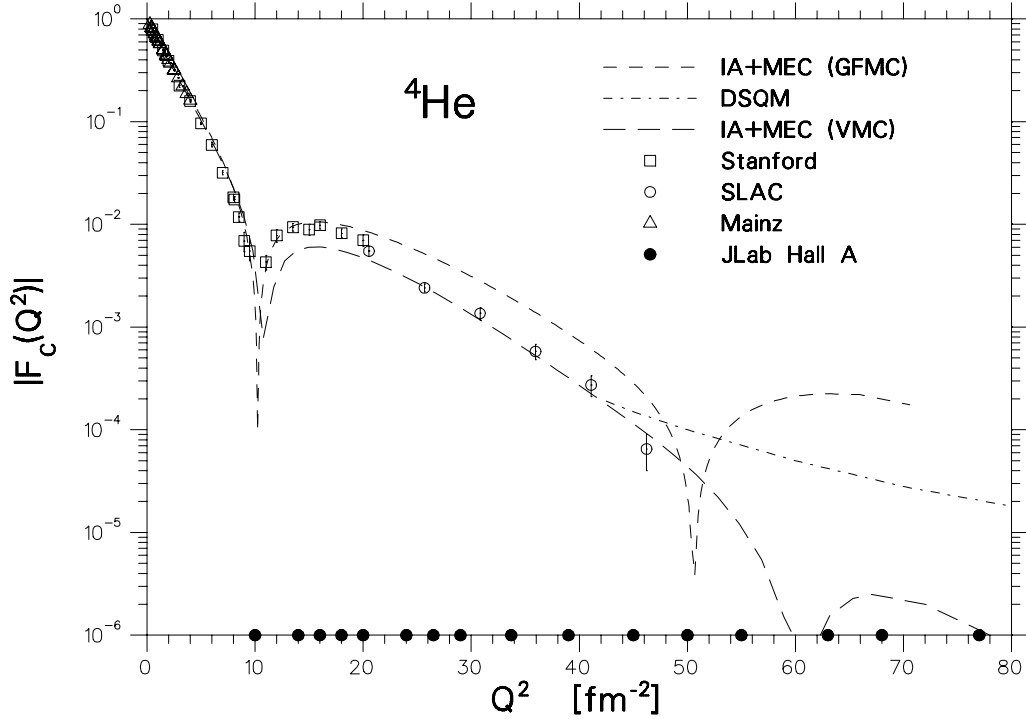


Figure 32: The world ${}^4\text{He}$ F_C data [117, 121, 122, 132] compared to two IA calculations with inclusion of MEC using Green’s Function Monte Carlo (GFMC) and Variational Monte Carlo (VMC) techniques [106, 107]. Shown is also the asymptotic prediction of the quark dimensional scaling model (DSQM) [44]. The solid circles indicate the Q^2 values of the recently completed E04-18 JLab experiment [59], under analysis.

Hall A Facility using the two HRS systems to detect scattered electrons and recoiling nuclei in coincidence. Elastic electron scattering off ${}^3\text{He}$ was measured at forward and backward (140°) electron scattering angles to extract its F_C and F_M form factors using the Rosenbluth separation method. For ${}^4\text{He}$, only forward elastic electron scattering was measured to extract directly its F_C form factor. Data have been obtained in the Q^2 range from 22 to 68 fm^{-2} for ${}^3\text{He}$, and from 10 to 77 fm^{-2} for ${}^4\text{He}$, as indicated by the solid black circles in Figures 31 and 32. Online results for elastic electron-proton scattering are in good agreement with previous world measurements. A selected online analysis of helium elastic data has shown that they are consistent with previous measurements from other laboratories such as

SLAC and MIT/Bates. Of particular note is that the preliminary/online result for the ^3He F_M measurement at $Q^2 = 30 \text{ fm}^{-2}$ seems to agree with the trend of the MIT/Bates data, reinforcing an apparent disagreement between the Saclay and MIT/Bates data. The data analysis is in progress and preliminary results are expected within a year.

The proposed experiment will have the unique opportunity to precisely measure the ^3He magnetic form factor around its 1st diffraction minimum, and at $Q^2 = 75 \text{ fm}^{-2}$. This latter measurement will be very valuable in defining the large- Q^2 behavior of the magnetic form factor. The proposed kinematic settings and the run plan for these measurements are given in Tables 5 and 6, for a recoil nucleus angle of 3.5° . The electron scattering angle will vary between 172° and 170° , and its energy between 0.35 and 0.42 GeV. The recoil nucleus momentum P_r will be in the range of 0.81 to 1.79 GeV/ c . The required beam energies are in the range of 0.46 to 1.16 GeV. The estimated beam time for these helium measurements is 5 days at a beam current of 120 μA with a 5 cm long gas target of density 0.065 g/cm^3 for the five low- Q^2 kinematic points, and a 15 cm one for the high- Q^2 point.

The projected data from this measurement are shown in Figures 30 and 31. It can be seen that this measurement will provide data sufficient to accurately map the 1st diffraction minimum of the ^3He magnetic form factor and provide an additional unique large- Q^2 F_M measurement. The results will be of utmost importance in testing our knowledge of the nucleon-nucleon interaction, possible three-body force effects and the nature of meson-exchange currents, and in constraining the parameters of the theoretical few-body standard model.

4 Summary–Request

We propose to perform a precision measurement of the deuteron magnetic form factor, a fundamental nuclear physics observable, over its diffraction minimum and up to the largest possible Q^2 limited by cross section sensitivity of one elastic event per day. The experiment can be performed in the Hall A Facility of JLab using a dual 3.5° recoil magnetic spectrometer using the two HRS systems and a dual-septum magnet, and a dual backward electron spectrometer ($\sim 170^\circ$) based on two small dipole magnets. The results from this

measurement are expected to lead to the establishment of a consistent canonical hadronic model describing the electromagnetic structure of the deuteron.

Additional possible measurements of the proton magnetic form factor over a wide momentum transfer range will provide a unique, precise set of data, free of Rosenbluth separation experimental deficiencies, and highly complementary to previous JLab data sets on the electric form factor, to test the theoretical models on the quark substructure of the nucleon. Finally, the proposed measurement of the ^3He magnetic form factor, around its 1st first diffraction and at large Q^2 , will provide precise data on another fundamental nuclear physics observable to constrain the parameters of the standard theoretical model describing the three-body nuclear systems.

We request the resources to design and build the dual-septum and the two small dipole magnets and a cryogenic deuterium/hydrogen/helium target assembly of 5, 10 and 15 cm tuna-can cells. The required beam time is 38 days (deuterium: 32, proton: 1, ^3He : 5) of data taking at 100% efficiency including empty target running and the necessary time for beam energy and target filling changes. An additional 3 days of low-current beam time is required for the check-out of the spectrometers and the detectors with a functional cryotarget.

5 Tables

ELECTRON-DEUTERON ELASTIC KINEMATICS

$$\Theta_r = 3.5^\circ$$

Q^2 [(GeV/c) ²]	E (GeV)	E' (GeV)	Θ deg.	P_r (GeV/c)	β_r	$d\Omega_e/d\Omega_r$
1.40	0.809	0.436	170.0	1.241	0.55	8.12
1.55	0.865	0.452	169.8	1.312	0.57	8.45
1.70	0.919	0.466	169.6	1.380	0.59	8.79
1.80	0.955	0.475	169.5	1.425	0.61	9.01
2.20	1.094	0.508	168.9	1.595	0.65	9.90
2.55	1.211	0.532	168.5	1.736	0.68	10.7
3.00	1.358	0.558	168.0	1.908	0.71	11.7
3.50	1.517	0.584	167.4	2.091	0.74	12.8
4.00	1.672	0.606	166.8	2.266	0.77	14.0
4.50	1.825	0.625	166.2	2.437	0.79	15.2
5.00	1.976	0.643	165.6	2.603	0.81	16.4
5.50	2.124	0.658	165.1	2.766	0.83	17.7
6.00	2.272	0.672	164.6	2.926	0.84	19.0

Table 1: Elastic electron-deuteron kinematics in the Q^2 range from 1.4 to 6.0 (GeV/c)². The recoil deuteron angle, Θ_r , is fixed at 3.5°, E is the incident beam energy, E' is the scattered electron energy, P_r and β_r are the recoil deuteron momentum and speed. The last column is the Jacobian transformation of the solid angle for recoil detection.

DEUTERON $B(Q^2)$ RUN PLAN SCENARIO

$$\Theta_r = 3.5^\circ$$

Q^2 [(GeV/c) ²]	$A(Q^2)$	$B(Q^2)$	R %	Cross Section (cm ² /sr)	Time (hr)	Counts	$\Delta B(Q^2)$ (±%)
1.40	2.4×10^{-5}	5.0×10^{-7}	73	2.9×10^{-39}	24	830	6.4
1.55	1.5×10^{-5}	2.0×10^{-7}	62	1.2×10^{-39}	24	360	10
1.70	1.0×10^{-5}	6.0×10^{-8}	42	4.5×10^{-40}	24	150	21
1.80	7.5×10^{-6}	1.7×10^{-8}	21	2.3×10^{-40}	84	280	35
2.20	2.5×10^{-5}	1.1×10^{-8}	32	6.9×10^{-41}	96	115	31
2.55	1.0×10^{-6}	1.9×10^{-8}	65	4.6×10^{-41}	48	45	23
3.00	3.7×10^{-7}	2.6×10^{-8}	87	3.5×10^{-41}	34	30	22
3.50	1.2×10^{-7}	3.1×10^{-8}	95	2.9×10^{-41}	29	25	21
4.00	4.7×10^{-8}	2.7×10^{-8}	98	1.9×10^{-41}	38	25	21
4.50	1.9×10^{-8}	1.8×10^{-8}	98	9.9×10^{-42}	60	25	21
5.00	6.8×10^{-9}	9.2×10^{-9}	99	4.1×10^{-42}	72	14	27
5.50	2.0×10^{-9}	3.5×10^{-9}	99	1.3×10^{-42}	120	8	36
Sub-Total					653		
Total					769		

Table 2: Run plan scenario with cross section and counting rate estimates for the $B(Q^2)$ measurements. The quantity R is the fraction of elastic events from magnetic scattering [due to $B(Q^2)$]. The rate estimates assume a 10 cm long liquid deuterium target with density 0.162 g/cm³, a beam current of 120 μ A, a variable double-arm solid angle of 50 (20) msr at the highest (lowest) Q^2 kinematics, and a radiative correction factor of 0.8. The total time includes 20 hours of empty target running and 96 hours for energy changes.

ELECTRON-PROTON ELASTIC KINEMATICS

$$\Theta_r = 3.5^\circ$$

Q^2 [(GeV/c) ²]	E (GeV)	E' (GeV)	Θ deg.	P_r (GeV/c)	β_r	$d\Omega_e/d\Omega_r$
0.43	0.463	0.234	169.6	0.695	0.59	8.83
0.58	0.569	0.258	168.8	0.823	0.66	10.2
0.96	0.809	0.299	167.0	1.102	0.76	13.6
1.05	0.865	0.307	166.6	1.166	0.78	14.5
1.14	0.919	0.314	166.2	1.226	0.79	15.3
1.20	0.955	0.318	165.9	1.266	0.80	15.9
1.43	1.094	0.332	164.9	1.418	0.83	18.2
1.63	1.211	0.343	164.1	1.543	0.86	20.3
1.88	1.358	0.354	163.0	1.701	0.88	23.1
2.16	1.517	0.365	161.8	1.868	0.89	26.2
2.43	1.672	0.375	160.7	2.029	0.91	29.4
2.71	1.825	0.383	159.6	2.188	0.92	32.7
2.98	1.976	0.390	158.5	2.343	0.93	36.1
3.24	2.124	0.397	157.4	2.495	0.94	39.6
4.25	2.683	0.418	153.4	3.062	0.96	53.7

Table 3: Elastic electron-proton kinematics in the Q^2 range from 0.4 to 4.0 (GeV/c)². The recoil proton angle, Θ_r , is fixed at 3.5° , E is the incident beam energy, E' is the scattered electron energy, P_r and β_r are the recoil proton momentum and speed. The last column is the Jacobian transformation of the solid angle for recoil detection.

PROTON G_M^p RUN PLAN SCENARIO

$$\Theta_r = 3.5^\circ$$

Q^2 [(GeV/c) ²]	G_E^p	G_M^p	R %	Cross Section (cm ² /sr)	I (μ A)	Time (hr)	Counts $\times 10^6$	$(\Delta G_M^p)_{stat}$ (\pm %)
0.43	0.374	0.386	99.6	3.60×10^{-33}	5	1	16	0.02
0.58	0.290	0.305	99.7	1.18×10^{-33}	5	1	11	0.03
0.96	0.170	0.190	99.8	4.61×10^{-34}	10	1	10	0.03
1.05	0.152	0.171	99.8	3.45×10^{-34}	10	1	8.3	0.03
1.14	0.136	0.156	99.8	2.65×10^{-34}	10	1	7.1	0.04
1.20	0.127	0.147	99.8	2.23×10^{-34}	20	1	9.6	0.03
1.43	0.097	0.118	99.9	1.19×10^{-34}	20	1	6.2	0.04
1.63	0.079	0.099	99.9	7.31×10^{-35}	20	1	4.2	0.05
1.88	0.062	0.081	99.9	4.12×10^{-35}	20	1	2.7	0.06
2.16	0.048	0.066	99.9	2.34×10^{-35}	60	1	7.0	0.05
2.43	0.038	0.055	99.9	1.41×10^{-35}	60	1	4.7	0.05
2.71	0.031	0.047	99.9	8.83×10^{-36}	60	1	3.3	0.06
2.98	0.025	0.040	99.9	5.76×10^{-36}	60	1	2.4	0.06
3.24	0.021	0.035	99.9	3.89×10^{-36}	60	1	1.8	0.08
4.25	0.010	0.022	100	1.06×10^{-36}	60	1	0.7	0.12
Sub-Total						15		
Total						26		

Table 4: Run plan scenario for the proton G_M^p measurements. The rate estimates assume a 5 cm long hydrogen target with density 0.071 g/cm³, a variable double-arm solid angle of 50 (27) msr at the highest (lowest) Q^2 kinematics, and a radiative correction factor of 0.8. The ratio R is the percentage of the counting rate due to magnetic scattering (due to G_M^p). The expected systematic error on the cross section is $\pm 2.5\%$, resulting in a systematic error for G_M^p of $\pm 1.25\%$. The total time includes 3 hours of empty target running and 8 hours for an energy change.

ELECTRON-³He ELASTIC KINEMATICS

$$\Theta_r = 3.5^\circ$$

Q^2 [(GeV/c) ²]	E (GeV)	E' (GeV)	Θ deg.	P_r (GeV/c)	β_r	$d\Omega_e/d\Omega_r$
16.5	0.463	0.349	171.85	0.810	0.28	5.40
17.5	0.479	0.356	171.81	0.835	0.29	5.46
19.0	0.502	0.370	171.76	0.870	0.30	5.53
20.5	0.525	0.383	171.70	0.906	0.31	5.63
23.5	0.569	0.405	171.59	0.971	0.33	5.75
75.0	1.156	0.636	170.13	1.786	0.54	7.90

Table 5: Elastic electron-³He kinematics in the Q^2 range from 16.5 to 23.5 fm⁻² (around the 1st diffraction minimum of the F_M elastic form factor), and at $Q^2 = 75$ fm⁻². The recoil helium angle, Θ_r , is fixed at 3.5°, E is the incident beam energy, E' is the scattered electron energy, P_r and β_r are the recoil helium momentum and speed. The last column is the Jacobian transformation of the solid angle for recoil detection.

^3He F_M RUN PLAN

$$\Theta_r = 3.5^\circ$$

Q^2 [(GeV/c) ²]	F_C	F_M	R %	Cross Section (cm ² /sr)	Time (hr)	Counts	ΔF_M ($\pm\%$)
16.5	5.0×10^{-3}	5.2×10^{-4}	48	1.7×10^{-38}	4	158	8.9
17.5	4.5×10^{-3}	3.0×10^{-4}	28	9.6×10^{-39}	8	177	14
19.0	4.0×10^{-3}	3.0×10^{-4}	35	7.6×10^{-39}	5	96	15
20.5	4.0×10^{-3}	4.5×10^{-4}	56	1.0×10^{-38}	4	105	9.1
23.5	2.7×10^{-3}	6.3×10^{-4}	86	1.3×10^{-38}	2	66	7.4
75.0	1.0×10^{-5}	3.0×10^{-5}	100	1.5×10^{-41}	48	8	18
Sub-Total					71		
Total					125		

Table 6: Run plan scenario with cross section and counting rate estimates for the ^3He magnetic form factor measurements. The rate estimates assume a 5 (15) cm long gas helium target with density 0.065 g/cm³ for the five low- Q^2 points (high- Q^2 point), a beam current of 120 μA , a variable double-arm solid angle of 24 (16) msr at the highest (lowest) Q^2 kinematics, and a radiative correction factor of 0.8. The ratio R is the percentage of the counting rate due to magnetic scattering (due to F_M). The total time includes 4 hours of empty target running, 40 hours for energy changes, and 10 hrs for target filling changes.

6 APPENDIX: The Monte Carlo Simulation

6.1 The Coincidence Elastic Cross Section

In a single-arm elastic electron-nucleus experiment, where only the scattered electron is detected, the number N_e of elastically scattered electrons in the interval $\Delta E' = E'_{max} - E'_{min}$ around the elastic peak is:

$$N_e = N_b N_t C \frac{d\sigma}{d\Omega}(E_o, \Theta_o) R(\Delta E') L(\Delta E') \Delta\Omega, \quad (30)$$

where $d\sigma(E_o, \Theta_o)/d\Omega$ is the elastic cross section of interest for the central values of E_o and Θ_o , N_b is the number of incident beam electrons, N_t is the number of target nuclei per cm^2 , C contains all applicable corrections including the detector inefficiencies and dead-time effects, and $\Delta\Omega$ is the electron spectrometer solid angle. The factor $R(\Delta E') = \exp[\delta(\Delta E')]$ accounts for losses due to radiation effects (radiative correction factor) and it is calculable analytically when the spectrometer energy acceptance $\Delta E'$ is independent of the electron scattering angle Θ . The factor $L(\Delta E')$ (ionization factor) accounts for losses due to Landau ionization effects, which for high energies becomes approximately multiplicative and equal to $(1 - \xi/\Delta E')$, where the parameter ξ is characteristic of the target material (see below).

In a double-arm experiment, the number of electrons N_{er} in coincidence with recoil nuclei detected in a recoil spectrometer in the interval $\Delta P_r = (P_r)_{max} - (P_r)_{min}$ is:

$$N_{er} = N_b N_t C \frac{d\sigma}{d\Omega}(E_o, \Theta_o) R(\Delta E', \Delta P_r) L(\Delta E', \Delta P_r) \Delta\Omega_{er}, \quad (31)$$

where in this case the radiative correction factor and the ionization factor depend on both $\Delta E'$ and ΔP_r , the solid angle becomes the effective double-arm solid angle $\Delta\Omega_{er}$, and the correction factor C includes also losses due to absorption of recoil nuclei in the target and the detectors. The radiative correction factor is calculable only if one of the two spectrometers is the limiting aperture defining the double-arm solid angle, and if the recoil spectrometer momentum acceptance ΔP_r is independent of the recoil angle Θ_r . In practice, even if the latter condition is met, in a realistic experiment where counting rate limitations dictate use of the maximum solid angle available from a double-arm spectrometer system, the effective

double-arm solid angle is in many kinematics defined, as it is the case for this experiment, by both spectrometers. The resulting convolution of the solid angles of the two spectrometers, coupled by elastic kinematics and radiative and ionization effects makes impossible the calculation of the product $R(\Delta E', \Delta P_r)L(\Delta E', \Delta P_r)\Delta\Omega_{er}$ analytically. The product, in this case, has to be calculated by means of a Monte Carlo simulation.

To express the above convolution, one writes down the coincidence counting rate as:

$$N_{er} = N_b N_t C \left\langle \int \int \frac{d\sigma_{exp}}{d\Omega dE'}(E, E', \Theta, t) \Delta\Omega \Delta E' \right\rangle_{E,l}, \quad (32)$$

where $d\sigma_{exp}(E, E', \Theta, t)/d\Omega dE'$ is the differential experimental cross section, which depends also on the position, t , of the scattering vertex of the elastic event along the target length l . The experimental cross section is integrated over the effective angular and scattered electron energy acceptances of the double-arm spectrometer system for detection of scattered electrons in coincidence with recoil nuclei. The bracket enclosure indicates that the resulting integral is averaged over the energy distribution of the incident beam and over the target length.

6.2 Overview of the Simulation Method

The above averaged integral has to be calculated by simulating the entire elastic electron-nucleus scattering process, starting with the arrival of the beam electrons at the target, and ending with the arrival of the scattered electrons and of the recoil nuclei at the detectors of the electron and recoil spectrometer, respectively. The simulation requires complete knowledge of all physical processes happening in the target, in addition to the elastic scattering process in question, and transportation of scattered and recoil particles through reliable optical models of the spectrometers used for their detection. Among all processes present, the dominant one is radiation by the incoming and scattered electrons, which is inextricably intertwined with the scattering process.

Internal and External Bremsstrahlung

There are two kinds of radiation effects. The first one is from real and virtual photons emitted during the elastic scattering (referred to as internal bremsstrahlung and vertex

corrections respectively). The second one is from real photons emitted by electrons when passing through the target material before and after the scattering (referred to as external bremsstrahlung).

Following the seminal papers by Mo and Tsai [133, 134], and neglecting for the time being ionization energy loss effects, the cross section for electrons of incident energy E to scatter at an angle Θ to a final energy E' from a target of T radiation lengths including all radiation effects is given by:

$$\frac{d\sigma_{exp}}{d\Omega dE'} = \int_0^T \frac{dt}{T} \int_{\eta'E'}^E dE_1 \int_{E'}^{\eta_1 E_1} dE'_1 I_e(E, E_1, t) \frac{d\sigma}{d\Omega dE'}(E_1, E'_1, \Theta) I_e(E'_1, E', T-t), \quad (33)$$

where $I_e(E, E_1, t)$ is the probability of finding an electron starting at initial energy E and straggling down to energy E_1 after passing through t radiation lengths in the target, $I_e(E'_1, E', T-t)$ is the probability of finding an electron after the scattering at energy E'_1 and straggling down to energy E' through the rest of the target, and $d\sigma(E_1, E'_1, \Theta)/d\Omega dE'$ is the cross section for elastic scattering with incident energy E_1 to final energy E'_1 and at an angle Θ including internal radiation and vertex corrections. The lower limit of integration for E_1 is $\eta'E'$ and the upper limit of integration for E'_1 is $\eta_1 E_1$, where $\eta' = [1 - 2(E'/M) \sin^2(\Theta/2)]^{-1}$ and $\eta_1 = [1 + 2(E_1/M) \sin^2(\Theta/2)]^{-1}$. The difference $E - \eta'E'$ is the maximum energy of a photon which can be emitted along the direction of the incident electron. Similarly the maximum energy of a photon which can be emitted along the direction of the scattered electron is $\eta E - E'$, where $\eta = [1 + 2(E/M) \sin^2(\Theta/2)]^{-1}$.

It is customary, in addition to using the angle peaking approximation, to assume that the shape of the internal bremsstrahlung is the same as that of the external bremsstrahlung, and that the internal bremsstrahlung has approximately the same effect as that given by two “external equivalent radiators” with one placed before and one after the scattering, each of thickness:¹

$$t_{eq} = \frac{1}{b} \frac{\alpha}{\pi} \left[\ln \frac{Q^2}{m_e^2} - 1 \right], \quad (34)$$

¹For clarity of the formulation a factor b^{-1} has been included in the definition of the equivalent radiator.

where m_e is the electron mass, and the small terms proportional to Z and Z^2 from radiation by the target nucleus with atomic number Z are neglected. The quantity b is approximately equal to $4/3$ and depends only weakly on Z :

$$b = \frac{4}{3} \left\{ 1 + \frac{1}{9} \left[\frac{(Z+1)}{(Z+\zeta)} \right] \left[\ln(183Z^{-\frac{1}{3}}) \right]^{-1} \right\}, \quad (35)$$

where:

$$\zeta = \frac{\ln(1440Z^{-\frac{2}{3}})}{\ln(183Z^{-\frac{1}{3}})}. \quad (36)$$

The vertex corrections are included in the factor $F(Q^2, 0) = 1 + \delta'$, where:

$$F(Q^2, T) = 1 + 0.577bT + \frac{2\alpha}{\pi} \left[-\frac{14}{9} + \frac{13}{12} \ln \frac{Q^2}{m_e^2} \right] - \frac{\alpha}{2\pi} \ln^2 \left(\frac{E}{E'} \right) - \frac{\alpha}{\pi} \left[\frac{\pi^2}{6} - \Phi(\cos^2 \frac{\Theta}{2}) \right], \quad (37)$$

with $\Phi \left[\cos^2(\frac{\Theta}{2}) \right]$ being the Spence function. The first two terms of the right-hand side come from a Gamma function normalization factor $1/\Gamma(1+bT) \simeq 1+0.5772bT$. The third term is the sum of the vacuum polarization and the non-infrared part of the vertex correction. The fourth term can be regarded as a correction to the peaking approximation in the internal bremsstrahlung. The fifth term comes from the non-infrared divergent part of the soft photon emission cross section.

The probability of a small energy loss $E_i - E_f$ due to bremsstrahlung by an electron with incident energy $E_i > 100$ MeV in a target of t radiation lengths is given by:

$$I_e(E_i, E_f, t) = \frac{bt}{\Gamma(1+bt)} \left(\frac{E_i - E_f}{E_i} \right)^{bt} \frac{1}{E_i - E_f}. \quad (38)$$

Application of Equation 33 for an effective radiator of length $T_b = t_b + t_{eq}$, before the scattering, and an effective radiator of length $T_a = t_a + t_{eq}$, after the scattering, where t_b and t_a are the real radiator lengths before and after the scattering, and insertion of the vertex correction factor $(1 + \delta')$ results to:

$$\frac{d\sigma_{exp}}{d\Omega dE'} = \int_{\eta' E'}^E dE_1 I'_e(E, E_1, T_b) \frac{d\sigma}{d\Omega}(E_1, \Theta) (1 + \delta') I'_e(\eta_1 E_1, E', T_a), \quad (39)$$

where the function $I'_e(E_i, E_f, T_j)$ is given (for $j = a, b$) by:

$$I'_e(E_i, E_f, T_j) = \frac{bT_j}{\Gamma(1+bT_j)} \left(\frac{E_i - E_f}{E_i} \right)^{bT_j} \frac{1}{E_i - E_f}. \quad (40)$$

The calculation is straightforward but messy and uses the presence of a delta function for elastic scattering:

$$\frac{d\sigma}{d\Omega dE'}(E_1, E'_1, \Theta) = \frac{d\sigma}{d\Omega}(E_1, \Theta) \frac{E_1}{E'_1} \delta \left[E_1 - E'_1 - \frac{2E_1 E'_1}{M} \sin^2\left(\frac{\Theta}{2}\right) \right] \quad (41)$$

Setting $d\sigma(E_1, \Theta)/d\Omega = w(E_1, \Theta)d\sigma(E_o, \Theta_o)/d\Omega$, and using basic properties of the Gamma function, the experimental cross section becomes:

$$\frac{d\sigma_{exp}}{d\Omega dE'} = \frac{d\sigma}{d\Omega}(E_o, \Theta_o) F(Q^2, T) G(E, E', \Theta, t) \quad (42)$$

where $T = t_a + t_b$ and:

$$G(E, E', \Theta, t) = \int_{\eta' E'}^E dE_1 g(E, E', E_1, \Theta, t) \quad (43)$$

with:

$$g(E, E', E_1, \Theta, t) = \frac{bT_b}{E - E_1} \left(\frac{E - E_1}{E} \right)^{bT_b} w(E_1, \Theta) \frac{bT_a}{E_1 - E'} \left(\frac{\eta_1 E_1 - E'}{E'} \right)^{bT_a}, \quad (44)$$

where the factor $F(Q^2, T)$ is a very slow varying function of Q^2 and has been pulled out of the integral.

Direct substitution of Equation 42 into Equation 32 results in Equation 21 of the main text:

$$\frac{d\sigma}{d\Omega}(E_o, \Theta_o) = \frac{N_{er}}{N_b N_t C F(Q^2, T) P_{MC}}, \quad (45)$$

where:

$$P_{MC} = \left\langle \int \int G(E, E', \Theta, t) d\Omega dE' \right\rangle_{E,i}. \quad (46)$$

The above analysis indicates that the determination of the product of the double-arm solid angle and the radiative corrections is reduced to a simulation of the complex integral of Equation 43. Equation 44 suggests that the internal and external bremsstrahlung of an incident or scattered electron, with initial energy E_i , in a total (real and equivalent) radiator thickness T' , follows a probability distribution of the functional form:

$$\frac{bT'}{\Delta E_{if}} \left(\frac{\Delta E_{if}}{E_i} \right)^{bT'}, \quad (47)$$

where ΔE_{if} is the energy loss by the electron. The term $w(E_1, \Theta)$ dictates that a simulation of an electron-nucleus scattering event must be weighted by a probability distribution defined

by the elastic cross section. Since the elastic cross section is to be measured, one has to use a model for it, then determine P_{MC} and subsequently the elastic cross section, and after that iterate. The procedure converges very quickly.

The factor P_{MC} is essentially a number that can be determined from a Monte Carlo model that can simulate in the nuclear target material not only energy losses due to internal and external bremsstrahlung of the incident/scattered electrons, but also ionization energy losses and multiple scattering effects for the incident/scattered electrons and the recoil nuclei.

Ionization Energy Losses

The energy loss of charged particles due to ionization or excitation of the atoms of the material they traverse is subject to appreciable fluctuations about the most probable energy loss ΔE_{prob} . Ionization energy losses by the incident and scattered electrons, and by the recoil nuclei cannot be neglected in this experiment. The most probable energy loss is given by [135]:

$$\Delta E_{prob} = \frac{2\pi n e^4 z^2 t}{m_e c^2 \beta^2 \rho} \left[\ln \frac{4\pi n e^4 z^2 t}{I^2 (1 - \beta^2) \rho} - \beta^2 + 0.198 - \delta - U \right] \quad (48)$$

where n is the volume density of electrons in the material, ρ is the density of the material, I is the mean excitation potential of the material, z is the charge of the incident particle in units of the electron charge e , t is the path length of the particle in the material, and $\beta = v/c$, where v is the velocity of the particle. The term δ is the correction for the density effect, which is due to the polarization of the medium. The term U is due to the nonparticipation of the inner shells (K, L,...) for very low velocities of the incident particle.

The shape of the ionization energy loss distribution depends on the value of the parameter $K = \xi/q_{max}$ [136, 137], where:

$$\xi = \frac{2\pi z^2 e^4 n t}{m_e v^2} \quad (49)$$

and q_{max} is the maximum energy transfer in the collision from the incident particle to the atomic electrons, approximately given by $2m_e v^2/(1 - \beta^2)$ for incident heavy particles and by $T_e/2$ for incident electrons, where T_e is the kinetic energy of the electron.

There is no absolute K demarcation defining the shape of the energy loss distribution. For the needs of this experiment it is sufficient to consider that for $K > 0.2$ the energy loss

follows a Gaussian distribution and for $K < 0.2$ it follows the Landau distribution [138] (in reality, for $0.01 < K < 1.0$ the energy loss follows the Symon distribution [139, 140], but application of his theory to a specific case is difficult without considerable manipulation and extrapolation of his unpublished results).

The variance, σ_i^2 , of the Gaussian distribution is given in terms of the path length t of the particle in the material as [136]:

$$\sigma_i^2 = 4\pi e^4 n z^2 t. \quad (50)$$

The Landau distribution is asymmetric with a long high-energy loss tail and a broad peak. If ΔE is the observed energy loss, Landau has described the distribution as:

$$\Phi(\lambda) = \int_{-i\infty}^{+i\infty} \exp[\lambda u + u \ln u] du \quad (51)$$

where the parameter λ is given in terms of the parameter ξ and the most probable energy loss as $\lambda = (\Delta E - \Delta E_{prob})/\xi$. Simulation of the Landau distribution is possible using the formalism of T. Tabata and R. Ito [141].

Multiple Scattering Effects

Another effect that has to be taken into account in a simulation of electron-nucleus scattering is the multiple scattering of the incident and scattered electrons and of the recoil nuclei in the Coulomb field of the nuclei of the target materials. It contributes to the value of the integral P_{MC} and to a larger extent to the shape of the observed distributions of the scattered electrons and of the recoil nuclei at the detectors. A reliable comparison between observed and simulated detector distributions would not be possible without incorporation of multiple scattering in the Monte Carlo model.

The resultant distribution of the net space angle θ_{ms} between the incoming and outgoing directions of the particle, after passing a material of thickness t , is a Gaussian-type distribution with a long non-Gaussian tail below the 5% level. The mean square value of θ_{ms} is given by [142]:

$$\langle \theta^2 \rangle_{ms}^{\frac{1}{2}} = \left[\frac{0.157 Z(Z+1) z^2 t}{A(pv)^2} \ln \left[1.13 \times 10^4 Z^{\frac{4}{3}} z^2 t A^{-1} \beta^{-2} \right] \right]^{\frac{1}{2}} \quad (52)$$

where p is the momentum of the incident particle and A is the mass number of the material. The multiple scattering angular distribution is in practice approximated by a Gaussian function. There is no unique parametrization for the standard deviation, σ_{ms} , of such a Gaussian distribution. The best approximate formula, working very well, especially for small- Z materials, is given by Lynch and Dahl as [143]:

$$\sigma_{ms} = \frac{19.2z}{p\beta} \sqrt{\frac{X}{X_0}} \left[1 + 0.088 \log_{10}\left(\frac{z^2 X}{\beta X_0}\right) \right], \quad (53)$$

where X and X_0 are the thickness and radiation length of the material, respectively.

Transportation of Particles through the Spectrometers

The Monte Carlo model, after simulating the production of elastic events in the target, raytraces the scattered electrons and the recoil nuclei all the way to the detectors, through the electron and recoil spectrometers, respectively. This requires knowledge of the optical properties of the two magnetic spectrometers as determined from detailed magnetic measurements of their elements, and of the apertures of the elements as determined from surveys. The scattered electrons and the recoil nuclei are transported through the spectrometers in our model by means of exact raytrace or forward TRANSPORT matrix elements [62]. Exact raytrace (good to all orders in the TRANSPORT coordinates) is applied for the motion of the particles in the quadrupoles of the High Resolution Spectrometers. The raytrace uses the Lorentz force equation:

$$\frac{d\vec{p}}{dt} = q(\vec{v} \times \vec{B}), \quad (54)$$

where q is the charge of the particle and \vec{B} is the magnetic field. The 3-dimensional magnetic field \vec{B} is provided by the measured field maps $B_x(x, y, z)$, $B_y(x, y, z)$, $B_z(x, y, z)$ of the HRS quadrupoles. The propagation of the particles through the quadrupoles is done in small steps. At the end of each step a check is made to see whether the particles are lost on the physical apertures of the quadrupoles. For the transportation of the particles through the two HRS dipoles this exact method cannot be applied due to the lack of a complete field map of the dipoles. Instead a TRANSPORT model for each dipole was created based on a combination of limited magnetic measurements and TOSCA simulations. The HRS dipole

has been divided in 10 pieces, and 10 sets of 3rd-order forward matrix elements have been provided by the TRANSPORT code [144].

The forward matrix elements of a magnetic element are the coefficients of a Taylor expansion about the central trajectory of the coordinates x, θ, y, ϕ of the particle at the exit of the element in terms of its coordinates $x_o, \theta_o, y_o, \phi_o, \delta_o$ at the entrance of the element:

$$x = \sum_{\kappa, \lambda, \mu, \nu, \xi} (x | x_o^\kappa y_o^\lambda \theta_o^\mu \phi_o^\nu \delta_o^\xi) x_o^\kappa y_o^\lambda \theta_o^\mu \phi_o^\nu \delta_o^\xi \quad (55)$$

$$\theta = \sum_{\kappa, \lambda, \mu, \nu, \xi} (\theta | x_o^\kappa y_o^\lambda \theta_o^\mu \phi_o^\nu \delta_o^\xi) x_o^\kappa y_o^\lambda \theta_o^\mu \phi_o^\nu \delta_o^\xi \quad (56)$$

$$y = \sum_{\kappa, \lambda, \mu, \nu, \xi} (y | x_o^\kappa y_o^\lambda \theta_o^\mu \phi_o^\nu \delta_o^\xi) x_o^\kappa y_o^\lambda \theta_o^\mu \phi_o^\nu \delta_o^\xi \quad (57)$$

$$\phi = \sum_{\kappa, \lambda, \mu, \nu, \xi} (\phi | x_o^\kappa y_o^\lambda \theta_o^\mu \phi_o^\nu \delta_o^\xi) x_o^\kappa y_o^\lambda \theta_o^\mu \phi_o^\nu \delta_o^\xi \quad (58)$$

where the order n of the expansion is : $n = \kappa + \lambda + \mu + \nu + \xi$ ($=3$ in this case). The coordinates x and y represent, respectively, the horizontal and vertical positions of the particle, and $\theta = dx/dz$ and $\phi = dy/dz$ are the associated angles. The quantity $\delta_o = (p - p_o)/p_o$ is the fractional deviation of the momentum of the particle from the central design momentum, p_o , of the system.

Each one of the 10 sets corresponds to a magnetic element starting at the entrance of the dipole and ending at a location $mL/10$ inside the dipole, where $m = 1, 2, \dots, 10$, and L is the effective length of the dipole. Each set is used to transport the particle from the beginning of the dipole to the $mL/10$ longitudinal position inside the dipole, where an aperture check is made to see whether the particle is lost on the trapezoidal aperture of the dipole. When the particle makes it through the aperture for the 10th step, it is traced through the third HRS quadrupole. All losses of particles on the apertures are recorded and a complete picture is obtained for the solid angle defining apertures of both spectrometers.

6.3 The Effective Double-Arm Solid Angle

The Monte Carlo simulation creates pairs of scattered electrons and recoil nuclei along the beam direction in the target. The incident beam distribution is assumed to be of a Gaussian form with given standard deviation. Each scattering event originates from a beam electron that has undergone energy straggling through the target and has been multiple-scattered

before it interacts elastically with a nucleus. The location of the scattering vertex in the target is uniformly distributed over the target length. Elastic electron events are created with polar and azimuthal angles θ and ϕ in the intervals (θ_1, θ_2) and (ϕ_1, ϕ_2) around the electron spectrometer axis (with $\Delta\theta = \theta_1 - \theta_2$ and $\Delta\phi = \phi_1 - \phi_2$ larger than the angular acceptances of the electron spectrometer). The recoil nucleus momentum and polar and azimuthal angles are determined by the elastic scattering condition. All the kinematical coordinates of the scattered electrons and recoil nuclei are corrected, before they enter the respective spectrometer models, for energy straggling and multiple scattering on the way out through the target.

All probability distributions involved in the simulation like the ones for internal and external bremsstrahlung, ionization energy loss, multiple scattering and for elastic scattering at the scattering vertex, are produced by standard Monte Carlo techniques. Random deviates from a particular distribution are generated either using the direct transformation method, where possible, or the acceptance-rejection method by von Neumann. Both methods use real numbers uniformly distributed in the interval $[0,1]$ as provided by a (pseudo)random number generator.

In the Monte Carlo language, the above procedure makes the integral P_{MC} equivalent to an integral of the form

$$P_{MC} = \int \int w(E_1, \Theta) r(\Delta E', \Delta P_r) d\theta d\phi, \quad (59)$$

where the function $r(\Delta E', \Delta P_r)$ includes the portion of the electron radiative corrections that depend on the momentum acceptances of the two spectrometers, and effects from ionization energy losses and multiple scattering for both scattering partners. For N trial events randomly and uniformly distributed over the target length l and over the angular ranges $\Delta\theta$ and $\Delta\phi$, the integral P_{MC} is given, in the limit $N \rightarrow \infty$, by:

$$\int_{\theta_1}^{\theta_2} \int_{\phi_1}^{\phi_2} f(\theta, \phi) d\theta d\phi = \Delta\theta \Delta\phi \frac{1}{N} \sum_{i=1}^N f(\theta_i, \phi_i), \quad (60)$$

where:

$$f(\theta, \phi) = w(E_1, \Theta) r(\Delta E', \Delta P_r). \quad (61)$$

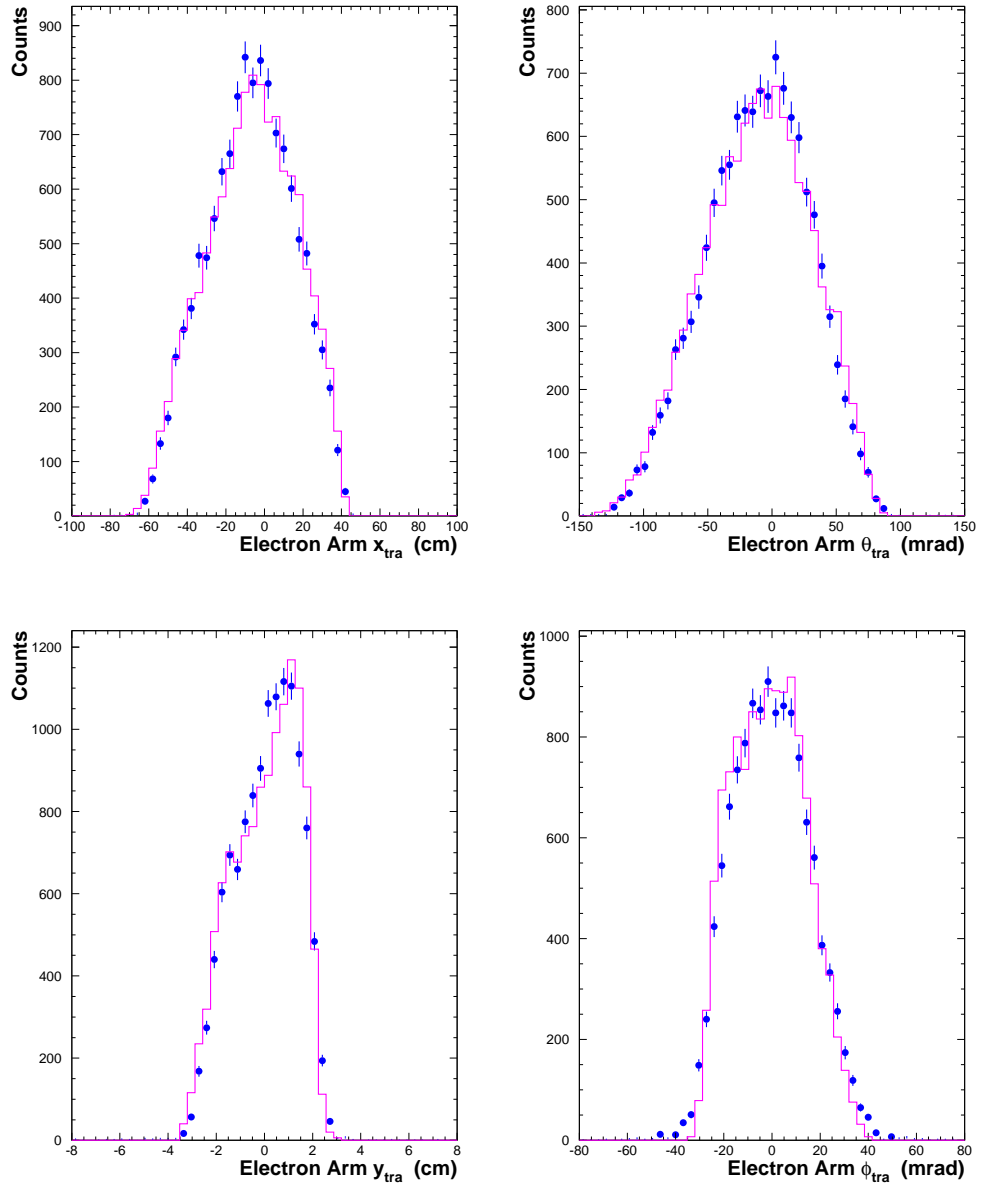


Figure 33: The JLab HRS drift chamber position and angular distributions of electrons elastically scattered off protons for one of the kinematics of experiment E91-26 (solid circles) [60]. The distributions are for coincidence events and are plotted versus the vertical (top) and horizontal (bottom) TRANSPORT position and angle coordinates. The curves represent the predictions of a Monte Carlo simulation (see text).

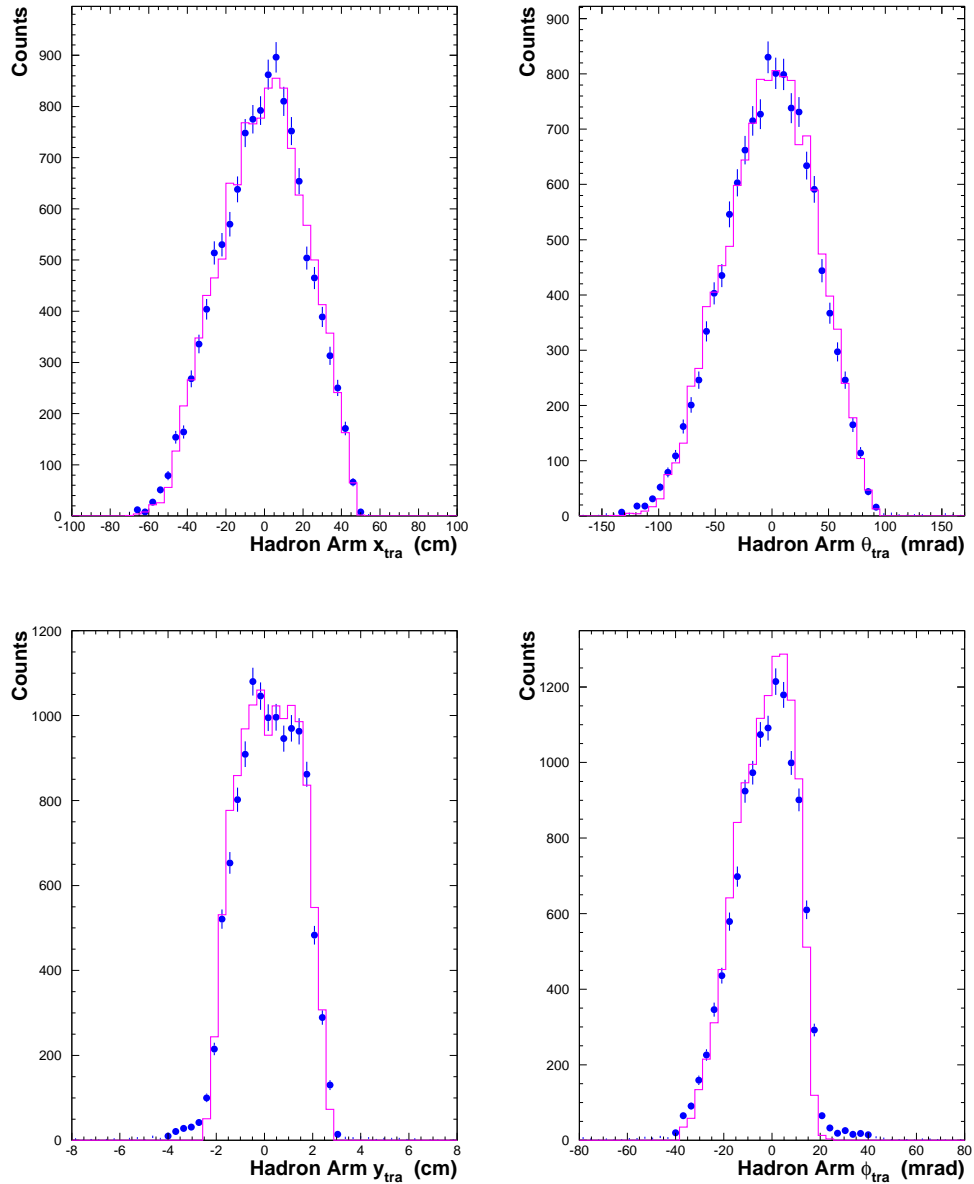


Figure 34: The JLab HRS drift chamber position and angular distributions of recoil protons for one of the elastic electron-proton kinematics of experiment E91-26 (solid circles) [60]. The distributions are for coincidence events and are plotted versus the vertical (top) and horizontal (bottom) TRANSPORT position and angle coordinates. The curves represent the predictions of a Monte Carlo simulation (see text).

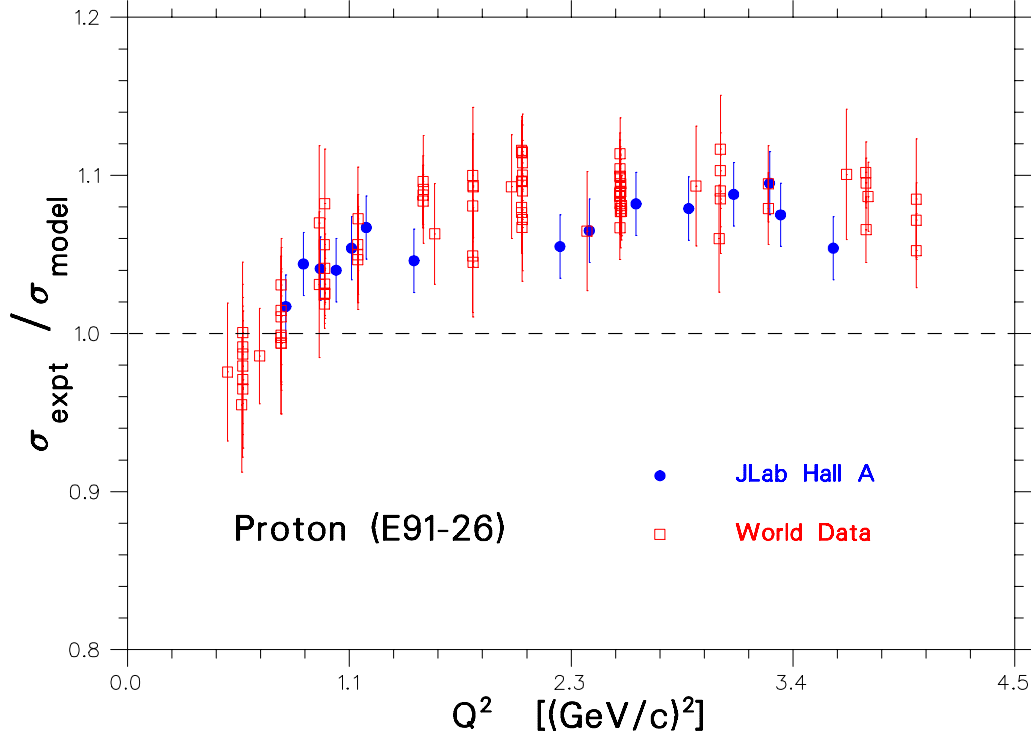


Figure 35: The elastic electron-proton cross section from JLab experiment E91-26 (measurement of the deuteron elastic structure functions) as extracted from coincidence measurements and simulation of the effective double-arm solid angle [60] compared to all previous world data for similar kinematics [94]. The experimental cross section has been divided by a model cross section assuming proton form factor scaling and using the dipole formula (see text). The JLab data include only point-to-point random errors.

Since the energy losses due to radiation and ionization and the multiple scattering effects are applied for every event, the function $f(\theta, \phi)$ takes the value:

$$f(\theta, \phi) = \begin{cases} w(E_1, \Theta) & \text{for a "good event"} \\ 0 & \text{otherwise} \end{cases} \quad (62)$$

where “good event” (or double-arm event) is considered the case when both the scattered electron and the recoil nucleus pass through the modeled spectrometers into the detectors without being lost on any limiting aperture. Small corrections for effects not accounted for by the above procedure, like radiation by the target nucleus, can be calculated in an

approximative way by using analytic formulae. It is obvious that the same procedure can be used to calculate an integral:

$$P'_{MC} = \int \int w(E_1, \Theta) r'(\Delta E') d\theta d\phi \quad (63)$$

for single-arm elastic scattering with detection of scattered electrons only, or a corresponding integral for detection of only recoil nuclei.

This method of evaluation of the integral P_{MC} was employed in the data analysis of the measurement of the electric form factor $A(Q^2)$ of the deuteron in JLab Hall A experiment E91-26. Figures 33 and 34 show a comparison [60] of the measured distributions of the coordinates of the scattered electrons and recoil deuterons at the drift chamber locations of the two HRS detectors, for one of the E91-26 kinematics, with the distributions simulated with our Monte Carlo code. It is evident that the simulated distributions are in very good agreement with the experimental distributions giving us confidence that our Monte Carlo model describes accurately all physical processes involved in the experiment and that the product P_{MC} takes into account correctly the convolution of radiative and ionization energy loss effects with the acceptances of the two spectrometers. The integral P_{MC} was used for the determination of the coincidence elastic electron-proton and electron-deuteron cross sections. Figure 35 shows the elastic electron-proton cross section from double-arm coincidence measurements at different values of Q^2 from E91-26 [60] compared to the world data at similar kinematics [94]. To obtain a linearized scale, the experimental cross section has been divided by a cross section model assuming i) that the proton magnetic form factor follows the dipole formula $G_M^p(Q^2) = (1 + Q^2/0.71)^{-2}$ and ii) that the electric form factor is $G_E^p = G_M^p/\mu_p$ (form factor scaling), where μ_p is the proton magnetic moment. The excellent agreement of the E91-26 cross section data with the world cross section data is another indication that our Monte Carlo model calculates reliably the integral P_{MC} .

7 Bibliography

References

- [1] J. Carlson and R. Schiavilla, *Rev. Mod. Phys.* **70**, 743 (1998).
- [2] M. Garçon and J. W. Van Orden, *Advances in Nucl. Phys.* **26**, 293 (2001).
- [3] R. Gilman and F. Gross, *J. Phys.* **G28**, R37 (2002).
- [4] I. Sick, *Prog. Part. Nucl. Phys.* **47**, 245 (2001).
- [5] C. E. Carlson, J. R. Hiller and R. J. Holt, *Annu. Rev. Nucl. Part. Sci.* **47**, 395 (1997).
- [6] L. C. Alexa *et al.*, *Phys. Rev. Lett.* **82**, 1374 (1999); and references therein.
- [7] P. E. Bosted *et al.*, *Phys. Rev.* **C42**, 38 (1990); and references therein.
- [8] T. W. Donnelly and A. S. Raskin, *Annals Phys.* **169**, 247 (1986).
- [9] J. Arvieux and J. M. Cameron, *Advances in Nucl. Phys.* **18**, 107 (1987).
- [10] D. M. Nikolenko *et al.*, *Phys. Rev. Lett.* **90**, 072501 (2003); M. Bouwhuis *et al.*, *Phys. Rev. Lett.* **82**, 3755 (1999); and references therein.
- [11] D. Abbott *et al.*, *Phys. Rev. Lett.* **84**, 5053 (2000); and references therein.
- [12] E. L. Lomon, *Annals Phys.* **125**, 309 (1980); and references therein.
- [13] T. W. Donnelly and I. Sick, *Rev. Mod. Phys.* **56**, 461 (1984).
- [14] R. Dymarz and F. C. Khanna, *Nucl. Phys.* **A516**, 549 (1990).
- [15] A. Amghar, N. Aissat and B. Desplanques, *Eur. Phys. J.* **A1**, 85 (1998).
- [16] B. D. Keister and W. N. Polyzou, *Advances in Nucl. Phys.* **20**, 225 (1991).
- [17] J. Carbonell, V. A. Karmanov and J. F. Mathiot, *Phys. Rep.* **300**, 215 (1998).
- [18] F. Gross, in *Modern Topics in Electron Scattering*, ed. B. Frois and I. Sick (World Scientific, Singapore, 1991).

- [19] E. Salpeter and H. Bethe, Phys. Rev. **84**, 1232 (1951).
- [20] J. W. Van Orden, N. Devine and F. Gross, Phys. Rev. Lett. **75**, 4369 (1995); J. Adam, J. W. Van Orden and F. Gross, Nucl. Phys. A640, 391 (1998); F. Gross, Fisika **B13**, 443 (2004).
- [21] E. Hummel and J. A. Tjon, Phys. Rev. **C42**, 423 (1990).
- [22] D. R. Phillips, S. J. Wallace and N. K. Devine, Phys. Rev. **C58**, 2261 (1998); Phys. Rev. **C72**, 014006 (2005).
- [23] T.-S. Cheng and L. S. Kisslinger, Phys. Rev. **C35**, 1432 (1987).
- [24] W. P. Sitarski *et al.*, Phys. Rev. **C36**, 2479 (1987); P. G. Blunden *et al.*, Phys. Rev. **C40**, 1541 (1989).
- [25] H. Dijk and B. L. G. Bakker, Nucl. Phys. **A494**, 438 (1989).
- [26] S. J. Brodsky and G. R. Farrar, Phys. Rev. Lett. **31**, 1153 (1973); Phys. Rev. **D11**, 1309 (1975).
- [27] V. A. Matveev, R. M. Muradyan and A. N. Tavkhelidze, Lett. Nuovo Cimento **7**, 719 (1973).
- [28] S. J. Brodsky, C.-R. Ji and G. P. Lepage, Phys. Rev. Lett. **51**, 83 (1983).
- [29] S. J. Brodsky and J. R. Hiller, Phys. Rev. **D46**, 2141 (1992).
- [30] A. Kobushkin and A. Syamtomov, Phys. Rev. **D49**, 1637 (1994).
- [31] G. G. Petratos *et al.*, Nucl. Phys. **A663**, 357c (2000); K. McCormick *et al.*, to be submitted to Phys. Rev. **C** (draft available).
- [32] D. Abbott *et al.*, Phys. Rev. Lett. **82**, 1379 (1999).
- [33] A. T. Katramatou, SLAC Report SLAC-NPAS-TN-86-08 (1986).
- [34] G. G. Petratos, SLAC Report NPAS-TN-86-07 (1986).

- [35] A. T. Katramatou *et al.*, Nucl. Instrum. Meth. **A267**, 448 (1988).
- [36] R. Schiavilla and D. O. Riska, Phys. Rev. **C43**, 437 (1991); R. B. Wiringa, V. G. J. Stoks and R. Schiavilla, Phys. Rev. **C51**, 38 (1995).
- [37] F. Gross, Phys. Rev. **186**, 1448 (1969); Phys. Rev. **D10**, 223 (1974); Phys. Rev. **C26**, 2203 (1982); and references therein.
- [38] R. Blankenbecler and R. Sugar, Phys. Rev. **142**, 1051 (1966); A. A. Logunov and A. N. Tavkhelidze, Nuovo Cimento **29**, 380 (1963).
- [39] H. Ito and F. Gross, Phys. Rev. Lett. **71**, 2555 (1993).
- [40] T. W. Allen, W. H. Klink and W. N. Polyzou, Phys. Rev. **C62**, 054002 (2000).
- [41] F. M. Lev, E. Pace and G. Salmè, Phys. Rev. **C62**, 064004 (2000).
- [42] R. Schiavilla and V. R. Pandharipande, Phys. Rev. **C65**, 064009 (2002).
- [43] R. G. Arnold *et al.*, Phys. Rev. Lett. **35**, 776 (1975).
- [44] S. J. Brodsky and B. T. Chertok, Phys. Rev. **D14**, 3003 (1976); B. T. Chertok, Phys. Rev. Lett. **41**, 1155 (1978).
- [45] N. Isgur and C. H. Llewellyn Smith, Phys. Rev. Lett. **52**, 1080 (1984); Phys. Lett. **B217**, 535 (1989).
- [46] G. R. Farrar, K. Huleihel and H. Zhang, Phys. Rev. Lett. **74**, 650 (1995).
- [47] E. C. Schulte *et al.*, Phys. Rev. Lett. **87**, 102302 (2001); and references therein.
- [48] L. E. Marcucci, D. O. Riska and R. Schiavilla, Phys. Rev. **C58**, 3069 (1998); L. E. Marcucci *et al.*, Phys. Rev. **C72**, 014001 (2005).
- [49] A. Imanishi *et al.*, Phys. Rev. Lett. **54**, 2497 (1985); Nuovo Cimento **A100**, 735 (1988).
- [50] D. G. Meekins *et al.*, Phys. Rev. **C60**, 052201 (1999).
- [51] P. L. Chung *et al.*, Phys. Rev. **C37**, 2000 (1988).

- [52] J. Carbonnel and V. A. Karmanov, Eur. Phys. J. **A6**, 9 (1999).
- [53] H. Arenhövel, F. Ritz and T. Wilbois, Phys. Rev. **C61**, 034002 (2000).
- [54] R. Cramer *et al.*, Z. Phys. **C29**, 513 (1985).
- [55] S. Platchkov *et al.*, Nucl. Phys. **A510**, 740 (1990).
- [56] *Nuclei, Nucleons, Quarks – Nuclear Science in the 1990’s*, Long Range Plan by the DOE/NSF Nuclear Science Advisory Committee, December 1989.
- [57] *Opportunities for Nuclear Science – A Long Range Plan for the Next Decade*, by the DOE/NSF Nuclear Science Advisory Committee, April 2002.
- [58] G. G. Petratos, *High- Q^2 Few-Body Form Factors*, presented at the 12 GeV JLab PAC18 meeting, July 2000; *The Science Driving the 12 GeV Upgrade*, L. S. Cardman *et al.*, JLab Report, 2001.
- [59] G. G. Petratos *et al.*, *JLab Proposal PR-04-018* (2004).
- [60] R. Suleiman, Ph.D. Thesis, Kent State University (2000).
- [61] P. Brinza, *A two-in-one magnet suitable for scattering experiments at 4 degrees*, JLab Hall A Internal Report (March 2005, revised December 2007).
- [62] K. L. Brown, SLAC Report 75 (1982).
- [63] F. Iachello, A. Jackson and A. Lande, Phys. Lett. **B43**, 191 (1973).
- [64] G. Höhler *et al.*, Nucl. Phys. **B114**, 505 (1976).
- [65] M. Gari and W. Krümpelmann, Z. Phys. **A322**, 689 (1985); Phys. Lett. **B173**, 10 (1986).
- [66] R. Bijker and F. Iachello, Phys. Rev. **C69**, 068201 (2004).
- [67] H. W. Hammer and U. G. Meissner, Eur. Phys. J. **A20**, 469 (2004).
- [68] E. L. Lomon, Phys. Rev. **C64**, 035204 (2001); Phys. Rev. **C66**, 045501 (2002).

- [69] M. .A. Belushkin, H. W. Hammer and U. G. Meissner, Phys. Rev. **C75**, 035202 (2007).
- [70] G. P. Lepage and S. J. Brodsky, Phys. Rev. **D22**, 2157 (1980).
- [71] A. F. Sill *et al.*, Phys. Rev. **D48**, 29 (1993).
- [72] V. L. Chernyak and I. R. Zhitnitsky, Nucl. Phys. **B246**, 52 (1984).
- [73] V. A. Nesterenko and A. V. Radyushkin, Phys. Lett. **B128**, 439 (1983); Sov. J. Nucl. Phys. **39**, 811 (1984).
- [74] G. A. Miller, Phys. Rev. **C65**, 065205 (2002).
- [75] M. K. Jones *et al.*, Phys. Rev. Lett. **84**, 1398 (2000).
- [76] O. Gayou *et al.*, Phys. Rev. Lett. **88**, 092301 (2002).
- [77] F. Iachello and Q. Wan, Phys. Rev. **C69**, 055204 (2004).
- [78] A. V. Belitsky, X. Ji and F. Yuan, Phys. Rev. Lett. **91**, 092003 (2003).
- [79] A. W. Thomas and W. Weise, *The Structure of the Nucleon*, Wiley-VCH, Berlin, 2001.
- [80] P. L. Chung and F. Coester, Phys. Rev. **D44**, 229 (1991).
- [81] F. Schlumpf, Mod. Phys. Lett. A **A8**, 2135 (1993); J. Phys. G **20**, 237 (1994).
- [82] G. A. Miller, Phys. Rev. **C66**, 032001R (2002).
- [83] M. Giannini, E. Santopito and A. Vassallo, Prog. Part. Nucl. Phys. **50**, 263 (2003); and references therein.
- [84] G. Z. Holzwarth, Z. Phys **A356**, 339 (1999); arXiv:hep-ph/0511194v2 (2005).
- [85] B. Q. Ma, D. Qing and I. Schmidt, Phys. Rev. **C65**, 035205 (2002).
- [86] F. Gross and P. Agbakpe, Phys. Rev. **C73**, 015203 (2006).
- [87] H. Gao, Inter. J. Mod. Phys. **E12**, 1 (2003).
- [88] C. E. Hyde-Wright and K. de Jager, Annu. Rev. Nucl. Part. Sci. **54**,217 (2004).

- [89] J. Arrington, C. D. Roberts and J. M. Zanotti, *J. Phys* **G14**, 523 (2007).
- [90] C. F. Perdrisat, V. Punjabi and M. Vanderhaeghen, *Prog. Part. Nucl. Phys.* **59**, 694 (2007).
- [91] M. E. Christy et al., *Phys. Rev.* **C70**, 015206 (2004).
- [92] I. A. Qattan *et al.*, *Phys. Rev. Lett.* **94**, 142301 (2005).
- [93] E. J. Brash *et al.*, *Phys. Rev.* **C65**, 051001 (2002).
- [94] L. Andivahis *et al.*, *Phys. Rev.* **D50**, 5491 (1994); and references therein.
- [95] P. G. Blunden, W. Melnitchouk and J. A. Tjon, *Phys. Rev.* **C72**, 034612 (2005).
- [96] P. A. M. Guichon and M. Vanderhaeghen, *Phys. Rev. Lett.* **91**, 142303 (2003).
- [97] J. Arrington, W. Melnitchouk and J. A. Tjon, *Phys. Rev.* **C76**, 035205 (2007).
- [98] P. E. Bosted, *Phys. Rev.* **C51**, 409 (1995).
- [99] R. C. Walker *et al.*, *Phys. Rev.* **D49**, 5671 (1994).
- [100] R. Bradford *et al.*, arXiv:hep-ex/0602017 (2006).
- [101] J. M. Cavedon *et al.*, *Phys. Rev. Lett.* **49**, 987 (1982).
- [102] A. Amroun *et al.*, *Phys. Rev. Lett.* **69**, 253 (1992); *Nucl. Phys.* **A579**, 596 (1994).
- [103] I. Nakagawa *et al.*, *Phys. Rev. Lett.* **86**, 5446 (2001).
- [104] E. Hadjimichael, in *International Review of Nuclear Physics*, Vol. 3, World Scientific, Singapore (1985). *Phys. Rev.* **C58**, 3069 (1998).
- [105] R. Schiavilla, V. R. Pandharipande and D. O. Riska, *Phys. Rev.* **C40**, 2294 (1989);
R. Schiavilla and D. O. Riska, *Phys. Lett.* **B244**, 373 (1990).
- [106] R. Schiavilla, V. R. Pandharipande and D. O. Riska, *Phys. Rev.* **C41**, 309 (1990).
- [107] R. B. Wiringa, *Phys. Rev.* **C43**, 1585 (1991).

- [108] M. J. Musolf, R. Schiavilla and T. W. Donnelly, Phys. Rev. **C50**, 2173 (1994).
- [109] J. Carlson, Phys. Rev. **C38**, 1879 (1988).
- [110] D. O. Riska, Phys. Rep. **181**, 207 (1989).
- [111] V. V. Burov and V. K. Lukyanov and A. I. Titov, Z. Phys. **A318**, 67 (1984);
V. V. Burov and V. K. Lukyanov, Nucl. Phys. **A463**, 263c (1987).
- [112] M. A. Maize and Y. E. Kim, Phys. Rev. **C31**, 1923 (1985).
- [113] L. S. Kisslinger, W.-H. Ma and P. Hoodbhoy, Nucl. Phys. **A459**, 645 (1986); W.-H. Ma
and L. S. Kisslinger, Nucl. Phys. **A531**, 493 (1991).
- [114] H. Dijk and M. Beyer, Phys. Lett. **B237**, 323 (1990).
- [115] T. Katayama, Y. Akaishi and H. Tanaka, Prog. Theor. Phys. **67**, 236 (1982).
- [116] H. Collard *et al.*, Phys. Rev. **138**, B57 (1965).
- [117] J. S. McCarthy, I. Sick and R. R. Whitney, Phys. Rev. **C15**, 1396 (1977).
- [118] M. Bernheim *et al.*, Lett. Nuovo Cimento **5**, 431 (1972).
- [119] P. C. Dunn *et al.*, Phys. Rev. **C27**, 71 (1983).
- [120] D. H. Beck *et al.*, Phys. Rev. **C30**, 1403 (1984).
- [121] C. R. Ottermann *et al.*, Nucl. Phys. **A436**, 688 (1985).
- [122] R. G. Arnold *et al.*, Phys. Rev. Lett. **40**, 1429 (1978).
- [123] E. Hadjimichael, B. Goulard and R. Bornais, Phys. Rev. **C27**, 831 (1983); E. Had-
jimichael, Phys. Lett. **B172**, 156 (1986).
- [124] W. Strueve, Ch. Hajduk, P. U. Sauer and W. Theis, Nucl. Phys. **A465**, 651 (1987).
- [125] H. Henning, P. U. Sauer and W. Theis, Nucl. Phys. **A537**, 367 (1992).
- [126] G. Rupp and J. A. Tjon, Phys. Rev. **C45**, 2133 (1992).

- [127] A. Stadler, F. Gross and M. Frank, Phys. Rev. **C56**, 2396 (1997).
- [128] F. Gross, A. Stadler and M. T. Peña, Phys. Rev. **C69**, 034007 (2004).
- [129] J. A. Adam and J. W. Van Orden, Phys. Rev. **C71**, 034003 (2005).
- [130] R. B. Wiringa, V. G. J. Stoks and R. Schiavilla, Phys. Rev. **C51**, 38 (1995).
- [131] B. S. Pudliner *et al.*, Phys. Rev. Lett. **74**, 4396 (1995).
- [132] R. F. Frosch *et al.*, Phys. Rev. **160**, 874 (1967).
- [133] L. W. Mo and Y. S. Tsai, Rev. Mod. Phys. **41**, 205 (1969).
- [134] Y. S. Tsai, SLAC-PUB-848 (1971).
- [135] R. M. Sternheimer and R. F. Peirls, Phys. Rev. **B3**, 3681 (1971).
- [136] A. Crispin and G. N. Fowler, Rev. Mod. Phys. **42**, 290 (1970).
- [137] U. Fano, Ann. Rev. Nucl. Sci. **13**, 1 (1960).
- [138] L. D. Landau, J. Phys. U.S.S.R. **8**, 201 (1944).
- [139] K. R. Symon, Ph.D. Thesis, Harvard University (1948).
- [140] B. Rossi, *High Energy Particles*, Prentice-Hall, Inc., New Jersey (1961).
- [141] T. Tabata and R. Ito, Nucl. Instr. and Meth. **158**, 521 (1979).
- [142] R. M. Sternheimer, in *Methods of Experimental Physics*, Vol. 5, edited by L. C. Yuan and C. S. Wu, Academic Press, New York (1961).
- [143] G. R. Lynch and O. I. Dahl, LBL Report 28165 (1990).
- [144] D. C. Carey, K. L. Brown and F. Rothacker, SLAC Report 462 (1995).